Platinum Single-site Catalysts for the Hydrogen Evolution Reaction



Peng Tang

Department of Materials

St. Catherine's College

University of Oxford

A thesis submitted for the degree of

Doctor of Philosophy

Abstract

To meet the International Energy Agency (IEA) net zero emissions scenario, terawatt-scale green hydrogen production is needed from renewable electricity using proton exchange membrane (PEM) water electrolysis. However, PEM water electrolysis now requires using rare and expensive noble metal electrocatalysts, undermining its economic viability for large-scale deployment. Single-site catalysts (SSCs), have active structures of isolated metal sites supported on substrates and thus could alleviate this problem by maximising the noble metal utilisation without comprising activity. The synthesis, activity, and stability of SSCs are determined by the interaction between isolated metal sites and supporting substrates. Platinum single-site catalysts (Pt SSCs) supported on carbon substrates have been proposed as efficient and stable electrocatalysts for the hydrogen evolution reaction (HER). However, due to the complexity of the atomic structure and the lack of in-situ characterisation techniques, the Pt SSCs' synthesis strategy, formation mechanism, atomic structure, and electrocatalytic activity for the HER are still highly debated. Therefore, the main focus of this project is to systematically explore the synthesis, characterisation, and catalytic activity of Pt SSCs that are stabilised differently on carbon substrates for the HER.

To achieve this target, three different types of Pt SSCs were initially synthesised, as defined by the interaction between the single site and the substrate. Firstly, Pt single-site complexes physically adsorbed onto graphene were synthesised by interacting with aniline molecules. After clarifying its atomic structure, I present a mechanistic study of this platinum SSC for the HER using operando, synchrotron-X-ray absorption spectroscopy. The results indicate that the physically adsorbed Pt SSC are decomposed, and platinum agglomerates as nanoparticles at operating potentials. Then, to provide a stronger interaction between Pt sites and the substrate, Pt single sites were chemically bonded to the surface of a polyaniline substrate. With the advantage of complementary characterisation techniques, the atomic

structure of this chemisorbed Pt SSC was clarified, and its active structure for the HER was recorded. Finally, a Pt SSC trapped at defects of N-doped graphene, the most stable single-site structure, was prepared by pyrolysis. In-situ characterisation techniques were employed to thoroughly clarify its formation mechanism and atomic structure. Using this well-defined model Pt SSC, it is found that the stable Pt SSC displays a lower intrinsic activity for the HER than metallic Pt nanoparticles.

This thesis provides a comprehensive study of how the interaction between Pt single sites and substrates affects the catalytic activity of Pt SSCs for the HER through advanced synthesis strategies and detailed characterisation techniques. My study clarifies the desired structure of Pt SSC for the HER and will aid the design and synthesis of improved SSC for the HER and other electrochemical reactions.

Some of the results presented in this work are shown in the following publications:

1. Peng Tang, Hyeon Jeong Lee, Kevin Hurlbutt, Po-Yuan Huang, Sudarshan Narayanan, Chenbo Wang, Diego Gianolio, Rosa Arrigo, Jun Chen, Jamie H. Warner, and Mauro Pasta. Elucidating the formation and structural evolution of platinum single-site catalysts for the hydrogen evolution reaction. ACS catalysis, 12(5), 3173-3180 (2022).
2. Peng Tang, Po-Yuan Huang, Jack E. N. Swallow, Chenbo Wang, Diego Gianolio, Hua Guo, Jamie Warner, Robert S. Weatherup, and Mauro Pasta. Structure-property relationship of defect-trapped Pt single-site electrocatalysts for the hydrogen evolution reaction. Submitted.

Dedication

To my family, who have always supported me in all these years.

Declaration

I declare that the work presented in this thesis, unless otherwise stated, is the result of my original work and is written by myself.

Acknowledgments

I want to express my gratitude to everybody who helped and supported me during this DPhil period.

I am very grateful to Prof. Mauro Pasta for granting me the opportunity to join the group and conduct my research in an excellent place. I also appreciate his encouraging supervision and kindest help during the past four-year DPhil study at Oxford. In addition, many thanks to my previous supervisor, Jamie H. Warner, for taking me to Oxford four years ago.

Thanks to my group colleague, Po-Yuan Huang, for helping with this research. I also thank the postdoctoral researchers in the group, Kevin Hurlbutt and Chenbo Wang, for their help and support with my journal papers.

I want to thank my collaborators: Dr. Jack E. N. Swallow for his help with the in-situ temperature-dependent XPS experiment; Dr. Diego Gianolio for his contribution to the measurement of the XAS data; and Dr. Hua Guo for their help with acquiring the NMR data.

I am grateful to the financial support from the Jiangsu Industrial Technology Research Institute (JITRI) and the Henry Royce Institute (through UK Engineering and Physical Science Research Council grant EP/R010145/1) for capital equipment. Many thanks to the David Cockayne Center for Electron Microscopy for using their microscopes. And I would like to acknowledge Diamond Light Source for time on B18 Beamline.

Lastly, I will give my deepest gratitude to my parents, Yiquan Tang and Linzhi Luo, without whom, I would never be able to complete this degree. I would also like to thank my cousins, Hong Tang and Qin Tang, for their support and kindest advice. Also, many thanks to my friends, in particular, my four-year friends: Wendy Wang, Sissi Ma, Qingniao Li, Xiaonan Luo, and Donghao Liu, who make my life at Oxford much happier.

Table of Contents

Abstract ii

Dedication iv

Declaration v

Acknowledgments vi

Introduction 1

1.1 The global demand for hydrogen 1

1.2 Hydrogen production technology 3

1.3 Water electrolysers 7

1.4 Proton exchange membrane water electrolyser 10

1.4.1 Structure and mechanism 10

1.4.2 Break down the cost 13

1.5 Catalysts in the PEM water electrolyser 15

1.5.1 State-of-the-art catalysts 15

1.5.2 Next steps for catalysts 16

1.6 Single-site catalysts 18

1.6.1 Definition of SSCs 18

1.6.2 Synthesis methods for SSCs 20

1.6.3 Pt SSCs for the HER 33

1.7 Aim and structure of this project 36

1.8 References 39

Methodology 46

2.1 Materials preparation 46

2.1.1 Thin-layer graphene substrate grown by the CVD method 46

2.1.2 Wet impregnation of Pt sites 47

2.1.3 One-pot pyrolysis 49

2.1.4 Casting catalysts on the glassy carbon electrode 50

2.2 Materials characterisation techniques 51

2.2.1 Scanning transmission electron microscopy 52

2.2.2 X-ray photoelectron spectroscopy 54
2.2.3 X-ray absorption spectroscopy 55
2.2.4 Raman spectroscopy 58
2.2.5 Infrared spectroscopy 59
2.2.6 X-ray diffraction pattern 61
2.2.7 Nuclear magnetic resonance 62
2.3 Electrochemical characterisation techniques 63
2.3.1 Linear sweep voltammetry 63
2.3.2 Cyclic voltammetry 65
2.3.3 Chronoamperometry 66
2.3.4 Potentiostatic electrochemical impedance spectroscopy 67
2.4 References 68
Physically adsorbed Pt SSC 72
3.1 Introduction 72
3.2 Results and discussion 74
3.2.1 Synthesis and physiochemical characterisation 74
3.2.2 Ex-situ XPS and XAS 75
3.2.3 Operando XAS measurements 77
3.2.4 Structure-electrochemistry correlation 80
3.3 Conclusion 83
3.4 References 84
Chemically bonded Pt SSC 90
4.1 Introduction 90
4.2 Results and discussion 91
4.2.1 Synthesis of Pt single sites on polyaniline 91
4.2.2 Chemical structure of Pt-PANI 92
4.2.3 HER activity of the chemisorbed Pt single sites on PANI substrate 94
4.2.4 Structure of Pt-PANI after activity tests 96
4.3 Conclusion 98

4.4 References 98
Defect-trapped Pt SSC 101
5.1 Introduction 101
5.2 Results and discussion 103
5.2.1 Synthesis of trapped Pt SSC on N-doped graphene by pyrolysis 103
5.2.2 Formation mechanism of trapped Pt SSC 105
5.2.3 HER activity of trapped Pt SSC 108
5.2.4 The structure of trapped Pt SSC at working potential 112
5.3 Conclusion 114
5.4 References 114
Conclusions and future work 119
Key findings 119
Future work 121
Appendices 122
A. In-situ temperature-dependent XPS data 122
B. The customised three-electrode system 123
C. STEM images of commercial 20 wt% Pt/C 123
D. In-situ heating STEM images of Pt-PANI showing another edge area during heat treatment 124
E. Ex-situ XPS data of Pt-PANI with different Pt loading after pyrolysis 124
F. STEM images of trapped Co and Ir SSC on N-doped graphitic carbon 125

Chapter 1

Introduction

1.1 The global demand for hydrogen

The 2021 International Energy Agency (IEA) Global Energy Review has stated that global energy-related CO_2 emissions have consistently increased to 31.5 Gt/year, which caused CO_2 to reach its highest-ever average annual atmospheric concentration in 2020 at 412.5 parts per million.[1] The world has reached a consensus that measures should be taken immediately to cut the CO_2 emission from fossil fuels. Looking back to the Paris Agreement, countries made pledges to limit global warming below 1.5 °C. More recently, the 26th UN Climate Change Conference (COP26) in Glasgow led to further agreements to accelerate international decarbonisation. The overall target is to reduce global CO_2 emissions by 45% by 2030 relative to the 2010 level and achieve net zero around mid-century, as well as deep reductions in other greenhouse gases.[2]

Hydrogen, a versatile energy carrier without carbon emission on combustion, is considered to be the ultimate way to displace fossil fuels with a green energy resource. Due to the large bond dissociation enthalpy of H-H (436 kJ/mol),[3] its gravimetric energy density (33.33 kWh/kg) is 2.78 times higher than that of gasoline.[4] Therefore, hydrogen and hydrogen-based fuels are one of the critical pillars of decarbonisation for the global energy system. The significance of hydrogen on the path to net zero emission is reflected in its increasing share in cumulative emission reductions. According to the calculations in the IEA hydrogen report, 60 Gt of CO_2 emissions could be prevented from 2021-2050 under the net zero emissions scenario.

There has been a strong growth in demand for hydrogen in recent years. Specifically, according to the IEA, the global hydrogen demand was around 90 million tonnes (Mt) in 2020 (Fig. 1.1); it almost all fills into oil refining (37.18 Mt) and industrial uses (51.30 Mt). The industrial uses include chemical production (Fig. 1.1) (~46 Mt for ammonia and methanol production) and steelmaking (5 Mt). But only 0.3 Mt of 2020 demand was met with low-carbon hydrogen, mainly from a handful of large-scale carbon capture and utilisation (CCU), carbon capture and storage (CCS) plants, and small electrolysis units in the chemical subsector.[5] However, the global demand for green hydrogen produced by electrolysis will dramatically increase to nearly 80 Mt (close to 1 TW hydrogen production), and the total low-carbon hydrogen demand will rise to more than 150 Mt by 2030 under the net zero emissions scenario. But only 0.3 Mt of 2020 demand was met with low-carbon hydrogen, mainly from a handful of large-scale carbon capture and utilisation (CCU), carbon capture and storage (CCS) plants, and small electrolysis units in the chemical subsector.[5] However, the global demand for green hydrogen produced by electrolysis will dramatically increase to near 80 Mt (close to 1 TW hydrogen production), and the total low-carbon hydrogen demand will rise to more than 150 Mt by 2030 under the net zero emissions scenario.

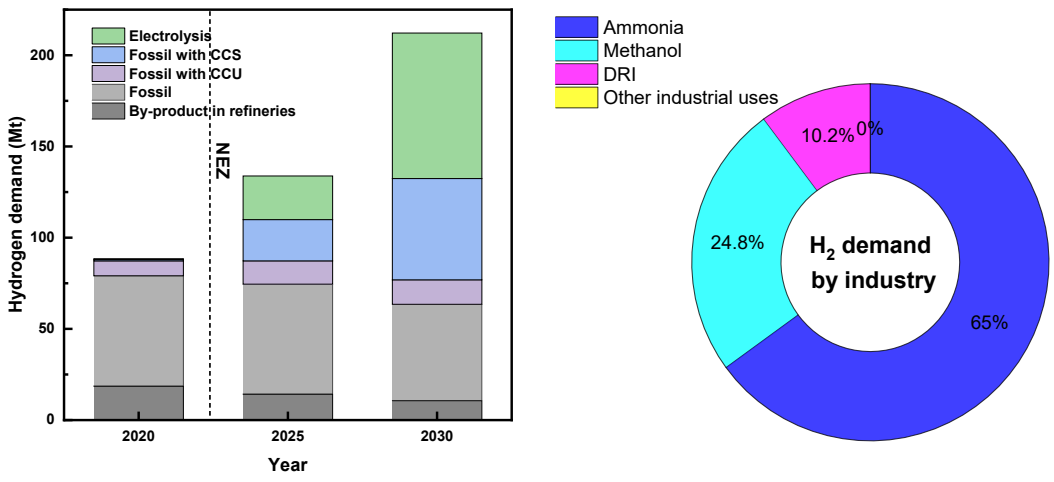


Figure 1.1: Global hydrogen demand by production technology and global hydrogen demand by industry in 2020. Adapted from [5] with permission.

The projected demand growth for low-carbon hydrogen by 2030 mainly comes from steel refining, industry, and new applications, including transport, industrial applications, synthetic

fuel production, and electricity storage. The demand for those new applications could reach more than 120 Mt annually by 2030, which could help significantly to reduce CO_2 emissions.

The projected demand growth for low-carbon hydrogen by 2030 mainly comes from steel refining, industry, and new applications, including transport, industrial applications, synthetic fuel production, and electricity storage. The demand for those new applications could reach more than 120 Mt annually by 2030, which could help significantly to reduce CO_2 emissions. Particularly, according to the UK hydrogen strategy, to achieve the net zero emission by 2050 and being a global leader on hydrogen by 2030, the UK government has set some ambitious goals about hydrogen: (1) 1 GW (equal to ~0.08 Mt of H_2) low-carbon hydrogen production capacity by 2025 and 5 GW hydrogen production with potential for rapid expansion by 2030; (2) low-carbon hydrogen will being make up 20-35 percent of UK final energy consumption (28.5 to 53.0 GW) in 2050.[6]

In summary, in the net zero emissions scenario, the global demand for hydrogen continually increases. However, current progress falls well short of these targets. More focus must be paid to reduce hydrogen production costs if those goals are to be met.

1.2 Hydrogen production technology

To meet the global demand for hydrogen at the terawatt (TW equal to Mt of hydrogen) level, hydrogen production techniques with low-carbon emissions are the key. Hydrogen can be produced via several routes, including methane, oil, coal, electrolysis, and bioenergy. Most of the production today (~95%) is based on fossil fuels (natural gas, oil, and coal) with heavy carbon emissions.[7] Although the production of hydrogen by fossil fuels can be decarbonised to a low level with the use of CCS, it requires significant infrastructure, which is exposed to the price fluctuations characteristic of fossil fuels and faces social acceptance issues. Green hydrogen is generated by electrolysis with energy from renewable sources leading to zero-carbon hydrogen production, which is an attractive alternative.

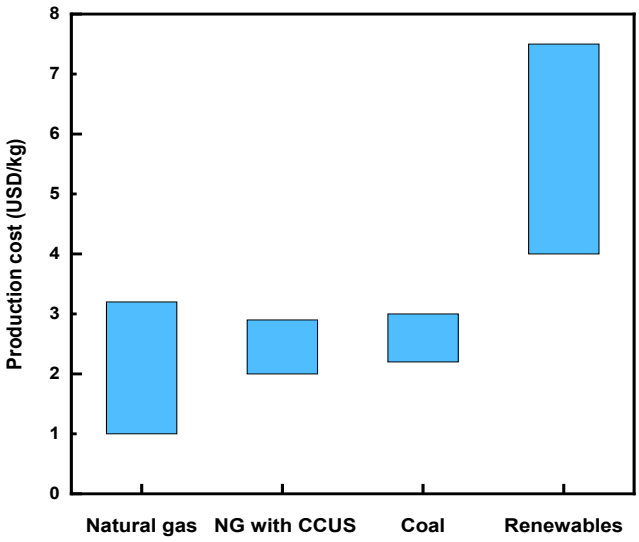


Figure 1.2: Hydrogen production costs by production source in 2018. Adapted from [7] with permission.

As shown in Fig. 1.2, the dedicated production of green hydrogen by electrolysis is still relatively low because the cost of electrolytic hydrogen (USD 3-8/kg H_2) is 2-3 times more than blue hydrogen from fossil fuels (USD 1-3/kg H_2) in most places around the world today. However, some regions have favourable conditions leading to a competitive cost of green hydrogen produced by electrolysis already. For example, if the wind or solar energy could have a capacity factor of almost 50%, with an electricity cost of USD 25-30/MWh, this low electricity price would be sufficient to achieve a green hydrogen production cost of about USD 2.5/kg, close to the blue hydrogen cost range.[7] Unfortunately, because of the small installation of water electrolysers and not low enough electricity prices, there is still a price gap between green hydrogen from electrolysis and blue hydrogen from fossil fuels. Narrowing the gap requires further reductions in low-carbon electricity costs and larger-scale electrolysers with longer operation hours and higher efficiency.

The price of hydrogen production by an electrolyser is mainly determined by the investment cost, electricity price, and operating hours. The relationship between them is described in Fig. 1.3a. When the electrolyser operating hours are low, the investment cost dominates because only a limited amount of hydrogen is produced. However, with higher operating hours and lower electricity prices, the production price of hydrogen can drop quickly. Therefore, green

hydrogen could become cost-competitive with fossil fuel-based hydrogen when there is access to low-cost renewable electricity, low investment cost, and long operating hours (3,000-4,000 hours) a year.

Thanks to the large-scale installation of renewable power generation capacity, the cost of renewable electricity has fallen sharply over recent decades, driven by steadily improving technology, economies of scale, competitive supply chains, and improving the developer experience.[8] Specifically, the cost of electricity from solar and wind has dropped by 85% from 0.381 USD/kWh to 0.057 USD/kWh and by ~56% from 0.089 USD/kWh to 0.039 USD/kWh (Fig. 1.3b) from 2010 to 2022, respectively. For example, Brasil and Saudi Arabia have achieved cost levels for renewable electricity of 2-3 US cents per kWh based on utility-scale solar PV (photovoltaic) and onshore wind. Based on analysis from the International Renewable Energy Agency (IRENA), the costs of new utility-scale solar PV and onshore wind electricity generation are lower than the operating costs of existing coal-fired capacity.

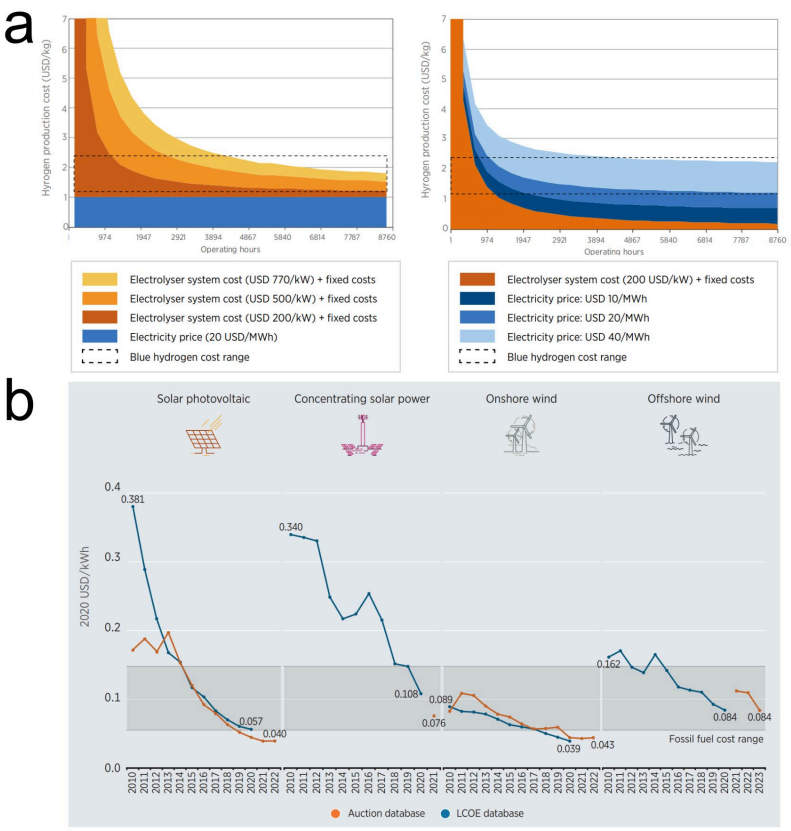


Figure 1.3: Cost of Hydrogen production by electrolysis as a function of investment cost, electricity price, and operating hours (top); the global weighted-average LCOE and auction

prices for solar PV, onshore wind, offshore wind, and CSP, 2010-2023 (bottom). The figure reproduced from the [8] with permission.

In addition, electrolyser technology has matured enough to be developed at scale, so manufacturing and deployment costs can be significantly reduced. According to a report from the IEA, record levels of new hydrogen electrolyser capacity were deployed over three consecutive years in 2018, 2019, and 2020. Despite the impact of the pandemic, 70 MW of water electrolysis was deployed in 2020, bringing the total capacity to almost 300 MW worldwide (Fig. 1.4). In 2022, the installed capacity has already broken the 1 GW barrier with continuing momentum to develop further production capacity. More importantly, as more countries have announced they plan to use hydrogen as an energy resource in recent years, electrolysis capacity deployment is expected to accelerate significantly through 2030. More than 25 GW of new electrolysis projects has already been announced between 2020 and 2025.

Thanks to the dramatic cost reduction of solar and wind-based renewable electricity and the increasing load factor of electrolysers, there is now an opportunity to provide low-cost green hydrogen globally by water electrolysis using energy from renewable sources. To achieve the ambitious targets set for green hydrogen in its role in reducing CO_2 emissions, further efforts should be focused on decreasing the cost and increasing the operating hours of water electrolysers.

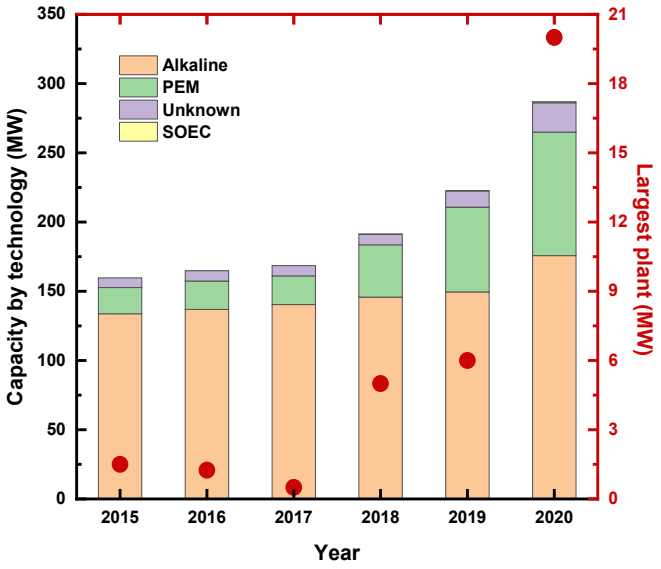


Figure 1.4: Global installed electrolysis capacity by technology from 2015 to 2020. Adapted from [5] with permission.

1.3 Water electrolysers

Green hydrogen can be produced in water electrolysers based on renewable electricity. Water electrolysers are electrochemical devices that split water molecules into oxygen and hydrogen by passing an electrical current. Three leading low-temperature electrolyser technologies are being used or explored today: the alkaline, proton exchange membrane (PEM), and anion exchange membrane (AEM) water electrolysers. Fig. 1.5 a, b, c shows schematics of these three different water electrolysers. The other one is high-temperature steam electrolysis, solid oxide electrolysis cell (SOEC). SOEC is regarded as more efficient because of its advantages for the water splitting both thermodynamically and kinetically, (Fig. 1.5.d) but it's application is highly inhibited by materials problem, cell stability because of the high-temperature condition. Therefore, SOEC is at very early stage and will not be discussed in detail in this thesis.

The most mature technology is the alkaline water electrolyser, broadly deployed globally with more than 200 MW of capacity by 2021. In an alkaline water electrolyser, the water-splitting reaction occurs between two electrodes in a solution composed of water and an alkaline electrolyte. The OH^- ion is transferred from the cathode to the anode through an electrochemical process. The two half-reactions generate oxygen and hydrogen and can be

catalysed by nickel and nickel-based alloys. Alkaline water electrolysers are typically operating with a current density lower than 0.5 A cm^{-2} and a voltage conversion efficiency of around 70% in 2020.[9] The hydrogen it produces is low-pressure with a purity of about 99.5%. Due to its simple architecture, low-cost electrode materials, long lifetime, and ability to ramp up and down production more quickly than the other two primary options, alkaline electrolysers make up the largest share of all installed electrolysis capacity.[10] However, it suffers from a slow system response (seconds to minutes) to fluctuating power supply due to its slower ion conduction in liquid, which makes it more difficult and costly to connect them with renewable electricity sources efficiently.

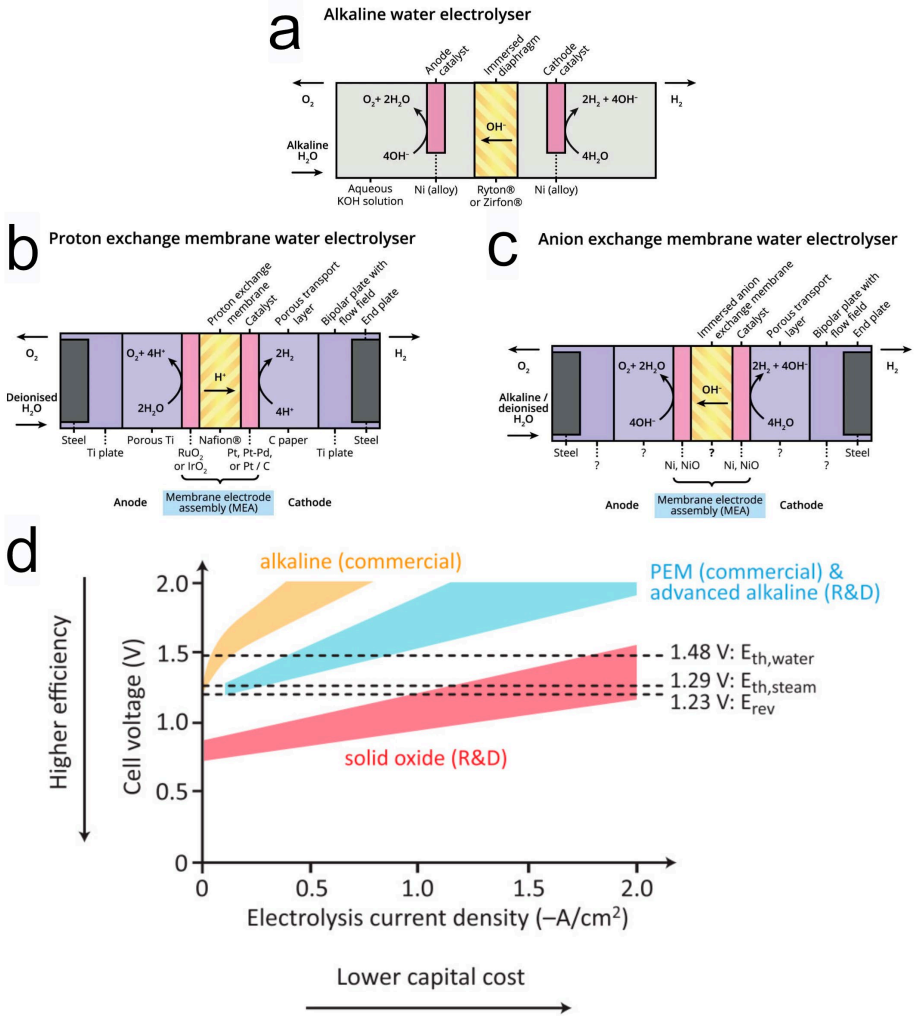


Figure 1.5: Low-temperature water electrolyser architectures and designs. **a**, Alkaline water electrolyser. **b**, Proton exchange membrane (PEM) water electrolyser. **c**, Anion exchange membrane water electrolyser. The components, commonly used materials, and commercial products of each electrolyser design are listed at the top and bottom of the schematics,

respectively. The figure reproduced from [9] with permission. **d**, Comparison between alkaline, PEM, and solid oxide electrolysers in terms of voltage vs. current density. $E_{th,water}$ and $E_{th,steam}$ are the thermoneutral voltages for water and steam electrolysis, respectively. E_{rev} is the reversible potential for water electrolysis at standard state. Adapted from [11] with permission.

In comparison, PEM water electrolysers can operate at higher current densities, above 1.6 A cm^{-2}, with higher voltages, and are able to produce high-purity H_2 gas (>99.9999%). Unlike an alkaline water electrolyser, a PEM water electrolyser operates using an acid electrolyte, and protons are transferred from anode to cathode through a Nafion membrane. More importantly, thanks to the fast proton transfer in the electrochemical device, the PEM water electrolyser has a faster system response time (on the order of seconds) that can ramp up and down with energy input. This means that it is compatible with renewable energy electricity based on wind and solar power. However, as the schematic shows, the catalysts used on both sides of the device are precious metals like platinum and iridium. Due to the high price and scarcity of these materials, the cost of PEM water electrolysers is relatively high. In addition, the current collector (titanium) and Nafion membrane are also expensive. These factors have slowed down the deployment of PEM water electrolysers.

The third option is an anion exchange membrane (AEM) water electrolyser, which combines the advantages of previous electrolysers. AEM water electrolysers can conduct ions in solid-state conditions with a fast response time at around 1 A cm^{-2} current density. Only cheap transition metals, such as nickel, are needed to trigger these reactions, so the cost of those electrode materials is not as high as the PEM water electrolyser. However, there is not an established high-quality conductive ion exchange membrane that can be used to separate the two reactions yet.

To sum up, at the moment, alkaline water electrolysers are the most mature electrolysis devices for producing low-carbon hydrogen with electricity due to its competitive cost and reasonable lifetime (~80,000 h). However, for large-scale zero-carbon green hydrogen based on renewable electricity, PEM water electrolysers is a better choice to scale up efficiently because they are compatible with a renewable power supply and can operate with high current

densities, power densities, and differential operating pressures. The biggest constraint of the PEM water electrolyser is the relatively high cost of the catalysts, membranes, and titanium plates.

1.4 Proton exchange membrane water electrolyser

1.4.1 Structure and mechanism

The characteristic structure of a standard PEM water electrolyser is illustrated in Fig. 1.6. It has three main components. These include (i) the membrane electrode assembly (MEA), which is located between the electrodes and separates the two electrochemical reactions. The MEA is generally comprised of a proton exchange membrane, such as Nafion, with both sides coated with electrocatalysts to accelerate the electrochemical reactions. (ii) Porous gas diffusion layers (GDL) outside of the MEA are made of titanium at the anode and carbon paper at the cathode. The GDL can transfer the current from the bipolar plates to the MEA and facilitate the release of generated gas products during electrolytic reactions. Finally, (iii) the bipolar plates and end plates assembly can be found on the outer edges of the cell. The bipolar plates (current collector) are usually made of titanium due to the high current densities used. The end plate assembly is steel, separating each cell in the electrolyser stack, and is also connected with a flow path for water circulation.[12] As described above, the structure of a PEM water electrolyser is more complex and compact than an alkaline water electrolyser. It would use less space once scaled up, which makes it more suitable for large-scale hydrogen production.

The mechanism of water splitting in PEM water electrolysers is highlighted here. In a low-temperature PEM water electrolyser, two electrodes with catalysts are placed in complete contact with the acid electrolyte. Then a sufficient voltage is passed across the electrodes to split the water molecules into hydrogen (H_2) and oxygen (O_2). The water splitting reaction can be divided into two half-reactions: the hydrogen evolution reaction (HER) at the cathode and

the oxygen evolution reaction (OER) at the anode. The reaction process can be described using the three equations shown in Fig. 1.7.

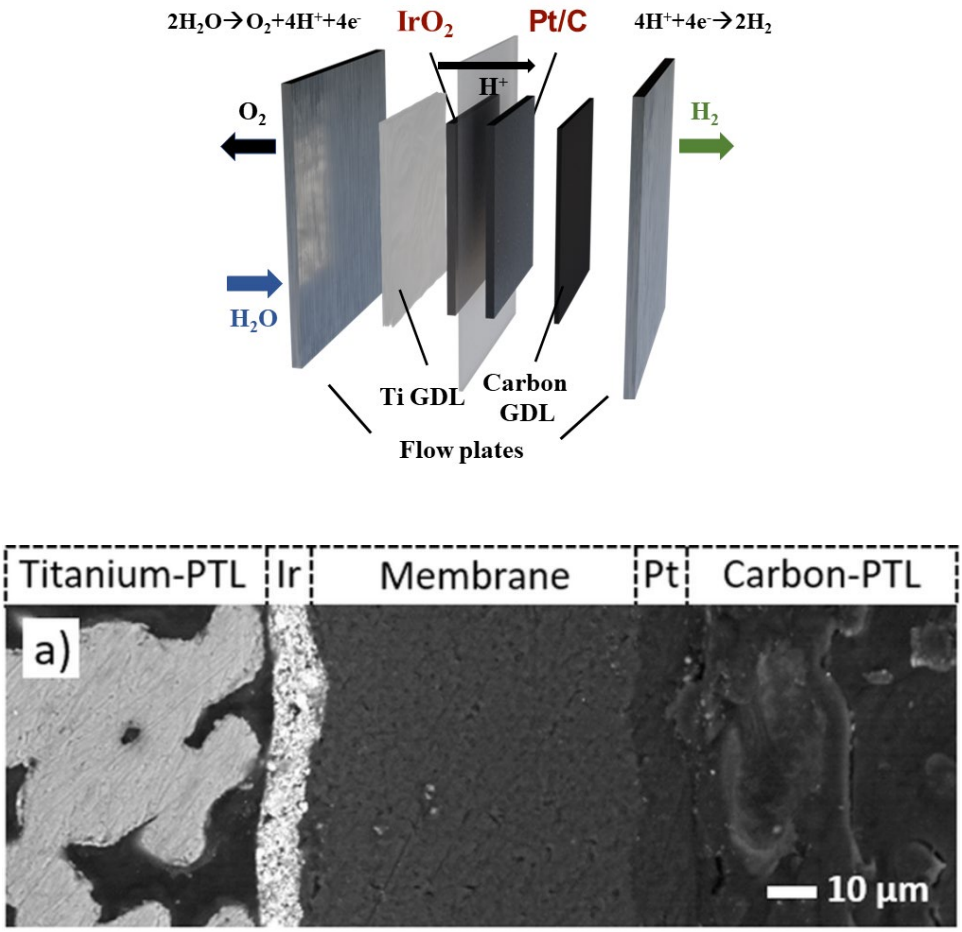


Figure 1.6: Typical structure of a proton exchange membrane water electrolyser with materials design (top); and cross-sectional SEM image of an typical MEA (bottom). From left to right: anode PTL (titanium sinter), anode electrode composed of IrO_2/TiO_2 catalyst and ionomer, 50 µm thick Nafion 212 membrane, cathode electrode composed of 4.8 wt% Pt/C and ionomer, cathode PTL (carbon paper). Adapted from [13] with permission.

In a PEM water electrolyser, the protons migrate from the anode to the cathode through different solutions within an overall electrical field, while the electrons travel through an external circuit from the anode to the cathode to maintain charge neutrality. By definition, the generation of H_2 and O_2 are coupled, meaning that H_2 and O_2 are produced simultaneously at one potential. To avoid mixing the generated gases, an ion-exchange membrane is necessary to separate the cathode and anode. Due to the catalytic overpotential (the extra voltage required beyond the thermodynamic minimum to drive the reaction) and cell resistance, the

thermodynamics of water splitting is 1.23 V (reversible cell voltage) at 25 °C and 1 atm; more than 1.7 V is generally required to reach a current density of 2 A cm^{-2} in a practical PEM water electrolyser.[14] As shown in Fig. 1.7, the high potential (>1.7 V) needed for PEM water electrolyser includes 5 parts: reversible cell voltage, OER/HER overpotential loss, ohmic loss, ionic resistance loss, and H_2 mass transport loss. This high overpotential dramatically decreases the energy efficiency of hydrogen production converted from renewables. Employing precious metal catalysts can minimise these overpotentials.

Cathode: $2H^+ + 2e^- \rightarrow H_2$

Anode: $H_2O \rightarrow 2H^+ + 2e^- + 1/2O_2$

Overall: $H_2O \rightarrow H_2 + 1/2O_2$

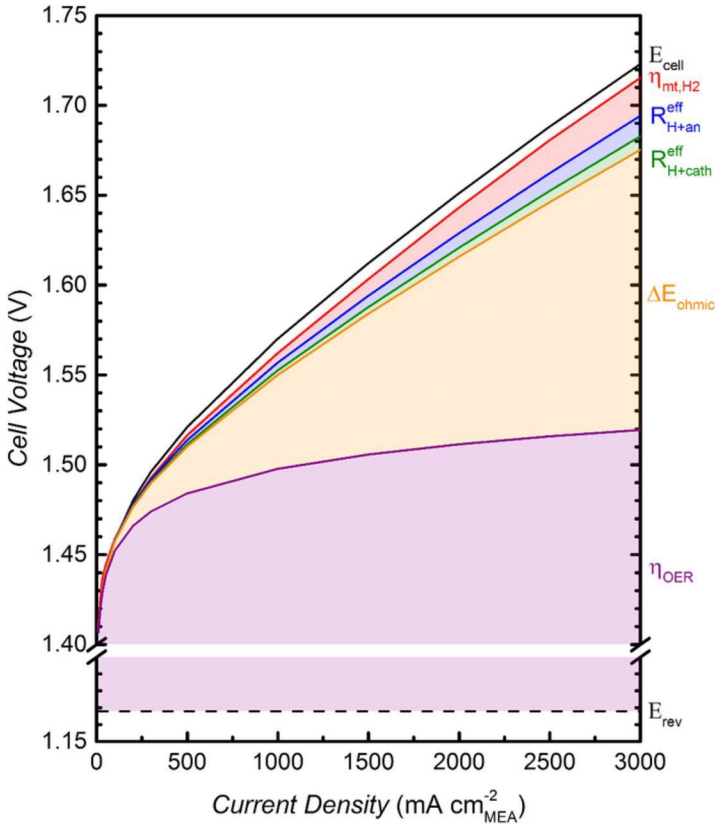


Figure 1.7: Typical chemical reactions of PEM water electrolyser and its cell voltage breakdown to different loss components: E_{cell}−overall cell voltage, $\eta_{mt,H2}$−mass transport loss, R^{eff}_{H+an}–anode–ionic resistance loss, R^{eff}_{H+cath}–cathode–ionic resistance loss, ΔE_{ohmic}−ohmic loss, η_{OER}−OER overpotential loss, Erev−reversible cell voltage. Adapted from [15] with permission.

1.4.2 Break down the cost

To understand the potential cost reductions for PEM water electrolysers, the various manufacturing costs must be considered.[16] Based on a report from the National Renewable Energy Laboratory, electricity price and electrolyser capital cost are the main factors that determine the cost of hydrogen production using PEM water electrolysis. Due to the rapid decrease in renewable electricity prices, electricity price is not a significant problem. The PEM water electrolysis system cost is a critical issue in cutting the cost of hydrogen production.

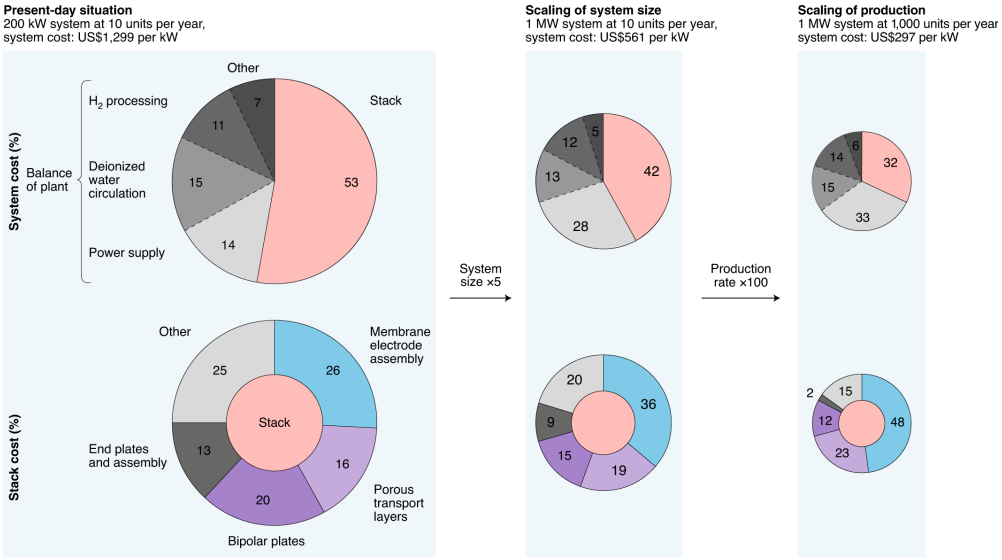


Figure 1.8: Cost breakdown for PEM electrolysers as a function of the manufacturing scale. Adapted from [9] with permission.

The capital cost of a PEM water electrolyser can be divided into two main parts: balance-of-plant (BOP) and stack (Fig. 1.8). The BOP cost consists of power supplies, deionized water circulation, hydrogen processing, and the others (a cooling system and miscellaneous parts). Stack cost is composed of the assembly, end plates, bipolar plates, frames, porous transport layer (PTL), and membrane electrode assembly (MEA or CCM). The BOP costs for a 1 MW electrolyser at 1000 units a year contribute about two-thirds of the system cost, with power electronics contributing half the BOP cost. The water circulation and hydrogen processing subsystems contribute about two-fifths of the BOP cost together. As shown in Fig. 1.9, the BOP costs can be decreased with the economics of scale from 323 $/kWh to 196 $/kWh from a production volume of 10 MW to 1,000 MW a year.

At high production volumes, raw material costs dominate stack costs. For PEM electrolyser stacks, the MEA manufacturing cost is about 36%–48% of the total cost for a 1 MW stack, with PTL contributing around 17%–25% of the stack cost, bipolar plates about 12%–21%, and end plates and assembly 3%–13%.[16] The power density, Pt loading, Pt price, and bipolar plates dominate the overall stack cost. It is necessary to cut these costs by improving power density by 20%, which would cut \$20/kWh, and reducing the Pt loading from 1.1 mg/cm^2 to 0.1 mg/cm^2, which would cut \$24/kWh (Fig. 1.9).

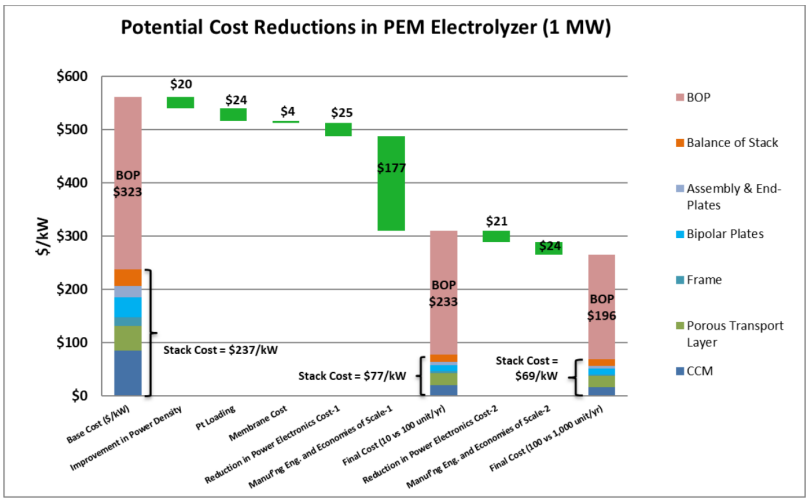


Figure 1.9: Potential cost reduction in PEM electrolysers (units of 1 MW per year). Reprinted from [16] with permission.

However, the most significant cost reduction would come from adopting more advanced manufacturing processes, such as high throughput and automated processes with high yields. For example, as an estimate, roll-to-roll manufacturing of catalyst-coated membranes and advanced coating processes for metal plates could reduce the cost for the PEM electrolyser stacks from \$237/kW (±10%) at a production volume of 10 MW (e.g., 1 MW systems at a production rate of 10 units/year) to \$69/kW (±10%) at 1,000 MW (e.g., 1 MW systems at 1,000 unit/year).

In summary, thanks to the decreasing electricity prices now, to make green hydrogen production by PEM water electrolysers cost-competitive, increasing system capacity and reducing the cost of the raw materials in electrolyser (precious metal, bipolar plates, and end plates) will be essential.

1.5 Catalysts in the PEM water electrolyser

1.5.1 State-of-the-art catalysts

Platinum (Pt) nanoparticles are the commercial electrocatalysts for HER, and only tens of mV overpotential are needed to achieve a reasonable hydrogen evolution rate (~2 A cm^{-2}). Iridium dioxide (IrO_2) is the most common commercial catalyst employed in PEMs for the OER; generally, more than 300 mV is necessary to achieve a current density of 2.0 A cm^{-2}. From a calculation conducted by Ib Chorkendorff et al., the state-of-the-art PEM electrolysers reported by 3M can stably operate at 2.0 A cm^{-2} for 5,000 hrs with 0.25 mg_{Pt} cm^{-2} at the cathode (and 0.25 mg_{Ir} cm^{-2} at the anode) in a nanostructured thin film. Even with this lowest loading of Pt, ~100 tonnes of platinum (close to 60% of the current annual production of Pt) are needed to convert 1 TW electricity into hydrogen.[17] Typically, the current commercial PEM water electrolyser uses platinum loadings of 0.5–1.0 mg cm^{-2}, which would need several times the current annual production of Pt to achieve TW-scale hydrogen production. Moreover, Pt is a crucial and efficient catalyst commercially utilised in many chemical reactions, not only for HER in PEM water electrolyser.

For catalysts on the OER side, although significant improvement has been achieved over the past decades, an overpotential of approximately 300 mV is necessary to reach a 10 mA cm^{-2} current density due to the sluggish oxygen formation steps. Recently, 3M reported nanostructured thin film catalysts with an Ir loading of only 0.25 mg cm^{-2} at the anode that can achieve a current density of 2.0 A cm^{-2} at 1.85 V in a real PEM water electrolyser. Even under these optimised conditions, it still currently requires at least ~100 tonnes of iridium for 1 TW of hydrogen production (corresponding to ~80 Mt of H_2). Unfortunately, iridium is just a by-product of other platinum group metals with an annual production rate of fewer than 10 tonnes.

To deploy TW scale green hydrogen production by PEM water electrolysers, the loading of precious metals on MEA must be decreased (by at least a factor of 10), or alternative cheap metal catalysts with reasonable activity and stability must be discovered.

1.5.2 Next steps for catalysts

First, investigations into cheaper metal catalysts have been done by Jaramillo's group at Stanford, where they conducted a detailed comparison of different metals for the HER and OER in acid and alkaline electrolytes.[18] They compare the performance (activity and stability) of those metal catalysts using a benchmarking protocol and a rotating disk electrode system. They deposit the catalysts on the disk and test the overpotential needed to reach a current density of 10 mA cm^{-2} and the overpotential required when controlling the current density at 10 mA cm^{-2} for 2-hour stability tests.

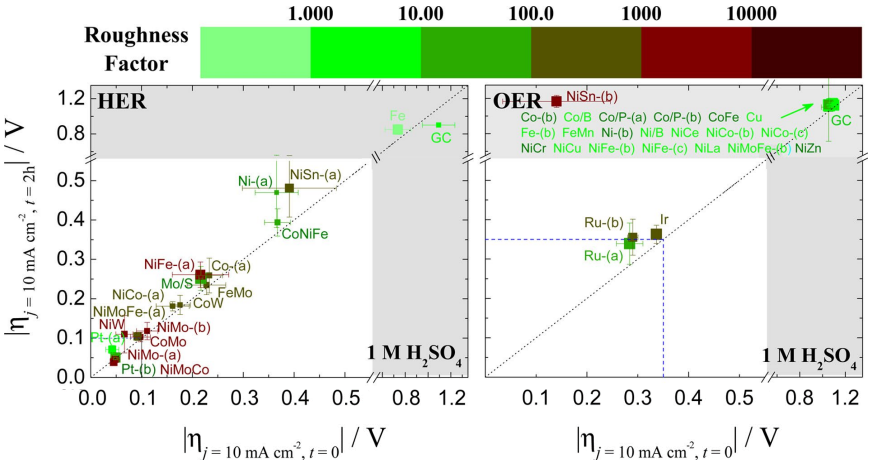


Figure 1.10: Plots of catalytic activity, stability, and electrochemically active surface area for the HER (left) and OER (right) electrocatalysts in acidic solutions. The *x*-axis is the overpotential required to achieve 10 mA cm^{-2} per geometric area at $t = 0$. The *y*-axis is the overpotential required to achieve 10 mA cm^{-2} per geometric area at $t = 2$ h. The diagonal dashed line is the expected response for a stable catalyst whose activity does not change during 2 h of constant polarization. The colour of each point represents the roughness factor of the catalyst with a bin size of 1 order of magnitude, with light green representing RF = 1 and dark red representing RF > 10^4. The size of each point is inversely proportional to the standard deviation in the electrochemical active surface area (ECSA) measurements. There is a break and change in scale in both axes at overpotentials >0.55 V, and the corresponding region of the plot is shown in grey. Adapted from [18] with permission.

Among the HER catalysts shown in Fig. 1.10, although several transition metal-based alloys could operate at 10 mA cm^{-2} with overpotentials <0.1 V in acidic solutions, Pt-based catalysts still hold the highest intrinsic activity even after more than 10 years of exploration. Moreover, those transition metal alternative catalysts for HER usually suffer from large-scale synthesis problems, and no commercial products have been achieved. For OER catalysts, no non-noble

metal-based materials have shown promising activity and stability, and Ir and Ru are still the only two materials that can reach a current density of 10 mA cm^{-2} at overpotentials of ~350 mV in acidic solutions.

In summary, for the catalysts used in PEM water electrolysers operating under acid solutions, Ir-based materials remain the only commercial catalysts for the OER due to their superior activity and stability in acid conditions. For the HER side, to operate with high activity and stability at low overpotentials, Pt-based materials are still the first choice in the current industrial manufacturing system. Although a few non-precious metal catalysts, including cobalt phosphide (CoP), have demonstrated the potential to produce hydrogen as a small electrolyser prototype, their specific activities are still much lower than Pt.[19, 20] Therefore, precious metals remain the bottleneck to scaling up PEM water electrolysers.

However, to achieve zero-carbon emissions on the necessary time scales, large-scale high-loading factors of PEM water electrolysers need to be employed soon, and precious metal catalysts are still indispensable. To support the development of TW hydrogen production via PEM water electrolysis, decreasing the loading of Pt and Ir used in water electrolysers without compromising their activity and stability is a better option in the short term. Taking the commercial Pt/C catalysts for the HER as an example, the state-of-the-art catalysts used in the PEM water electrolyser are nanoparticles with an average size of around 3 nm.[21] From an electrochemical study measured by Kucernak et al. via a floating electrode, as shown in Fig. 1.11, Pt atoms at edges and vertices are two to three orders of magnitude more active than those at the facets for hydrogen evolution.[22] Also, the precious metal atoms in the bulk of the particles are not accessible to catalyse reactions, which means the utilisation of precious atoms used in the reactions is relatively low. From a calculation by Liu et al., the best Pt catalysts for the HER are predicted to be Pt clusters with a size below ~20 atoms.[23] These fundamental scientific results demonstrate that it would be possible to decrease the loading of precious metals significantly down to 1 $\mu g_{Pt}/cm^2$ in electrolysers without losing any activity by

changing the atomic structures. Theoretically, the loading of precious metals could be two to three orders of magnitude lower than what is currently used.

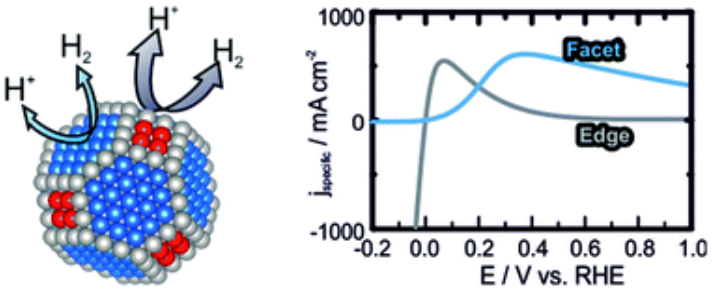


Figure 1.11: Schematic showing how protons are reduced to H_2 molecules at a Pt nanoparticle and the activity of metallic Pt atoms at the facet and edge for the HER. Reprinted from [22] with permission.

In conclusion, to cut the cost of PEM water electrolysers and meet the urgent demand for their large-scale deployment, I have focused my thesis on decreasing the loading of precious metals, such as Pt and Ir, used in electrolysers via cutting-edge nanostructure engineering science at the atomic level.

1.6 Single-site catalysts

1.6.1 Definition of SSCs

For catalysts in a PEM water electrolyser, the commercial catalysts currently used are Pt nanoparticles on active carbon substrates for the HER and IrO_2 nanoparticles on TiO_2 or SnO_2 for the OER, respectively. These Pt and IrO_2 catalysts are supported on high surface area substrates and are 2 nm to 5 nm in size. They are usually composed of hundreds of metal atoms. However, only the atoms at the edges and vertices are active for catalysis.[24] The utilisation of metal atoms can be significantly improved by exposing more active sites and constructing new structures.

Metal catalysts and nanostructures supported on the surface of substrates, including metal oxides, metal surfaces, and carbon materials, are widely used types of heterogeneous

catalysts in current industrial processes. From mechanistic studies, it has been found that the size of the metal particles is a critical factor in determining the performance of catalysts, usually referred to as the particle size effect. Because of this, low-coordinated metal sites often demonstrate more active and uniquely selective catalytic properties. The specific activity per metal atom usually increases with decreasing size of the metal particles. This is because low-coordinated metal sites show distinct electronic structures. For example, metal clusters around 1 nm in size have already demonstrated different selectivity and reactivity compared to nanoparticles, which have been used by the chemical industry for a long time.

The ultimate small structure of heterogeneous catalysts should be single-site catalysts (SSCs).[24] SSCs are single metal sites supported on substrates and separated from other metal sites by a distance larger than their metallic bonding. Reducing the size from nanoparticles to single atom sites can expose all metal atoms and maximise their utilisation, which is particularly valuable for precious metal catalysts (Fig. 1.12). Moreover, at the atomic scale, the catalytic properties of SSCs are determined by their atomic orbitals, which are quite different from their properties in clusters and nanoparticles (Fig. 1.12). Therefore, SSCs offer great potential for achieving high atom utilisation, increased activity, and high selectivity for chemical reactions.

However, single metal sites are not easily formed due to the high surface free energy of metals at the atomic level. To prevent the aggregation of metal sites, single metal sites are needed to interact with appropriate substrates. The synthesis, activity, and stability of SSCs rely heavily on the interaction between isolated metal atom sites and supporting substrates, which is the key to understanding SSCs.[25, 26] Several substrates have proven to be ideal for supporting SSCs, including metal oxides, metal surfaces, two-dimensional (2D) materials, and carbon materials. For electrochemical applications, carbon-based substrates are the most reported supporting matrix to immobilise single sites because of their high electrical conductivity and electrochemical stability.

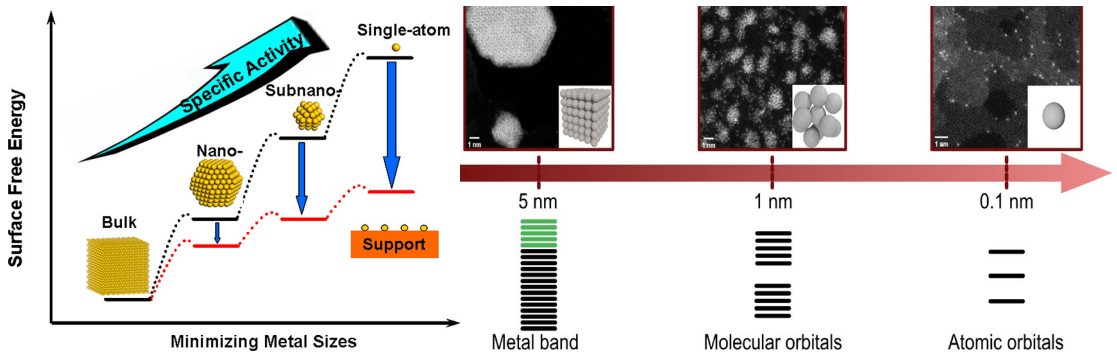


Figure 1.12: Schematic illustrations of the changes in the surface free energy, specific activity per metal atom with metal particle size, and the supporting effects on stabilizing single atoms (left). Adapted from [24] with permission. Typical physical and electronic structures of nanoparticles, clusters, and single-site catalysts on carbon support (right).

1.6.2 Synthesis methods for SSCs

Due to the energetically preferential aggregation of metal atoms, it is very challenging to synthesise well-dispersed single-site catalysts. To overcome this propensity for single metal atom sites to aggregate during synthesis, the interaction of single sites and the underlying support is critical. In terms of the different interactions between single metal sites and substrates, here we summarise all SSCs structures and initially divide them into three different types: (1) physically adsorbed SSCs, (2) SSCs chemically bond to the substrate surface by ligands, and (3) single sites trapped or embedded into substrates. This thesis summarises the recent advances in synthetic methods developed by researchers to synthesise SSCs, such as strong electrostatic adsorption, van der Waals interaction, wetness impregnation and grafting, atomic layer deposition (ALD), electrodeposition, and pyrolysis synthesis.

1.6.2.1 Physical interaction: electrostatic adsorption and van der Waals interaction

SSCs can be adsorbed onto the surface of supports by weak physical interactions, such as electrostatic adsorption and van der Waals interactions. In solutions, the surface of oxide materials is often covered with a layer of hydroxyl groups, and the charge of those oxides can be adjusted by simply controlling the pH values of aqueous solutions. The oxides are positively

charged when pH values are below their isoelectric point and negatively charged in the cases where pH values are above their isoelectric point. By adjusting pH values, a monolayer of O^-, OH, or OH_2^+ could be formed on the surface of oxides.[27] Then, those hydroxyl groups are capable of anchoring various metal ion complexes via strong electrostatic interactions, such as the metal ion complexes $[(NH_3)_4Pt]^{2+}$ or $[PtCl_6]^{2-}$ (Fig. 1.13a). It has been experimentally and theoretically found that the synthesis of SSCs by electrostatic interaction depends on having a solid electrostatic interaction between the support and appropriate metal ion complexes.[28, 29] The electrostatic adsorption method has been proven effective for preparing singly dispersed noble metal catalysts. However, the efficiency and quality of this method of preparing SSCs are greatly influenced by the heterogeneity of substrates and the instability of the aqueous solution.

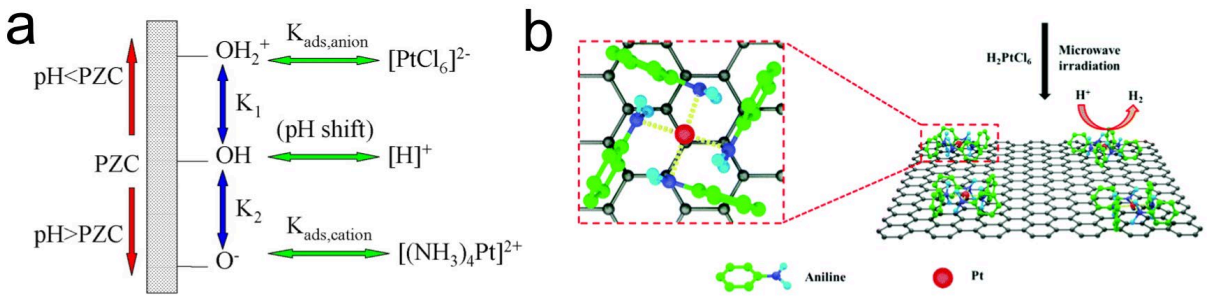


Figure 1.13: a, Mechanism of electrostatic adsorption by adjusting solution pH value. Adapted from [27] with permission. **b**, schematic of Pt single sites bonding with aniline molecules to be stacked on the surface of graphene nanosheets by pi-pi interactions. Adapted from [30] with permission.

Another physical interaction to synthesise SSCs is van der Waals interaction between single-site complex and substrates (Fig. 1.13b). Sun's group has shown that highly stable Pt single sites can be anchored on aniline-stacked graphene for the HER using this interaction. In this system, aniline molecules will first stack with graphene by $\pi - \pi$ interaction. And then, the nitrogen atoms in aniline will coordinate with the Pt single sites from H_2PtCl_6 as they are reduced by microwaves.[30] These single-site heterogeneous catalysts can be easily synthesised by adsorbing soluble single-site complexes on proper substrates such as mesoporous silicas with large surface areas.[31] Although the well-defined SSCs synthesised

by physical adsorption can combine some merits of homogeneous catalysts and heterogeneous catalysts, these single-site structures are still not stable enough in harsh reaction conditions, such as high temperatures and during electrochemical cycling.

1.6.2.2 SSCs chemically bonded to the surface: wetness impregnation, grafting

Single metal sites can be chemically bonded to the surface of the support by covalent interactions, which can immobilise isolated metal atom sites. The wetness impregnation method is one of the conventional strategies to prepare heterogeneous catalysts: a soluble metal salt impregnates the catalysts by being adsorbed on the support surface to form a covalent bond. Then the residual solvent can be simply removed by evaporation to obtain a metal-site impregnated catalytic surface. Kwak et al. showed that Pt could be anchored as isolated sites on unsaturated pentacoordinate Al^{3+} (Al^{3+}_{penta}) centres present on the (100) facets of the γ-Al_2O_3 surface by coordination after wetness impregnation of γ-Al_2O_3 with an aqueous solution of Pt salt. Unfortunately, there is a limitation on the density of pentacoordinate Al^{3+}, which can form Pt particles with increasing Pt loading. The author found that the structure of Pt changes from atomically dispersed single sites to a combination of isolated Pt sites and Pt nanoparticles when the loading of Pt increases from 1 wt% to 10 wt% (Fig. 1.14a-d).[32]

Similarly, single-site Pt catalysts which are loaded up to 8 wt% have been successfully prepared on an ATO (antimony tin oxide) support (Pt1/ATO) by a conventional incipient wetness impregnation (Fig. 1.14e-h). When $H_2PtCl_6 \cdot 6H_2O$ (precursors) are simply mixed with the ATO support and reduced at 400 °C, Pt replaces Sb in the bulk phase or at the surface of SbSn or ATO. This substitution is energetically preferred, as confirmed by density functional theory (DFT) calculations. Scanning transmission electron microscope (STEM) images and extended X-ray absorption fine structure (EXAFS) analysis results show that Pt exists as a

single atom without Pt nanoparticles. Compared with a commercial Pt/C catalyst, the Pt1/ATO offers superior activity and durability for the formic acid oxidation reaction.[33]

Another typical technique to synthesise single-site catalysts is surface organometallic chemistry (SOMC) by grafting well-defined molecular precursors on well-defined support. As shown in Fig. 1.15a, when combined with thermolytic molecular precursors (TMPs) that can lose their organic moieties quite readily upon thermal treatment, SOMC provides access to supported isolated metal sites with a defined oxidation state and nuclearity inherited from the precursor.[34] This proposed approach can provide an ideal way to generate uniform and atomically defined dispersed metal centres on well-defined supports. It could help make structure-activity relationships possible.

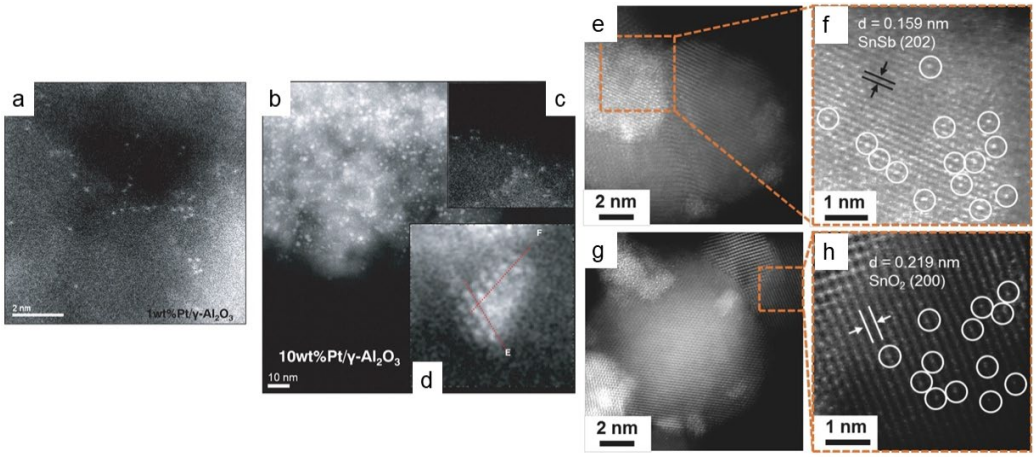


Figure 1.14: High-resolution STEM images of 1 wt % Pt/γ-Al_2O_3 (**a**) and 10 wt % Pt/γ-Al_2O_3 (**b** to **d**) samples. The image in (**a**) shows the presence of mostly atomically dispersed Pt. **c**, The presence of atomically dispersed Pt. **d**, Pt rafts that dominate the STEM image at 10 wt% Pt loadings. Adapted from [32] with permission. **e, g**, HAADF-STEM images of Pt1/ATO and (**f, h**) magnified images of (**e, g**). Adapted from [33] with permission.

Liu et al. were the first to prepare a well-defined thin layer of single-crystalline MgO(111) nanosheet substrates that contained triple-coordinated-O^{2-} anions and isolated -OH groups. This was then left in full contact with Ir(COD)(acac) (COD, cyclooctadiene; acac, acetylacetonate) in pentane for three hours (Fig. 1.15b). According to infrared spectroscopy, the disappearance of the Mg–OH (3,573 cm^{-1}) bond, together with the appearance of bridging –O–H (3,513 and 3,374 cm^{-1}) and C–H (3,080–2,840 cm^{-1}) stretches supports an anchoring process via grafting (Fig. 1.15c).[35] Furthermore, X-ray absorption spectroscopy and high-

resolution scanning transmission electron microscopy showed that 0.1 wt% and 1 wt% Ir sites were anchored on the surface of the MgO nanosheets as single sites or fully exposed clusters (Fig. 1.15e, f). These Ir species display unique catalytic properties in the coupling reaction between benzene and ethylene to form styrene.

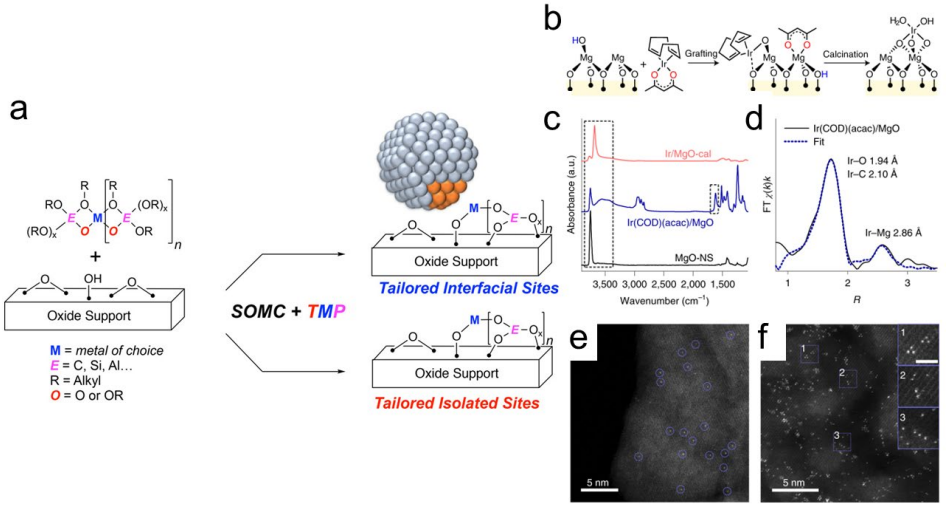


Figure 1.15: a, A general strategy to prepare single-sites or supported nanoparticles using surface organometallic chemistry (SOMC) and thermolytic molecular precursors (TMPs). Adapted from [34] with permission. **b**, Schematic procedure for grafting of Ir(COD)(acac) onto MgO nanosheets, followed by calcination to form Ir/MgO-cal. **c**, FTIR characterisation of the supported, grafted, and calcined materials. **d**, FT extended X-ray absorption fine structure spectra of grafted Ir(COD)(acac) on MgO-NS. **e**, **f**, Representative ADF-STEM images of 0.1 wt% (**e**) and 1 wt% (**f**) Ir/MgO-cal catalysts: Inset: monomer, dimer, and trimer Ir assemblies (scale bar, 1 nm). Adapted from [35] with permission.

This shows that SSCs can be synthesised and tailored by an SOMC combined with thermal treatments to form well-defined structures. Using in-situ characterisation techniques, structure-activity relationships can be determined and engineered for those SSCs, which has been demonstrated in many traditional chemical catalysis reactions. However, due to the selectivity of substrates to precursors, only limited sites can be used to graft metal precursors; it is tough to anchor a high loading of single sites on these substrates.[36]

1.6.2.3 SSCs trapped or embedded into substrates: atomic layer deposition, electrodeposition, pyrolysis synthesis

Atomic layer deposition (ALD) is a typical way to prepare uniform and conformal metal-based thin films and nanostructures. It relies on ligands or functional groups on the supports to react

with gas-phase metal precursors under a high vacuum. Functionalised carbon-based substrates are an excellent candidate to anchor metal sites through metal-N-C or metal-O-C coordination using the ALD technique. Sun's group first reported SSCs prepared by ALD to deposit Pt single sites and clusters on nitrogen-doped graphene nanosheets for catalysis of the HER (Fig. 1.16a-e).[37] An N-doped graphene nanosheet (NGNs) was synthesised. Pt structures were on the N-doped graphene using $MeCpPtMe_3$ and O_2 as precursors. High-purity N_2 (99.9995%) was used as a purging and carrier gas. The NGN powder was placed in a container inside the ALD reactor chamber. The deposition temperature was 250 °C, while the container for the $MeCpPtMe_3$ was kept at 65 °C to provide a steady-state flux of $MeCpPtMe_3$ to the reactor. Gas lines were held at 100 °C to avoid precursor condensation. For each ALD cycle, there was a 1 s pulse of the $MeCpPtMe_3$ and a 5 s pulse of O_2 , which were separated by a 20 s N_2 purge.[37] By adjusting the number of ALD cycles, different Pt catalyst structures could be synthesised, ranging from single sites and sub-nanometre clusters to NPs. Highly exposed single Pt atoms and clusters show exceptionally high activity and stability as HER catalysts compared with commercial Pt/C catalysts. According to an operando X-ray absorption spectroscopy (XAS) study, the superior performance of those Pt single sites on N-doped graphene is due to the high dispersion of Pt sites and a partial reduction of those Pt sites under reduction potentials, which is confirmed by DFT modelling analysis.[38] The same methods and processes are adaptable to synthesise Pd SSCs on oxygen-doped graphene substrates by using oxygen functional groups to anchor Pd single sites (Fig. 1.16f-i).[39]

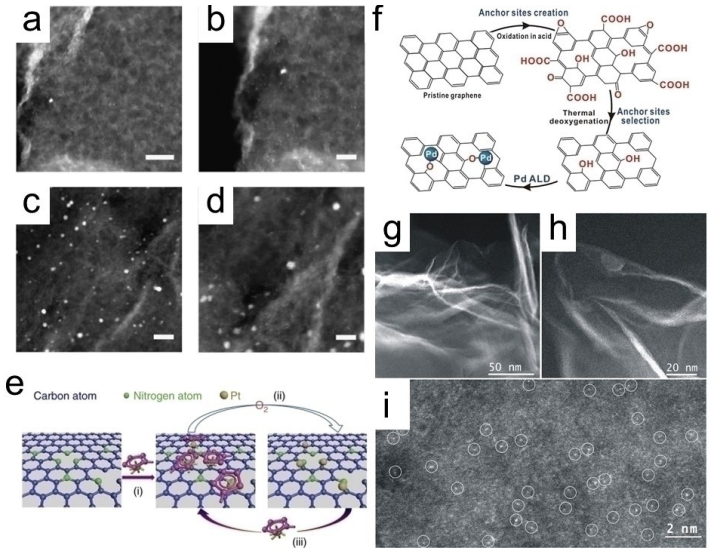


Figure 1.16: **a**, ADF-STEM images of ALDPt/NGNs samples with 50 (**a**, **b**) and 100 (**c**, **d**) ALD cycles. Scale bars, 10 nm (**a**, **c**); 5 nm (**b**, **d**). e, Schematic to show how Pt sites interact with N-doped carbon substrate. Adapted from [37] with permission. **f,** Schematic illustration of single-atom Pd_1/graphene catalyst synthesis via anchor site creation and selection and Pd ALD on pristine graphene. Representative HAADF-STEM images of Pd single sites on graphene at low (**g**, **h**) and high (**i**) magnifications. The white circles highlight the atomically dispersed Pd atoms in the image **(i**). Adapted from [39] with permission.

There are several advantages to use ALD to synthesise SSCs, (1) the desired structure and thickness of SSCs can be precisely controlled by deposition parameters (adjusting the number of cycles); (2) a uniform and reproducible deposition of designed structures and loading can be easily achieved; and (3) this method can be used with many different metal precursors to form SSCs at an atomic level. Generally, ALD is an ideal synthesis method to build uniform model catalysts under controllable conditions, which will be an essential technique for studying their structure-activity relationship using SSCs. Preparing SSCs by ALD is based on the solid covalent interaction between single sites and suitable substrates. This method is ideal for scientific research but is not applicable for large-scale commercial manufacturing due to its high cost.[40]

Another approach to synthesising SSCs bonded to substrates is electrodeposition. The mechanism of this method is to deposit transition metal sites (Pt, Ru, or Co) from counter electrodes or electrolytes on substrates by cathodic cycling. Traditionally, metal sites in electrolytes can immigrate from electrolytes to the working electrode and be deposited onto the surface of substrates to form small particles by applying cyclic voltammetry (CV) cycles

via a three-electrode working station (Fig. 1.17). Yang has prepared atomically Ru-doped MoS_2 co-catalysts for the HER by cycling a MoS_2 on carbon cloth (MoS_2/CC) substrate from -0.5 to 0.4V vs. SCE at a sweep rate of 20 mV/s in an electrolyte containing $RuCl_3$ (1 mmol/L) and H_2SO_4. The Ru-MoS_2/CC co-catalysts exhibit remarkable catalytic activity and stability for the HER in alkaline conditions compared to MoS_2/CC. Density functional theory calculations revealed that the improved catalytic activities stem from the synergistic effect between MoS_2 and single-site Ru.[41]

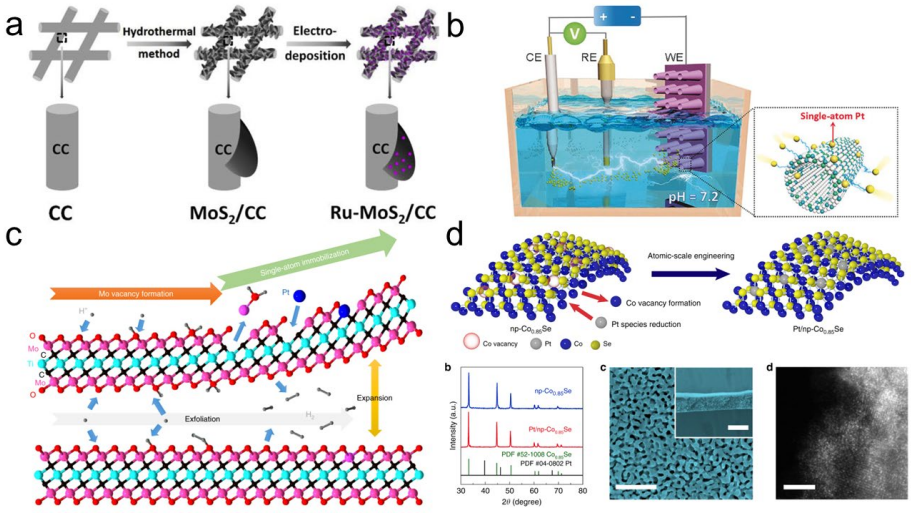


Figure 1.17: a, The fabrication process of Ru-MoS_2/CC co-catalyst by CV cycling. Adapted from [41] with permission. **b**, **c**, **d**, Schematic diagrams of the synthesis processes and the obtained products of Pt SSCs in several nanostructured substrates (CoP, MXene, and CoSe) by potential cycling where Pt is used as the counter electrode. The scale bars are 500 nm and 2 nm in (**d**). Adapted from [42–44] with permission.

Recently, an increasing number of papers have reported that Pt single sites can be doped into transition metal-based substrates by cathodic polarisation treatment, including CoP, MXene, and CoSe.[42–44] The detail of those processes is that during the CV cycles of the electrolytes without Pt precursors, Pt can dissolve into them from the Pt anode. Then the Pt migrates through the electrolyte and anchors onto the surface of the working electrode. Zhang et al. have demonstrated that a potential-cycling method can be used to synthesise a binder-free catalyst comprised of single Pt sites on CoP-based nanotube arrays supported by Ni foam in a neutral media for efficient hydrogen evolution.[42] Wang's group reported that the synthesis

of single platinum sites immobilised on transition metal-based MXene nanosheets with abundant exposed basal planes and Mo vacancies by electrochemical cycling. It has shown enhanced its HER catalytic properties at 30 and 77 mV overpotential to achieve 10 and 100 mA cm^{-2}.[43] Similarly, a single–site platinum decorated nanoporous cobalt selenide that serves as an electrocatalyst for hydrogen evolution has been synthesised by cathodic polarization cycling.[44] Using MoS_2 as an example, it was found that it is energetically favourable to dope Pt single sites and nanocrystals into defects of MoS_2 by electroplating.

However, it has also shown that reducing transition metal sites from solutions makes them easier to grow as small nanoparticles because of the nucleation, chemical, and physical properties of the surface of supports.[45] To synthesise metal sites decorated onto the supports, the surface chemistry of the structure is a vital factor to take into account. Besides, the conduction of CV cycling should also be precisely controlled, such as the potential range, scan rate, and cycle numbers. Although some researchers have reported successfully synthesising single sites onto supports with highly enhanced catalytic activities, there are still two problems that need to be investigated. The loading amount of those single sites is relatively low that inhibits its industrial applications, and there is still no clear evidence to clarify the coordination structures between single sites and substrates.

The pyrolysis synthesis method is one of the most reported strategies to synthesise defect-trapped SSCs on carbon-based or metal oxides substrates. It produces atomically dispersed metal sites from its organic precursors by thermochemically decomposing the structure of the precursor at elevated temperatures under a specific atmosphere. The two main pyrolysis methods can be differentiated based on the number of pyrolysis: one-pot pyrolysis and two-step annealing.

One-pot pyrolysis, as the name suggests, involves pyrolysis of metal precursors (metal-organic frameworks (MOFs), metal phthalocyanine, metal–phenanthroline complexes), and nitrogen or oxygen-containing carbon matrix in tandem at high temperatures (700-1,000 °C). A general approach to synthesising a series of atomically monodispersed transition metal sites

embedded into a nitrogen-doped graphene structure is reported by Fei et al.. Fig. 1.18 shows the formation of what they called M–NHGFs(M = Fe, Co, Ni, and NHGF is nitrogen-doped holey graphene frameworks) structure. Firstly, transition metal precursors ($NiCl_2 \cdot 6H_2O$, $FeCl_3$, $CoCl_2 \cdot 6H_2O$) are mixed with a graphene oxide suspension with the addition of 30% H_2O_2 and sonicated for 1 h. Then, the mixed suspension was hydrothermally treated at 180 °C for 6 h, forming a porous hydrogel. Finally, after freeze drying, the gel was placed in the centre of a 1-inch quartz tube furnace and annealed at 900 °C for 1 h under a continuous flow of Ar (100 sccm) and NH_3 (50 sccm) to obtain their single-site structure (Fig. 1.18a).[46] By using cutting-edge EXAFS and direct atomic STEM images analysis, the structure of the resulting metal sites supported in carbon has been confirmed. They adopt an identical MN_4C_4 configuration with single metal atoms occupying the divacancies in the graphene lattice, such that the distortions to the 2D graphene lattice are as minor as possible (Fig. 1.18b, c, d).[46] Based on the model-led atomic structure, a structure-activity relationship is built by theoretical calculations and experimental studies using those SSCs for the OER reaction. Similarly, Ju et al. synthesised a series of CO_2 reduction catalytically active metal-N_x structures by pyrolysis of a mixture of metal precursors with nitrogen-doped porous carbons and acid washing.[47]

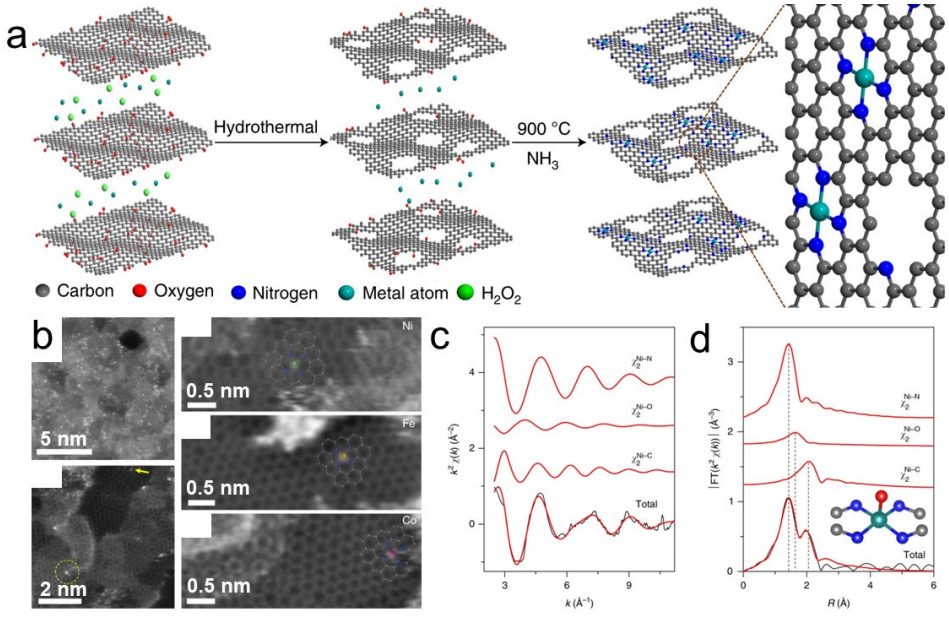


Figure 1.18: a, The preparation route to incorporate N-dopants into the graphene lattice by a thermal annealing process in an NH_3 atmosphere (top). **b**, Atomic structure characterisations

of M–NHGFs by ADF-STEM show that single metal sites are embedded into the defects of N-doped graphene substrate. **c**, A Ni K-edge EXAFS analysis of Ni–NHGF in *k* and *R* spaces, which shows the synthesised Ni SSC is a NiN_4C_4 moiety structure. Adapted from [46] with permission.

Although one-pot pyrolysis has shown potential as a synthesis method for many kinds of SSCs, it struggles to achieve a high enough loading of single sites to meet practical applications. Comparatively, two-step annealing can achieve single-site dispersions with a high areal density of metal contents, maximising the industrial potential of single-site heterogeneous catalysts. To fulfill this goal, a stepwise pyrolysis method was developed by Hai et al., as shown in Fig. 1.19. A nitrogen-doped carbon (NC) substrate was firstly synthesised based on a well-known hydrothermal process. Then, transition metal precursors were anchored on the NC by wet impregnation. Finally, the dried powder mixture was pyrolysed twice. For low-temperature annealing, the powder was heated to 300 °C (heating rate, 5 °C min^{-1}) for 5 hrs under a flow of nitrogen gas. After thorough washing using a water-ethanol mixture, the dried powders (80 °C) were subjected to high-temperature annealing at 550 °C (heating rate, 2 °C min^{-1}) for 5 hrs under a constant flow of nitrogen gas. They synthesised ultra-high-density single-site catalysts with metal contents up to 23 wt% for 15 metals on different carriers.[48] The mechanism behind this method initially involves removing the weakly interacting species that would otherwise aggregate upon complete decomposition at high temperatures through low-temperature annealing and ethanol washing. The stable single sites can then remain isolated through graphitisation above 500 °C.

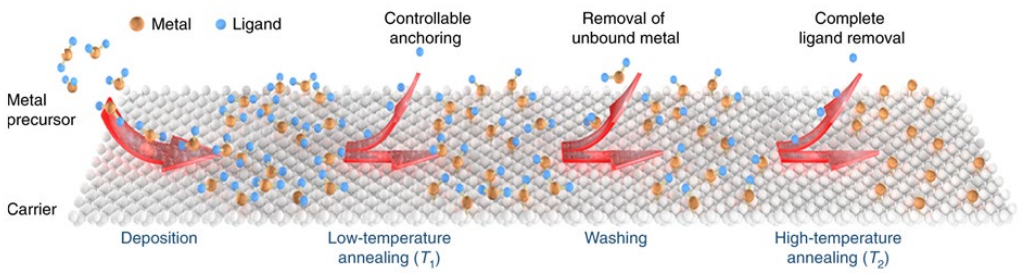


Figure 1.19: Strategy for preparing ultrahigh loading of SSCs by two-step annealing. Adapted from [48] with permission.

The pyrolysis method is straightforward and very suitable for synthesising SSCs embedded in carbon substrates for electrochemical applications due to their high electrical conductivity and electrochemical stability.[49] The process is to decompose metal precursors with heat treatment. Then N/O ligands can then bond to the single-site materials to keep them isolated during the transformation to embedded SSCs. After graphitisation at high temperatures, a metal-nitrogen/oxygen-carbon (referred to as M-N/O-C) structure will form. Pyrolysis is a mature technology to synthesise large-scale SSCs but is energy intensive due to the need to reach high temperatures during pyrolysis, which is not environmental-friendly.

There are two other related methods that have been reported to synthesise SSCs in addition to the two mentioned above. The first one involves metal site trapping at high temperatures. Wei et al. have described an unexpected phenomenon such that noble metal nanoparticles (Pd, Pt, Au-NPs) can be transformed into thermally stable single sites trapped on an N-doped carbon substrate (Pd, Pt, Au-SAs) above 900 °C in an inert atmosphere (Fig. 1.20a-g). By using in-situ environmental transmission electron microscopy, it was found that there is competition between the sintering and atomisation processes during the conversion from nanoparticles to single sites. Below 900 °C, Pd nanoparticles tend to grow and sinter with increasing temperature. However, after the temperature reaches 1,000 °C, uncontrolled movement and intense collisions within the supports occur, and the Pd nanoparticles shrink and eventually vanish. Density functional theory calculations further reveal that the nanoparticle to single site conversion at high temperature is driven by the formation of the more thermodynamically stable Pd-N_4 structure as mobile Pd sites are captured on the defects of nitrogen-doped carbon.[50] Atom trapping is a unique top-down method to synthesise SSCs. Similar transition metal SSCs prepared by atom trapping of bulk metals have also been reported.[51, 52]

Another method is called one-step flame spray pyrolysis. By using cerium and palladium acetylacetonates as precursors in the flame spray pyrolysis (FSP) technique, Pd single sites atomically disperse on the defects of crystalline CeO_2 with a high surface area. As confirmed

by several advanced characterisation techniques in Fig. 1.20 h and i, those Pd single sites are incorporated into the ceria lattice during the FSP preparation. Compared to the isolated ion Pd^{2+} single sites prepared by impregnation, Pd SSCs synthesised by FSP show high resistance to sintering under CO oxidation conditions, as observed by in-situ X-ray-based spectroscopies.[53]

In conclusion, pyrolysis is the most highly reported method to synthesise well-defined SSCs. It is a robust and scalable method that could achieve large-scale manufacture. This is especially true for electrochemical applications, where stable single sites embedded into the defects of carbon substrates are the best choice. However, pyrolysis processes are energy intense, which raises concern about their environmental benefit.

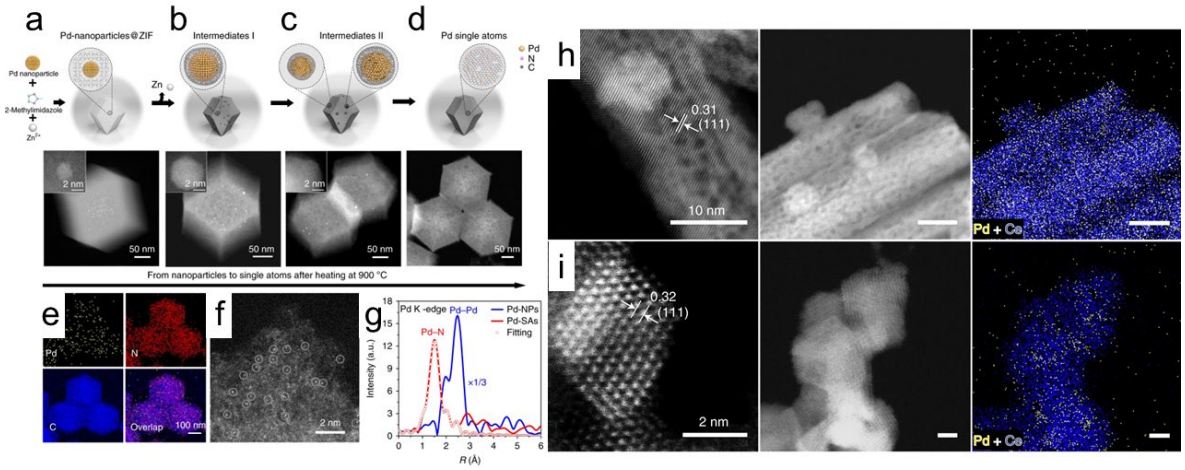


Figure 1.20: a–d, HAADF-STEM images, and high-resolution HAADF-STEM images (insets) of Pd-nanoparticles@ZIF-8 (**a**), intermediate I (**b**), intermediate II (**c**), and Pd single atoms (**d**). **e**, Energy dispersive X-ray spectroscopy elemental mapping results of Pd-SAs, showing Pd homogeneously distributed across the pyrolyzed sample. **f**, High-resolution STEM image of Pd-SAs suggests Pd was atomically dispersed on the substrate. **g**, Fourier transforms of k^3-weighted Pd K-edge EXAFS experimental data for Pd-NPs and Pd-SAs, showing the coordinating atoms adjacent to Pd atoms before and after pyrolysis. Adapted from [50] with permission. **h**, **i**, HAADF-STEM and EDX-mapping images of 1PdRods (**h**) and 1Pd SSC prepared by flame spray pyrolysis (**i**). The spacing of the corresponding crystal planes is indicated (nm). Adapted from [53] with permission.

1.6.2.4 Synthesis of Pt SSCs for the HER

Thanks to the significant efforts devoted to developing new SSCs, more than ten methods have been reported to synthesise SSCs. The synthesised SSCs can be summarised into three

different types based on the interactions between the SSCs and the substrate: (1) SSCs physically adsorbed on substrates, (2) SSCs chemically bonded with the ligands of substrates, and (3) SSCs trapped at the defects of substrates. These three types of single-site structures may demonstrate different behaviours under electrochemical processes. However, there is a lack of systematic investigation into how interactions between single sites and substrates affect their activity and stability for the HER. Therefore, my DPhil projects will focus on synthesising three types of Pt SSCs on carbon substrates by physical interaction, chemical impregnation, and pyrolysis, respectively; and clarifying their structure, formation mechanism, and activity for the HER.

1.6.3 Pt SSCs for the HER

After synthesising Pt SSCs and defining the structure of Pt SSCs, their activity for the HER can be evaluated, and structure-activity relationships should be built.

To estimate the HER rate of metal electrodes, a volcano relationship plot has been established by DFT-based calculations of the exchange-current density against the free energy of catalysts.[54] Pt metal electrodes have been located at the top of the volcano and are regarded as the most efficient metal catalyst for the HER with near thermo-neutral free energy.[55] The previous experiments confirm that the Pt nanoparticles hold a great intrinsic activity for the acidic HER.[56] Similarly, to explore the activity of SSCs for the HER, a series of late transition metal atoms trapped on a C_9N_4 monolayer (TM@C_9N_4, where TM represents Mn, Fe, Co, Ni, Cu, Ru, Rh, Pd, Ir, and Pt) as electrocatalysts have been screened based on the first-principle calculations. The results show that the metal sites in the Co@C_9N_4, Ni@C_9N_4, and Pt@C_9N_4 systems demonstrate a higher exchange current density for the HER (Fig. 1.21).[57] Pt SSCs supported on carbon supports are promising catalysts with the potential to demonstrate the sufficient activity with a low Pt loading. However, the HER activity of Pt SSCs supported on carbon substrates has not been precisely evaluated by experiments, and there are still some controversies.

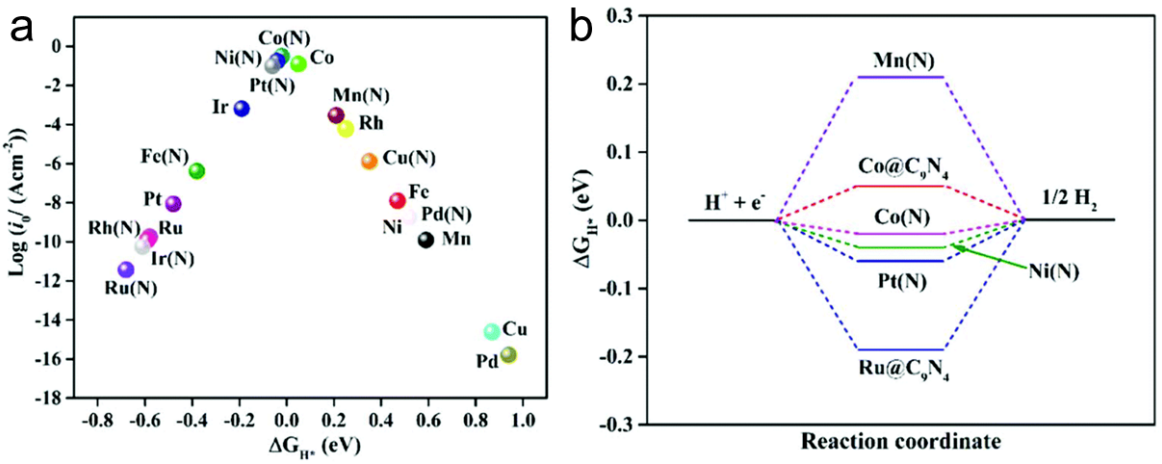


Figure 1.21: a, HER volcano curve of exchange current (i_0) related to the adsorption Gibbs free energy of hydrogen (ΔG_{H^*}) adsorbed on the different active sites of TM@C_9N_4 catalysts. **b**, The calculated ΔG_{H^*} value for the TM and N atoms in the TM@C_9N_4 catalysts. Adapted from [57] with permission.

Some examples show that Pt-based SSCs with a Pt oxidation state at +2 have a better activity and stability for the HER than metallic Pt nanoparticles. The Sun's group synthesised Pt single sites at an oxidation state of +2 deposited on N-doped carbon nanosheets (Pt_1/NCNS) by ALD. As shown in Fig. 1.22a, the Pt_1/NCNS displays a similar activity as their metallic nanoparticles counterparts (Pt-SNs/NCNS) with a much lower amount of Pt content. Further, its calculated mass activity at the overpotential of 0.05 V is 7.1 A mg^{-1}_{Pt} mass, which is more than 4 times greater than that of the Pt-SNs/NCNS catalyst (1.6 A mg^{-1}). The operando XAS experiments proposed that the superior HER activity comes from the higher total unoccupied density of states of Pt 5*d* orbitals of Pt sites.[38] Adjusting the substrate from N-doped graphene to curved onion-like carbon nanospheres, a low overpotential (38 mV at 10 mA cm^{-2}) and high turnover frequencies (40.78 H_2 s^{-1} at 100 mV) for the HER are achieved by oxidised Pt (+2) SSC with a Pt loading of 0.27 wt% (Fig. 1.22b). From the first-principle calculations, the curved carbon support promotes the kinetics of the HER by a tip-enhanced local electronic field at the Pt sites.[58] Similarly, Yin et al. have reported that Pt (+2) single sites can be anchored on graphdiyne for hydrogen evolution (Fig. 1.22c).[59] These Pt single sites can reach outstanding mass activities of 23.64 A mg^{-1} at an overpotential of 0.1 V. This excellent HER performance originates from the solid electronic coupling between the Pt single sites and the substrate graphdiyne.

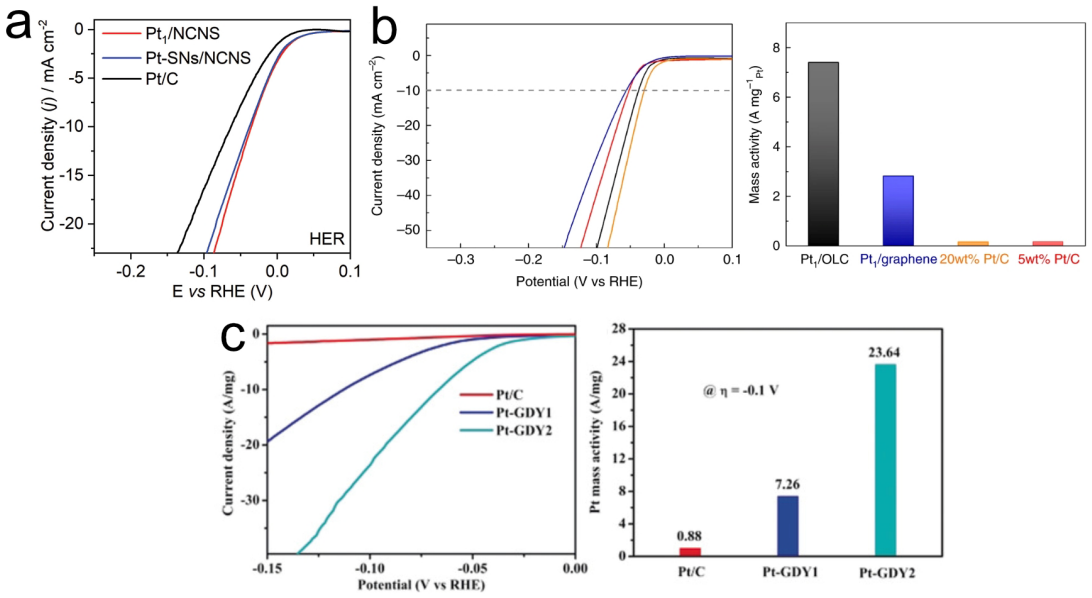


Figure 1.22: Electrocatalytic performance of Pt SSCs in hydrogen evolution reaction. **a**, Polarisation curves of Pt_1/NCNS, Pt-SNs/NCNS, and Pt/C for the HER. Adapted from [38] with permission. **b**, Polarisation curves and corresponding mass activity of Pt single sites on onion-like carbon support in comparison with 5 wt% and 20 wt% commercial Pt/C (red and orange, respectively) and Pt single sites on N-doped graphene (Pt_1/graphene, blue) in a 0.5 M H_2SO_4 electrolyte. Adapted from [58] with permission. **c**, The polarisation curves and derived mass activities for Pt singles on graphdiyne, and commercial Pt/C in 0.5 M H_2SO_4 solutions, with a scan rate of 5 mV s^{-1}. Adapted from [59] with permission.

But recent evidence shows those Pt single sites will be reduced to near metallic states or Pt nanoparticles to produce hydrogen. Firstly, Yao's group prepared an atomically dispersed Pt on a metal-organic framework derived N-doped carbon (designated as Pt_1/N-C) via ALD. Using operando XAS, they found that the Pt sites can exhibit very high hydrogen evolution activity with only 19 mV overpotential at 10 mA cm^{-2} when these Pt sites evolve into a near-free state (Fig. 1.23a, c).[60] Chen's group synthesised a Pt SSC trapped into an N-doped carbon by single-step thermal pyrolysis (denoted as Pt_{SA}/N–C). Then, by probing the dynamic structure of Pt single-site centres during the acidic HER process, they observed that the as-prepared Pt_{SA}/N–C shows continuously improved HER performance once it was reduced to form metallic clusters by the repetitive LSV and CV scanning (Fig. 1.23b, d).[61]

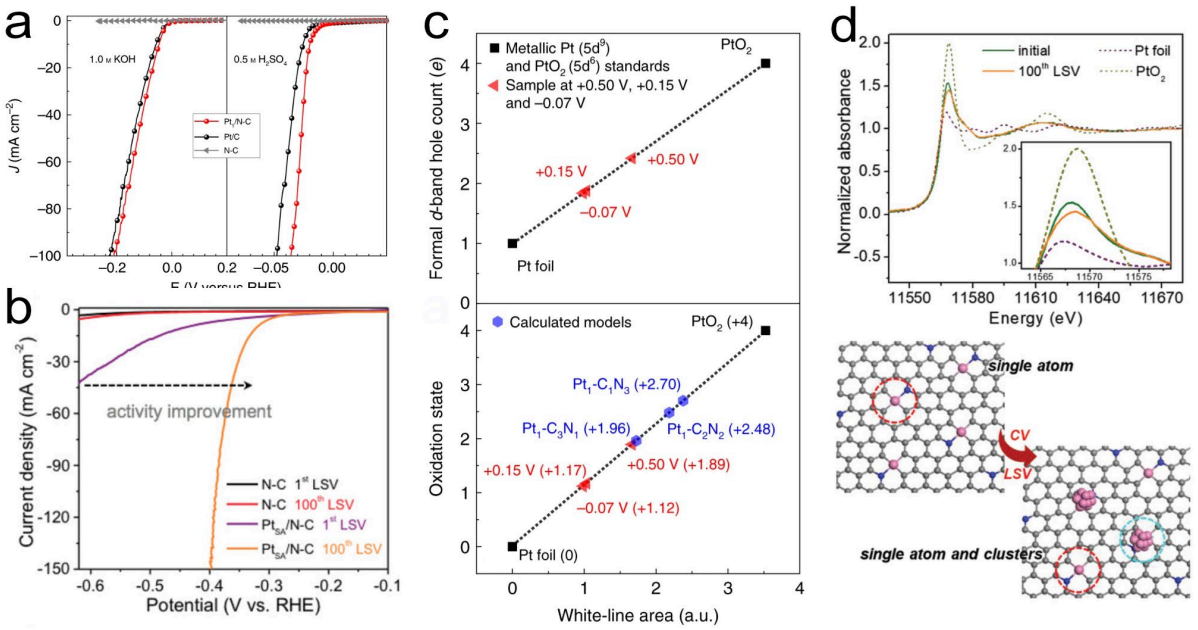


Figure 1.23: a, Polarisation curves of Pt_1/N-C, Pt/C, and N-doped framework for the HER at acidic solutions. **b**, HER polarisation curves of Pt_{SA}/N-C and N-doped carbon substrate with their 1st and 100th measurement in a 0.5 M H_2SO_4 electrolyte. **c**, The fitted average formal *d*-band hole counts and oxidation states of Pt from ΔXANES spectra indicate that Pt sites are reduced to a near-metallic state at the HER working conditions. **d**, The normalised XANES at the Pt L_3-edge of Pt_{SA}/N–C recorded during the repetitive LSV scanning, which shows the Pt sites are reduced as the schematic illustrated. (**a**) and (**c**) adapted from [60] with permission, and (**b**) and (**d**) are adapted from [61] with permission

Many studies have reported that the oxidised Pt SSCs on carbon supports can exhibit a superior activity for the HER and related these activities to their unique electronic properties and local structures based on theoretical models. Due to the lack of well-defined atomic structure and limitations of ex-situ characterisation, the desired structure of Pt SSCs for the HER is highly debated now. Several operando experiments have proposed that Pt metallic sites or clusters may be the truly active structure for the HER.

1.7 Aim and structure of this project

As discussed in this chapter, due to the requirements of the net zero emissions scenario, TW-scale hydrogen production must be achieved by water electrolysis by 2035. Due to the dramatic cost reduction of renewable electricity and the increasing load factor of electrolysers, PEM water electrolysis will become a cost-competitive technique to produce green hydrogen. This will lead to a surge in demand for precious metals to be employed as electrocatalysts. To

achieve the TW-scale green hydrogen target, the loading of the precious metals currently used in PEM water electrolysers must be reduced. SSCs, as a new frontier in heterogeneous catalysis, can maximise the utilisation of metal atoms and achieve high catalytic activity and long-time stability with their unique electronic structures. Therefore, SSCs may significantly reduce the cost of precious catalysts (Pt and Ir) used in acidic PEM water electrolysers.

After reviewing the literature, most transition metal-based SSCs with a metal site embedded into an N-doped carbon structure still need ~100 mV larger overpotential to reach a current density of 10 mA cm^{-2} than commercial Pt nanoparticles on active carbon. This thermodynamic disadvantage will decrease the energy efficiency of the whole water electrolyser. Comparatively, Pt SSCs on carbon substrates show competitive activity and stability for the HER. Therefore, synthesising Pt SSCs to achieve superior HER activity with extremely low Pt loadings looks very promising. Tens of synthesis methods have been described to synthesise SSCs. Several cutting-edge characterisation techniques have been developed to clarify the as-synthesised structure and its active structure under working conditions. Most Pt SSCs are proposed with promising HER activity and stability, but it is not necessarily true.

Before Pt SSCs can be successfully employed to produce hydrogen, there are still some fundamental points needed to be better understood: (1) how to enable large-scale synthesis of stable and well-dispersed Pt SSCs; (2) how to clarify the structure and formation mechanism of Pt SSCs using advanced and complementary characterisation techniques, such as atomic resolution STEM and XAS; (3) how to determine the activity and stability of Pt SSCs for the HER using a method that is well-accepted and non-controversial; and (4) how to use in-situ or operando techniques to investigate the structural transformations of Pt SSCs at working potentials for the HER.

Therefore, the main focus of this project is to explore the synthesis, characterisation, and catalytic mechanism of Pt SSCs on carbon substrates for the HER. To achieve this target, three different types of Pt SSCs were initially synthesised, as defined by the interaction between the single site and the substrate: (1) Pt single-site complexes physically adsorbed

onto graphene (Fig. 1.24a), (2) Pt SSCs chemically bonded to the surface of a polyaniline substrate (Fig. 1.24b), and (3) Pt SSCs trapped at defects in graphene prepared by pyrolysis (Fig. 1.24c). Secondly, complementary ex-situ and in-situ characterisation techniques, including high-resolution STEM, XAS, X-ray photoelectron spectroscopy (XPS), Raman spectroscopy, and Fourier-transform infrared spectroscopy (FTIR), were used to clarify their physical and chemical structures and formation mechanisms at an atomic level. Thirdly, their HER activity in acidic electrolytes was tested, and operando XAS techniques were used to track the structural evolution of Pt SSCs at working potentials. Finally, structure-activity relationships were established based on their well-defined structures and operando XAS experiments.

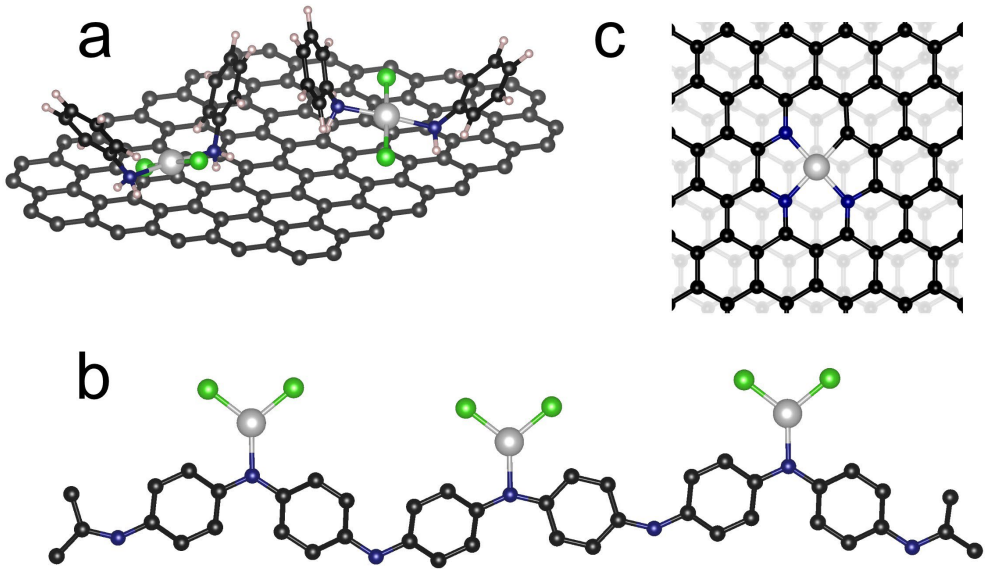


Figure 1.24: a, **b**, **c**, The schematics of the physically adsorbed (**a**), chemically adsorbed (**b**), and defect-trapped (**c**) Pt SSCs on carbon-based substrates.

Specifically, in Chapter 3, a Pt single-site complex catalyst (Pt sites atomically bonded to aniline and Cl ligands) was physically adsorbed on a thin graphene substrate. The physical structure was imaged by atomic resolution STEM, and its chemical bonding environment was clarified by ex-situ XAS, XPS, and Raman spectroscopy. Finally, the activity of this model Pt SSC for the HER was investigated, and its structure at working potential was recorded by operando XAS. The structural changes were then correlated with activity. Our model catalysts

and operando experiments elucidate how physically adsorbed Pt SSCs behave during the HER at working potentials.

In Chapter 4, Pt single sites were anchored on a polyaniline substrate (Pt-PANI) using wetness impregnation. Due to the high number of N sites and porous structure of the polyaniline substrates, atomically dispersed Pt sites can be formed on polyaniline with up to a 10 wt% loading, as demonstrated by atomic STEM images. By using FT-IR and XAS, it was found that Pt is bonded with the N sites on polyaniline and Cl ligands from the precursor. The electrochemical activity of this Pt-PANI for the HER was also investigated by testing it in a static three-electrode setup.

In Chapter 5, following the synthesis of atomically dispersed Pt-PANI in Chapter 4, a stable Pt SSC trapped into a carbon substrate (graphitised carbon) was synthesised by pyrolysing the Pt-PANI sample. Ex-situ XAS and X-ray photoemission spectroscopy (XPS) confirmed that the Pt is atomically bonded with N at an oxidation state between 0 and +2, and the Raman spectra show that the polyaniline substrate is transformed into distorted graphene. Then, to clarify the structure and formation mechanism of trapped Pt SSCs prepared by pyrolysis, in-situ heating STEM and temperature-dependent XPS were employed to track the physical and chemical structure evolution of Pt during pyrolysis. After obtaining a representative Pt SSC by adjusting the Pt loading, the HER activity for the trapped Pt SSC was evaluated and compared with commercial Pt/C catalysts in a well-designed electrochemical testing setup. Finally, the active structure of the trapped Pt SSC at working potentials was recorded by the operando XAS experiments. Combined with density functional calculations, the mechanism of the trapped Pt SSC for the HER is clarified.

1.8 References

1. IEA (2021), *Global Energy Review 2021*, IEA, Paris

2. Mountford H, Waskow D, Gonzalez L, et al. COP26: Key Outcomes from the UN Climate Talks in Glasgow (2021).

3. Holleman, A. F., Egon Wiberg, and Nils Wiberg. *Inorganic chemistry*. Academic press, 2001.

4. Nazir H, Muthuswamy N, Louis C, et al. Is the H_2 economy realizable in the foreseeable future? Part II: H_2 storage, transportation, and distribution. *International journal of hydrogen energy*, 45(41): 20693-20708, (2020).

5. IEA (2022), *Hydrogen*, IEA, Paris

6. Great Britain. Department for Business, E. & I. Strategy. *UK Hydrogen Strategy*.

7. IRENA (2020), Green Hydrogen Cost Reduction: Scaling up Electrolysers to Meet the 1.5 ºC Climate Goal.

8. IRENA (2020), Renewable Power Generation Costs in 2020.

9. Lagadec, M. F. & Grimaud, A. Water electrolysers with closed and open electrochemical systems. *Nature Materials 2020 19:11* **19**, 1140–1150 (2020).

10. Hydrogen Production Costs 2021. (2021).

11. Barelli, L., Bidini, G. & Cinti, G. Airflow Management in Solid Oxide Electrolyzer (SOE) Operation: Performance Analysis. *ChemEngineering* 2017, Vol. 1, Page 13 1, 13 (2017).

12. Chisholm, G., Kitson, P. J., Kirkaldy, N. D., Bloor, L. G. & Cronin, L. 3D printed flow plates for the electrolysis of water: an economic and adaptable approach to device manufacture. *Energy Environ Sci* **7**, 3026–3032 (2014).

13. Bernt, M., Siebel, A. & Gasteiger, H. A. Analysis of Voltage Losses in PEM Water Electrolyzers with Low Platinum Group Metal Loadings. *J Electrochem Soc* **165**, F305–F314 (2018).

14. Ifkovits, Z. P., Evans, J. M., Meier, M. C., Papadantonakis, K. M. & Lewis, N. S. Decoupled electrochemical water-splitting systems: a review and perspective. *Energy Environ Sci* **14**, 4740–4759 (2021).

15. Bernt, M. & Gasteiger, H. A. Influence of Ionomer Content in IrO_2/TiO_2 Electrodes on PEM Water Electrolyzer Performance. *J Electrochem Soc* **163**, F3179–F3189 (2016).

16. Mayyas, A., Ruth, M., Pivovar, B., Bender, G. & Wipke, K. Manufacturing Cost Analysis for Proton Exchange Membrane Water Electrolyzers. (2019).

17. Kibsgaard, J. & Chorkendorff, I. Considerations for the scaling-up of water splitting catalysts. *Nature Energy 2019 4:6* **4**, 430–433 (2019).

18. McCrory, C. C. L. et al. Benchmarking Hydrogen Evolving Reaction and Oxygen Evolving Reaction Electrocatalysts for Solar Water Splitting Devices. *J Am Chem Soc* **137**, 4347–4357 (2015).

19. King, L. A. et al. A non-precious metal hydrogen catalyst in a commercial polymer electrolyte membrane electrolyser. *Nature Nanotechnology 2019 14:11* **14**, 1071–1074 (2019).

20. Yang, J. et al. Ultrahigh-current-density niobium disulfide catalysts for hydrogen evolution. *Nature Materials 2019 18:12* **18**, 1309–1314 (2019).

21. Petek, U., Ruiz-Zepeda, F., Bele, M. & Gaberšček, M. Nanoparticles and Single Atoms in Commercial Carbon-Supported Platinum-Group Metal Catalysts. *Catalysts* 2019, Vol. 9, Page 134 9, 134 (2019).

22. Zalitis, C. M., Kucernak, A. R., Sharman, J. & Wright, E. Design principles for platinum nanoparticles catalysing electrochemical hydrogen evolution and oxidation reactions: edges are much more active than facets. *J Mater Chem A Mater* **5**, 23328–23338 (2017).

23. Wei, G. F. & Liu, Z. P. Restructuring and Hydrogen Evolution on Pt Nanoparticle. *Chem Sci* **6**, 1485–1490 (2015).

24. Yang, X. F. et al. Single-atom catalysts: A new frontier in heterogeneous catalysis. *Acc Chem Res* **46**, 1740–1748 (2013).

25. Yang, J., Li, W., Wang, D. & Li, Y. Electronic Metal–Support Interaction of Single-Atom Catalysts and Applications in Electrocatalysis. *Advanced Materials* **32**, 2003300 (2020).

26. Qi, K., Chhowalla, M. & Voiry, D. Single atom is not alone: Metal–support interactions in single-atom catalysis. *Materials Today* **40**, 173–192 (2020).

27. Jiao, L. & Regalbuto, J. R. The synthesis of highly dispersed noble and base metals on silica via strong electrostatic adsorption: I. Amorphous silica. *J Catal* **260**, 329–341 (2008).

28. Lambert, S. et al. Synthesis of very highly dispersed platinum catalysts supported on carbon xerogels by the strong electrostatic adsorption method. *J Catal* **261**, 23–33 (2009).

29. Pillay, D. & Johannes, M. D. Effect of S on Pt(111) and Pt_3Ni(111) Surfaces: A First Principles Study. *Journal of Physical Chemistry C* **112**, 1544–1551 (2008).

30. Ye, S. et al. Highly stable single Pt atomic sites anchored on aniline-stacked graphene for hydrogen evolution reaction. *Energy Environ Sci* **12**, 1000–1007 (2019).

31. Thomas, J. M., Raja, R. & Lewis, D. W. Single-Site Heterogeneous Catalysts. *Angewandte Chemie International Edition* **44**, 6456–6482 (2005).

32. Kwak, J. H. et al. Coordinatively unsaturated Al^{3+} centers as binding sites for active catalyst phases of platinum on γ-Al_2O_3. *Science* (1979) **325**, 1670–1673 (2009).

33. Kim, J. et al. Highly Durable Platinum Single-Atom Alloy Catalyst for Electrochemical Reactions. *Adv Energy Mater* **8**, 1701476 (2018).

34. Copéret, C. Single-Sites and Nanoparticles at Tailored Interfaces Prepared via Surface Organometallic Chemistry from Thermolytic Molecular Precursors. *Acc Chem Res* **52**, 1697–1708 (2019).

35. Liu, P., Huang, X., Mance, D. & Copéret, C. Atomically dispersed iridium on MgO(111) nanosheets catalyses benzene–ethylene coupling towards styrene. *Nature Catalysis 2021 4:11* **4**, 968–975 (2021).

36. Samantaray, M. K. et al. Surface organometallic chemistry in heterogeneous catalysis. *Chem Soc Rev* **47**, 8403–8437 (2018).

37. Cheng, N. et al. Platinum single-atom and cluster catalysis of the hydrogen evolution reaction. *Nature Communications 2016 7:1* **7**, 1–9 (2016).

38. Li, J. et al. Unveiling the Nature of Pt Single-Atom Catalyst during Electrocatalytic Hydrogen Evolution and Oxygen Reduction Reactions. *Small* **17**, 2007245 (2021).

39. Yan, H. et al. Single-Atom Pd1/Graphene Catalyst Achieved by Atomic Layer Deposition: Remarkable Performance in Selective Hydrogenation of 1,3-Butadiene. *J Am Chem Soc* **137**, 10484–10487 (2015).

40. Fonseca, J. & Lu, J. Single-Atom Catalysts Designed and Prepared by the Atomic Layer Deposition Technique. *ACS Catal* **11**, 7018–7059 (2021).

41. Wang, D., Li, Q., Han, C., Xing, Z. & Yang, X. Single-atom ruthenium based catalyst for enhanced hydrogen evolution. *Appl Catal B* **249**, 91–97 (2019).

42. Zhang, L., Han, L., Liu, H., Liu, X. & Luo, J. Potential-Cycling Synthesis of Single Platinum Atoms for Efficient Hydrogen Evolution in Neutral Media. *Angewandte Chemie International Edition* **56**, 13694–13698 (2017).

43. Zhang, J. et al. Single platinum atoms immobilized on an MXene as an efficient catalyst for the hydrogen evolution reaction. *Nature Catalysis 2018 1:12* **1**, 985–992 (2018).

44. Jiang, K. et al. Single platinum atoms embedded in nanoporous cobalt selenide as electrocatalyst for accelerating hydrogen evolution reaction. *Nature Communications 2019 10:1* **10**, 1–9 (2019).

45. Tang, K., Wang, X., Li, Q. & Yan, C. High Edge Selectivity of In Situ Electrochemical Pt Deposition on Edge-Rich Layered WS_2 Nanosheets. *Advanced Materials* **30**, 1704779 (2018).

46. Fei, H. et al. General synthesis and definitive structural identification of MN_4C_4 single-atom catalysts with tunable electrocatalytic activities. *Nature Catalysis 2018 1:1* **1**, 63–72 (2018).

47. Ju, W. et al. Understanding activity and selectivity of metal-nitrogen-doped carbon catalysts for electrochemical reduction of CO_2. *Nature Communications 2017 8:1* **8**, 1–9 (2017).

48. Hai, X. et al. Scalable two-step annealing method for preparing ultra-high-density single-atom catalyst libraries. *Nature Nanotechnology 2021 17:2* **17**, 174–181 (2021).

49. Peng, Y., Lu, B. & Chen, S. Carbon-Supported Single Atom Catalysts for Electrochemical Energy Conversion and Storage. *Advanced Materials* **30**, 1801995 (2018).

50. Wei, S. et al. Direct observation of noble metal nanoparticles transforming to thermally stable single atoms. *Nature Nanotechnology 2018 13:9* **13**, 856–861 (2018).

51. Qu, Y. et al. Direct transformation of bulk copper into copper single sites via emitting and trapping of atoms. *Nature Catalysis 2018 1:10* **1**, 781–786 (2018).

52. Yang, J. et al. In Situ Thermal Atomization To Convert Supported Nickel Nanoparticles into Surface-Bound Nickel Single-Atom Catalysts. *Angewandte Chemie International Edition* **57**, 14095–14100 (2018).

53. Muravev, V. et al. Interface dynamics of Pd–CeO_2 single-atom catalysts during CO oxidation. *Nature Catalysis 2021 4:6* **4**, 469–478 (2021).

54. Nørskov, J. K. et al. Trends in the Exchange Current for Hydrogen Evolution. *J Electrochem Soc* **152**, J23 (2005).

55. Skúlason, E. et al. Modeling the electrochemical hydrogen oxidation and evolution reactions on the basis of density functional theory calculations. *Journal of Physical Chemistry C* **114**, 18182–18197 (2010).

56. Hansen, J. N. et al. Is There Anything Better than Pt for HER? *ACS Energy Lett* **6**, 1175–1180 (2021).

57. Zhou, Y., Gao, G., Kang, J., Chu, W. & Wang, L. W. Computational screening of transition-metal single atom doped C_9N_4 monolayers as efficient electrocatalysts for water splitting. *Nanoscale* **11**, 18169–18175 (2019).

58. Liu, D. et al. Atomically dispersed platinum supported on curved carbon supports for efficient electrocatalytic hydrogen evolution. *Nature Energy 2019 4:6* **4**, 512–518 (2019).

59. Yin, X. P. et al. Engineering the Coordination Environment of Single-Atom Platinum Anchored on Graphdiyne for Optimizing Electrocatalytic Hydrogen Evolution. *Angewandte Chemie International Edition* **57**, 9382–9386 (2018).

60. Fang, S. et al. Uncovering near-free platinum single-atom dynamics during electrochemical hydrogen evolution reaction. *Nature Communications 2020 11:1* **11**, 1–8 (2020).

61. Wang, J. et al. In Situ Identifying the Dynamic Structure behind Activity of Atomically Dispersed Platinum Catalyst toward Hydrogen Evolution Reaction. *Small* **17**, 2005713 (2021).

Chapter 2

Methodology

2.1 Materials preparation

2.1.1 Thin-layer graphene substrate grown by the CVD method

The thin-layer graphene nanosheets used in Chapter 3 are synthesised by a well-established chemical vapour deposition (CVD) method.[1] It has been reported that low-pressure CVD can synthesise one-layer or bilayer graphene films with high coverage, an ideal material to be employed as a substrate to support single-site catalysts. The details of growing thin-layer graphene by our CVD method are described as follows.

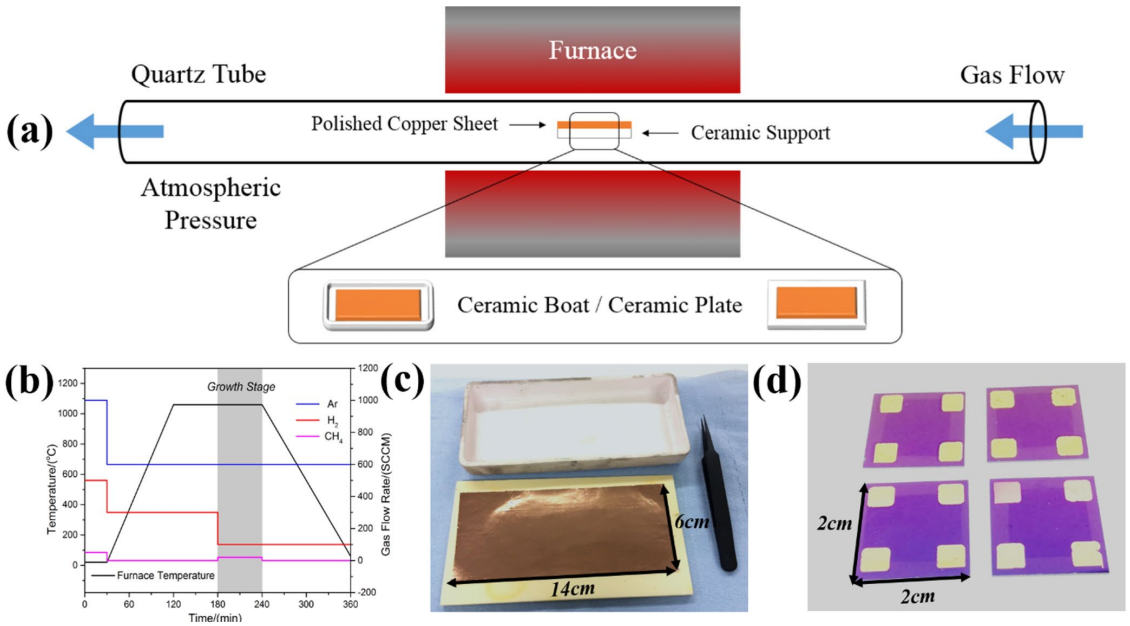


Figure 2.1: Atmospheric pressure CVD synthesis of large-area thin layer graphene on copper. **a**, Schematic illustration of the CVD experimental set-up with a polished copper sheet in a ceramic boat or a flat ceramic plate. **b**, Temperature profiles of the furnace as a function of time and the gas flow rate of argon, hydrogen, and methane during the growth, respectively. Black line: furnace temperature. Blue line: argon. Red line: hydrogen. Magenta line: methane. **c**, Photo of a large-area graphene sheet on copper. The image also displays the ceramic boat

and plate used during the graphene synthesis. **d**, Photograph of four transferred graphene samples on SiO_2/Si with pre-patterned metal contacts. Adapted from [1] with permission.

A piece of copper foil (99.8%, Goodfellow) with a thickness of 25 μm and an area of ~14 cm by ~6 cm was first polished for at least 15 mins. Then, to remove the oxides residues on the copper foil surface, it was sonicated in diluted hydrochloric acid (HCl) solution (1 M) for two mins, followed by acetone and isopropanol (IPA) for 5 mins each. Finally, the whole piece of copper was put into a ceramic plate and placed into an air-tight 4-inch quartz tube. A horizontal tube furnace with an accompanying control unit (Carbolite model HST 12/400) was moved to the sample's position by sliding it across mounted runners. To ensure a uniform temperature during growth, the copper sheet was positioned in the centre of the furnace, as shown in Fig. 2.1a. Three gases (BOC) were used to grow graphene nanosheets in our experiments: 1% methane in argon, 25% hydrogen in argon, and 100% argon (referred to as CH_4, H_2, and Ar, respectively). The flow rate of these gases could be individually controlled using Alicat mass flow controllers in conjunction with Flowvision computer software and was measured in standard cubic centimetres per minute (sccm).

The CVD growth was performed at atmospheric pressure and was first flushed with 1000 sccm Ar, 500 sccm H_2, and 50 sccm CH_4 for 30 mins to remove all gases from the air. Then, as Fig. 2.1b shows, the furnace temperature increased to 1065 °C at a ramping rate of 50 °C/min under a flow of 600 sccm of Ar and 300 sccm of H_2. After the furnace reached 1065 °C, the copper was annealed at this temperature with the same flow rate for one hour. Graphene growth was carried out at 1065 °C under a flow of 600 sccm of Ar, 100 sccm of H_2, and 20 sccm of CH_4 for one hour. After growth, the furnace slid away from the sample to the other end of the runners, which allowed the sample to be fast-cooled to room temperature (RT) (Fig. 2.1c, d).

2.1.2 Wet impregnation of Pt sites

Impregnation and drying is a frequently used method for preparing heterogeneous catalysts because of its technical simplicity, low cost, and limited waste. Generally, it is to mix a metal

precursor solution with porous support and then to be dried. The dry product is further treated through activation processes (calcination or reduction) to obtain the desired catalyst.

Inorganic metal salts, including metal chlorides, nitrates, acetates, carbonates, and organic metal complexes, such as metal acetylacetonates, are common precursors used in impregnation methods. Water is the most commonly used solvent for inorganic salts because of the high solubility of many inorganic precursors, whereas organic solvents are mainly used for organometallic precursors. Concentrations below (super)saturation are required to prevent premature deposition of the metal precursor in bulk solution.[2]

The impregnation methods can be divided into two main types: wet impregnation and incipient wetness impregnation. Wet impregnation is when catalyst precursors are dissolved into a solution with a volume larger than the pore volume, and metal ions are anchored on supports by the interaction with the surface groups of the support after removal of the water solution by filtration or centrifuging. Comparatively, the incipient wetness impregnation is simply dissolving metal precursors in the impregnating solution, which is made to match the pore volume of the support. The metal loading is thus controlled by the concentration of metal ions in the solution, meaning that the support surface does not play an important role but merely acts as physical support and keeps a dry character on a macroscopic scale.[3]

Therefore, due to its simple procedure and controllable conditions, wet impregnation methods have been demonstrated to be efficient in preparing precious group metal catalysts.[4] The preparative process begins with dissolving metal precursors in a solvent of adequate solubility and volatility and adding the solution dropwise onto support under vigorous stirring. The resultant mixture is dried to remove the residual solvent and then treated to obtain the final products.

In Chapter 3, to synthesise the physically adsorbed Pt SSC, I used aniline molecules modified graphene as supporting materials to impregnate with the Pt sites in an ethanol solution of H_2PtCl_6. In Chapter 4 and Chapter 5, the chemisorbed Pt SSC (Pt-PANI) was prepared by the

impregnation between polyaniline and the H_2PtCl_6 ethanol solution. Specifically, polyaniline was dispersed in ethanol solution and ultrasonicated for 30 mins; then 10 mM H_2PtCl_6 dissolved in ethanol was dropwise into the polyaniline solution under vigorous stirring for 4 hrs. Finally, the mixed solution was centrifuged at 10,000 rpm for 10 mins (repeated three times) to get the dry powder products after evaporating the remaining ethanol solvent.

2.1.3 One-pot pyrolysis

As discussed in Chapter 1, one-pot pyrolysis is a synthesis strategy to prepare heterogeneous catalysts by pyrolysing metal precursors (like metal-organic frameworks (MOFs), metal phthalocyanine, metal–phenanthroline complexes) and supporting materials in tandem at desired temperatures. During the one-pot process, reactants can undergo successive chemical reactions in just one reactor. Therefore, the efficiency and chemical yield of one-pot pyrolysis are relatively high by avoiding a lengthy separation process and purification of the intermediate chemical compounds, which is adaptable for large-scale production of heterogeneous catalysts. And the one-pot pyrolysis typically cooperates with the wet impregnation method.

Specifically, the one-pot pyrolysis contains the following steps: (1) mixing metal precursors with impregnation materials to anchor metal sites on supporting materials (mixture of suspension); (2) centrifuging the obtained mixture with extra solvents, and drying to get a uniform powder; (3) finally, putting the as-prepared powder into a furnace and subsequently to anneal it in a selected temperature range and gas atmosphere. Fig. 2.2 below shows the typical procedure for the one-pot pyrolysis synthesis method.[5]

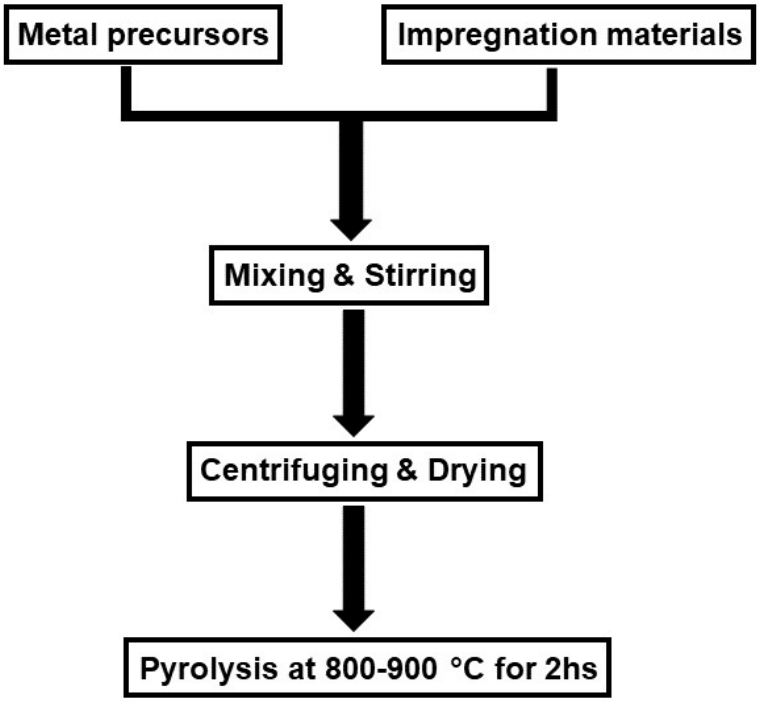


Figure 2.2: Synthesis steps of single-site electrocatalysts via a one-pot pyrolysis method.

Pt single-site heterogeneous catalysts are frequently prepared by the one-pot pyrolysis method.[6] In Chapter 4 and Chapter 5, polyaniline was first used to impregnate the Pt sites from H_2PtCl_6 dissolved in ethanol to form a Pt-PANI mixture. Then the obtained mixture suspension was stirred in ethanol for 4 hrs before centrifugation at 10,000 rpm for 30 mins and evaporation at 60 °C to remove the remaining solvent to get a dry powder Pt-PANI. Afterward, the Pt-PANI was put into a tube furnace, and its temperature was increased from RT to 800 °C at a rump rate of 15 °C/min. After reaching the setting temperature (800 °C), the Pt-PANI was annealed at 800 °C for 2 hrs to graphitise it completely. Finally, the furnace was naturally cooled down to obtain the final desired catalysts (trapped Pt SSC).

2.1.4 Casting catalysts on the glassy carbon electrode

There are two different types of Pt single-site catalysts cast on glassy carbon electrodes (1 cm by 2 cm, with a thickness of 1 mm) to test its catalytic performance for the HER: (1) thin-layer graphene nanosheets supported with Pt single-site complex; and (2) carbon-based powder materials supported with Pt single sites (Pt SSCs).

On the one hand, for the casting of Pt single-site complex catalysts supported on thin-layer graphene nanosheets, the CVD-grown graphene nanosheets (details described in section 2.1.1) are firstly transferred on glassy carbon with the polymer-assisted method without Cu residue (the graphene contacting with Cu side is stick with glassy carbon).[7] Then, the graphene surface is cleaned by annealing under Ar (70 sccm) / H_2 (5 sccm) flow at 250 °C for 2 hrs. The remaining sulfur from ammonium persulfate and small organics can be removed. Then Pt single-site complex catalyst is in-situ synthesised on the clean surface of graphene as described: 4 μL of aniline drop was cast on a 1 cm^2 graphene nanosheets transferred on the glassy carbon electrode, dried in ambient conditions for 15 mins, then 10 μL of 10 mM/L H_2PtCl_6 ethanol solution was dropped casting on the surface. The sample was then annealed in an argon atmosphere at 100 °C for 1.5 hrs. After the annealing treatment, the Pt sites from the H_2PtCl_6 precursor can be complexed with aniline molecules to in-situ form the Pt single-site structure on a glassy carbon electrode. Finally, the coated sample was sequentially washed with 0.5 M sulfuric acid, then deionised (DI) water, and dried under vacuum overnight.

For the Pt catalysts support on carbon-based powder substrates, typically, 20 wt% commercial Pt/C or carbon-based Pt SSC powders were mixed with ethanol and 5 wt% of Nafion (1 μL perfluorinated resin solution) and sonicated for at least 15 mins to obtain homogeneous inks. Then, the inks were stirred at a rate of 500 rpm for 2 hrs to make a well-dispersed catalyst suspension. Then 20 μL of the catalysts were dropped and coated on a glassy carbon electrode with an area of 1 cm^2 to get a catalyst loading of ~1 $\mu g_{Pt}\, cm^{-2}$ on each sample.

2.2 Materials characterisation techniques

The activity and stability of catalysts are closely related to their physical and chemical structures. Therefore, the routine ex-situ characterisation techniques can be divided into two parts: (1) scanning transmission electron microscopy (STEM) and X-ray diffraction pattern (XRD) for physical structure; (2) X-ray photoelectron spectroscopy (XPS), X-ray absorption spectroscopy (XAS), Raman spectroscopy, infrared spectroscopy, and nuclear magnetic

resonance (NMR) for chemical structure. Then, to clarify the structural evolution during synthesis and build real-time structure-activity relationships, in-situ heating STEM, in-situ XPS, and operando XAS are employed, respectively.

2.2.1 Scanning transmission electron microscopy

2.2.1.1 STEM

Scanning transmission electron microscopy (STEM) is a transmission electron microscopy equipped with additional scanning coils, detectors, and necessary circuitry. In the STEM mode, the microscope lenses are adjusted to create a convergent electron beam to focus on a fine spot. This focused probe is scanned across the sample surface, and various signals are collected point-by-point to form an image. The convergence of the beam destroys its coherency.

STEM is particularly suitable for analytical techniques such as Z-contrast annular dark-field imaging and spectroscopic mapping by energy dispersive X-ray (EDX) spectroscopy or electron energy loss spectroscopy (EELS). These signals can be obtained simultaneously, allowing direct correlation of microscopic and spectroscopic data (physical and chemical structures).

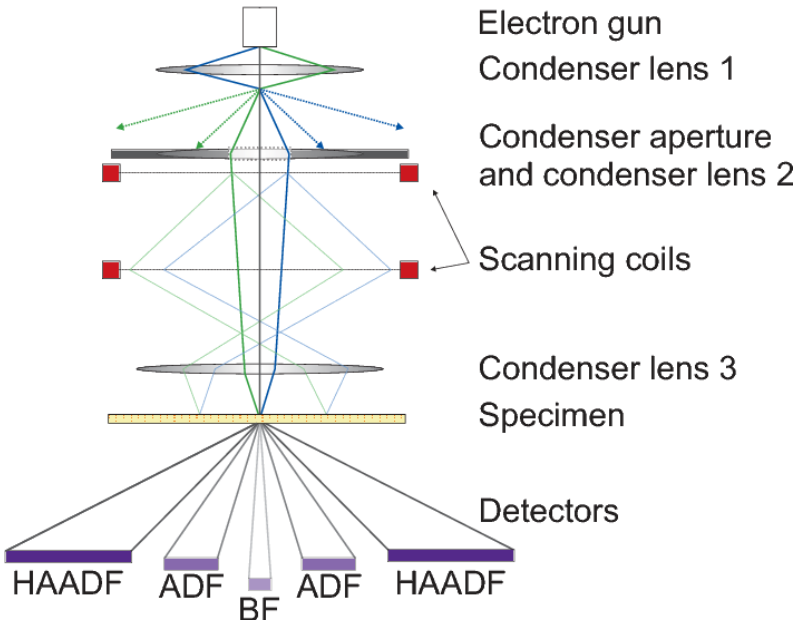


Figure 2.3.: Schematic of a typical STEM setup. Adapted from [8] with permission.

Atomic Z-contrast annual dark-field images are recorded during my projects. They are formed by mapping the intensity of high-angle scattered electrons as the electron probe is scanned across the specimen. Z-contrast images are incoherent, have doubled the resolution of coherent images, and do not reverse contrast with focus or specimen thickness. The images represent a direct map of the scattering power at atomic resolution. An incoherent image has no phase problem so that it can be directly inverted to the object. Because the image is formed from high-angle scattering from the atomic nuclei, the contrast of an atomic column is directly related to the atomic number (Z) squared.[9]

Adding an aberration corrector to STEMs enables the focused electron probes to go to a sub-angstrom diameter, allowing images with a sub-angstrom resolution to be acquired. Due to its atomic resolution to physical and chemical structures of materials, STEM has been widely used to characterise heterogeneous catalysts.[10]

The STEM used in my projects is a JEOL ARM-200F sited at David Cockayne Centre for Electron Microscopy. In Chapter 3 and Chapter 4, aberration-corrected STEM was employed under 80 kV/200 kV to get atomic high-angle annual dark field (HAADF) images of synthesised Pt structures. Dwell times of 10-20 μs, a beam current of 35 pA, and a pixel size of 0.006 nm px^{-1} were used for imaging, with a convergence semi-angle of 25.5 mrad and collecting inner-outer angles 68 to 275 mrad.

2.2.1.2 In-situ heating STEM

Differentially pumped sample chambers can be equipped with STEM to study the reactions of nanoparticles in gaseous environments at high temperatures. At the same time, a specialised holder is used to control the reaction temperature.[11]

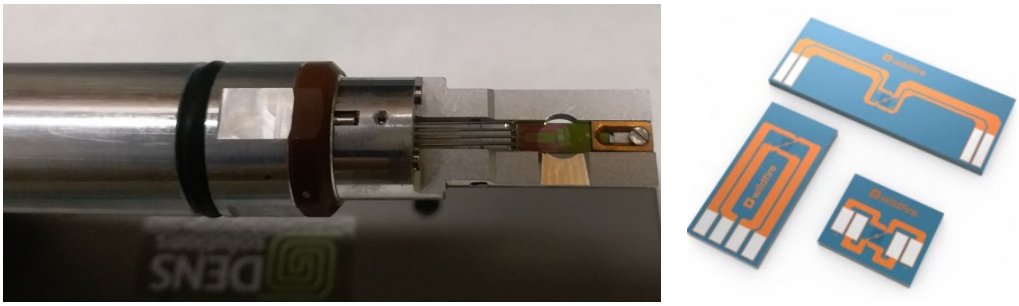


Figure 2.4: In-situ heating holder with software-controlled heating chips developed by Dens solution company.

In Chapter 5, in-situ STEM at heating was used under vacuum to investigate the structural evolution of Pt SSC on polyaniline with rising temperatures (Fig. 2.4).

2.2.2 X-ray photoelectron spectroscopy

X-ray photoelectron spectroscopy (XPS) is a highly surface-sensitive and quantitative chemical analysis technique that can measure the elemental composition and determine the chemical states of the elements at the surface of a wide range of materials (1-10 nm).

This technique uses a beam (usually X-rays) to irradiate a sample. Photoelectrons will be ejected from the surface of the sample after the core electrons of the atoms presenting at the sample surface absorb this irradiation energy. The kinetic energy (KE) of the emitted photoelectrons can be measured by an energy analyser. Combined with the energy of the incident beam (E_{beam}), the kinetic energy can be used to calculate the photoelectrons' binding energy (E_b), which is characteristic of the element and its chemical state:

$$E_b = E_{beam} - KE - \varphi \qquad (2.1)$$

Where φ is the work function that is specific to the spectrometer.

Normally, photoelectrons generated near the surface, which escape without losing too much energy, can be detected. This means that XPS can be used to measure materials at the top few nanometres of the surface. The surface selectivity, coupled with quantitative chemical state identification, makes XPS valuable for characterizing nano-structured heterogeneous catalysts.

The ex-situ XPS experiments were done on the Pt reference samples, Pt/Aniline/Ar, and Pt/Ar samples in Chapter 3, and Pt-PANI in Chapter 4, using a PHI VersaProbe III system generating monochromatic Al X-rays at 1486 eV. The core levels of Pt 4f, N 1s, Cl 2p, and C 1s were measured at a pass energy of 26 eV, giving an energy resolution of 0.45 eV. The binding energies of the spectra were calibrated on the C-C sp^3 bond from carbon black, which is located at 284.8 eV in the C 1s spectra. The CasaXPS was used to analyse the spectra. The fitting was operated using a Shirley background and a Gaussian-Lorentzian peak shape GL(30). The ex-situ XPS experiments in Chapter 3 and Chapter 4 were performed by a postdoc in the group, Dr. Sudarshan Narayanan (University of Oxford).

For the in-situ XPS in Chapter 5, survey measurements were performed at a pass energy of 224 eV. In comparison, core levels were measured at a pass energy of 13 eV (26 eV), giving an energy resolution of 0.4 eV (0.45 eV). Samples were deposited directly onto gold foil for XPS measurements which negated the need for any charge compensation mechanisms. Samples were transferred into a prep-chamber without breaking the vacuum to be heated. Subsequently, samples were moved back into the XPS system through a load lock. In-situ heating was performed using a ceramic heater from Thermic Edge, capable of reaching 1600 °C in UHV. A type K thermocouple was used to contact the Mo sample plate during heating to allow temperature measurements. The in-situ XPS experiment on the Pt-PANI was performed by a collaborator, Dr. Jack E. N. Swallow (University of Oxford).

2.2.3 X-ray absorption spectroscopy

2.2.3.1 Ex-situ XAS

X-ray absorption spectroscopy (XAS) is widely used to determine the materials' local geometric and electronic structure.[12] A synchrotron radiation-based X-ray is applied as a function of incrementing energy in small energy steps close to the absorption edge. The transmission (or fluorescence) of X-rays is measured for analysis.

The absorption edge energy corresponds to the energy required to eject an electron from an electron shell of a target element. Small changes in how x-rays are absorbed near and above an atom's absorption edge provide insight into the state of the electrons.[13] It can reflect the average oxidation state and bonding environment of the detected elements in the whole sample, which is complementary to atomic STEM images. XAS is very sensitive to the local atomic coordination of low concentration samples. It is a powerful technique for characterising heterogeneous single-site catalysts.

XAS is comprised of two regions as follows:

X-ray absorption near edge structure (XANES/NEXAFS): Comprising X-ray energies nearest to the absorption edge (10~150 eV around the edge), this region is dominated by core transitions to quasi-bound states, which exhibit sharp resonance peaks. Generally, the region is sensitive to local atomic states, such as oxidation states and symmetry.

Extended X-ray absorption fine structure (EXAFS): This region contains features appearing after the XANES (150 eV) region and up to ~1000 eV greater than the absorption edge. EXAFS appears as gentle oscillations in the measured signal and is caused by the scattering of the ejected electron by surrounding atoms. It can measure neighbouring atom information, including bond lengths and chemical coordination environments.

In Chapter 3 and Chapter 4, the ex-situ XAS measurements at the Pt L_3-edge were carried out at the B18 Core EXAFS beamline of Diamond Light Source. The Pt reference samples (300 mg) and synthesised Pt SSC were finely ground, mixed homogeneously with five parts of cellulose, and pressed into 13 mm diameter pellets. All spectra were recorded in transmission mode at RT. The ex-situ XAS experiments were conducted by a collaborator, Dr. Diego Gianolio (Diamond Light Source).

2.2.3.2 In-situ XAS with HER

To clarify the structural evolution of prepared Pt SSCs for HER working conditions, the in-situ XAS spectra are recorded when chronoamperometry is applied at varied potentials in Chapter 3 and Chapter 5.

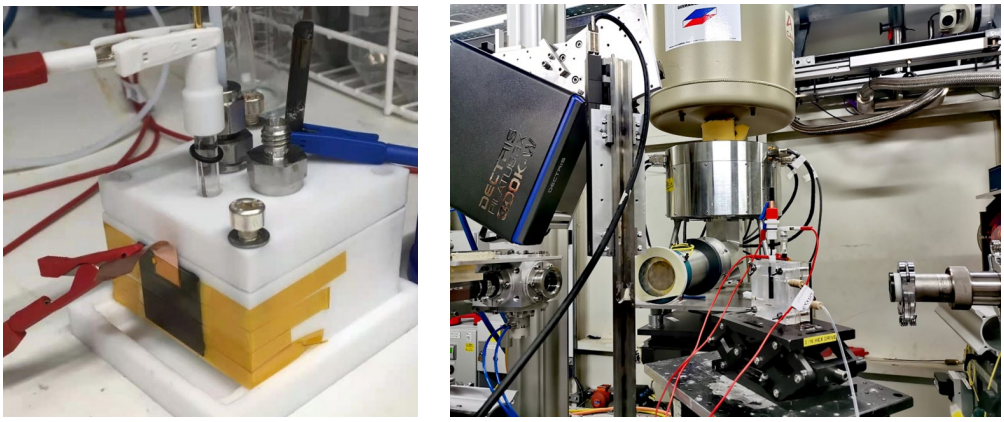


Figure 2.5: In-situ cells were used for the XAS study in Chapter 3 (left) and Chapter 5 (right).

The XAS experiments were performed at the B18 Core EXAFS beamline of the Diamond Light Source. The measurements were carried out using the Cr-coated branch of collimating and focusing mirrors and a Si(111) double-crystal monochromator. The size of the beam at the sample position was ca. 1 mm (*h*)×1mm (*v*). Samples were measured both in static electrolyte and operando conditions. The data were collected in fluorescence mode using a 36-element solid-state germanium detector; the ion chamber at the front of the sample was used to measure incoming photons (I_0 filled with a mixture of 80 mbar of Ar and 1020 mbar of He to optimize sensitivity at 15% efficiency). Electrochemical cells adapted to the B18 beamline of the UK's Synchrotron Diamond Light Source were designed for the operando study shown in Fig. 2.5. Before the operando electrochemical measurements, the Pt L_3-edge spectra were measured in contact with the liquid electrolyte. The operando XAFS spectra of the Pt L_3-edge (11564 eV) were obtained from 200 eV before the edge up to 750 eV after the edge (corresponding to 14 $Å^{-1}$ in k-space). The measuring time was 2 mins per spectrum. When indicated, 8/6 repetitions at each potential were acquired and merged to obtain a better signal-to-noise ratio. Data were normalised using the Athena program with a linear pre-edge and polynomial post-edge background subtracted from the raw data. EXAFS fits were performed

using ARTEMIS software.[14] The in-situ XAS experiments were conducted by a collaborator, Dr. Diego Gianolio (Diamond Light Source).

2.2.4 Raman spectroscopy

Raman spectroscopy is a non-destructive spectroscopic analysis technique to determine vibrational models of molecules based on the interaction of light with the chemical bonds within materials. It provides fingerprints about chemical structure, phase and polymorphy, crystallinity, and molecular interactions.

Raman is a light scattering technique whereby a molecule scatters incident light from a high-intensity laser light source. Two leading scattered lights will be generated after the interaction:

Rayleigh scattering: the elastically scattered light at the same wavelength as the laser source, which does not provide characteristic information of target materials;

Raman scattering: a form of inelastic light scattering in which a photon excites the sample at different wavelengths. This small amount of scattered light (typically 0.0000001%) provides the chemical structure of the analyte.

Raman scattering relies upon the inelastic scattering of photons. Typically, a sample is illuminated with a laser beam in the visible, near-infrared, or near ultraviolet range. The laser beam interacts with molecular vibrations, phonons, or other excitations in the system, resulting in the energy of the laser photons being shifted up or down. Electromagnetic radiation from the illuminated spot is collected with a lens and sent through a monochromator. Elastically scattered radiation at the wavelength corresponding to the laser line (Rayleigh scattering) is filtered out by a notch filter. In contrast, the rest of the collected light (Raman scattering) is dispersed onto a detector. The detector can collect the shift in the energy of excited photons, which gives information about the vibrational modes in the sample.

The magnitude of the Raman effect correlates with the polarisability of the electrons in a molecule. It is a form of inelastic light scattering, where a photon excites the sample. This

excitation puts the molecule into a virtual energy state for a short time before the photon is emitted. Inelastic scattering means that the energy of the emitted photon is either lower or higher than the incident photon. After the scattering event, the sample is in a different rotational or vibrational state.

For the total energy of the system to remain constant after the molecule moves to a new rovibronic (rotational-vibrational-electronic) state, the scattered photon shifts to different energy and, therefore, a different frequency. This energy difference is equal to that between the initial and final rovibronic states of the molecule. If the final state is higher in energy than the initial state, the scattered photon will be shifted to a lower frequency (lower energy) so that the total energy remains the same. This frequency shift is called a Stokes shift or downshift. If the final state is lower in energy, the scattered photon will be shifted to a higher frequency, called an anti-Stokes shift, or upshift.

For a molecule to exhibit a Raman effect, there must be a change in its electric dipole-electric dipole polarisability concerning the vibrational coordinate corresponding to the rovibronic state. The intensity of the Raman scattering is proportional to this polarisability change. Therefore, the Raman spectrum (scattering intensity as a function of the frequency shifts) depends on the rovibronic states of the molecule.

The instrument used in this work is a Renishaw InVia microscope. It was used to characterise in-situ impregnated Pt single-site complex on graphene nanosheets in Chapter 3 and to clarify polyaniline substrate before and after pyrolysis in Chapter 5. A 785 nm laser was used. Multiple acquisitions were made with a 1% laser intensity for 1 s exposure time.

2.2.5 Infrared spectroscopy

Infrared spectroscopy (IR spectroscopy or vibrational spectroscopy) measures the interaction of infrared radiation with materials by absorption, emission, or reflection. It is used to study and identify chemical bonds (functional groups) in solid, liquid, or gaseous forms. The method or technique of infrared spectroscopy is conducted with an instrument called an infrared

spectrometer (or spectrophotometer) which produces an infrared spectrum. The infrared spectrum of a sample is recorded by passing a beam of infrared light through the sample. When the frequency of the IR is the same as the vibrational frequency of a bond or collection of bonds, absorption occurs. The fundamental mechanism of this absorption is that infrared radiation can excite the mode of molecules, from a ground state with vibrational quantum number v = 0 to the first excited state with vibrational quantum number v = 1. And then, by examination of the transmitted light, how much energy is absorbed in each frequency (or wavelength) can be revealed.

The characteristic wavelength is commonly used for analysing samples with covalent bonds. Therefore, an IR spectrum can be visualised in a graph of infrared light absorbance (or transmittance) on the vertical axis vs. wavelength on the horizontal axis. Typical units of wavenumber used in IR spectra are reciprocal centimetres, with the symbol cm^{-1}.

The infrared spectrum measurement can be achieved by scanning the wavelength range using a monochromator. Alternatively, the entire wavelength range is usually necessary to identify chemical bonds in a sample. Hence, the IR spectrum measured using a Fourier transform instrument to generate a transmittance or absorbance spectrum is a more practical technique.

Fourier-transformed infrared (FTIR) spectroscopy is a measurement technique that allows one to record infrared spectra. Infrared light is guided through an interferometer and the sample (or vice versa). A moving mirror inside the apparatus alters the infrared light distribution that passes through the interferometer. The signal directly recorded, called an "interferogram", represents light output as a function of mirror position. A data-processing technique called Fourier transform turns this raw data into the sample's spectrum: light output as a function of infrared wavelength (or wavenumber). As described above, the sample's spectrum always needs to be compared to a reference.

In Chapter 4, FTIR spectroscopy is used to characterise the chemical bonds of synthesised polyaniline (PANI) substrate (powder). And then, the interaction between anchored Pt single

sites and the polyaniline substrate is also identified by FTIR. Finally, in Chapter 5, the transformation of chemical bonds in Pt-PANI after being heated at different temperatures is recorded by FTIR spectra.

2.2.6 X-ray diffraction pattern

X-ray Diffraction (XRD) is a common technique for studying crystal structures and atom spacings of materials. This method uses coherent X-Ray radiation collimated and directed to the sample.

Firstly, X-rays are generated in a cathode ray tube by heating a filament to produce electrons, accelerating and bombarding the electrons toward target materials to produce their characteristic X-ray spectra. After filtering with crystal monochromators, monochromatic X-rays needed for diffraction can be generated. Copper is the most common target material for single-crystal diffraction, with Cu K_α radiation = 1.5418Å.

Then, the generated X-ray radiation is directed to interact with the atoms in the crystal structure of a sample. As the sample and detector are rotated, the intensity of the reflected X-rays is recorded. A clear peak in intensity occurs when the radiation waves interfere with crystal atoms constructively and satisfy Bragg's law:

$$n\lambda = 2d\sin(\theta) \tag{2.2}$$

Where n is an integer number (generally 1), λ is the wavelength of the radiation, d is the distance between two crystallographic planes, and θ is the glancing angle between the radiation and the crystallographic plane. By varying the glancing angle, we obtain a diffractogram that reports the intensity of the diffracted radiation with respect to the angle (reported as 2θ). Peaks are located where Bragg's relation is satisfied, confirming the existence of crystallographic planes separated by d. Therefore, it is possible to identify crystalline phases present in a sample based on the diffracted radiation.

The instrument used in this work is a Rigaku Smartlab X-Ray diffractometer with a Cu $K_{\alpha 1}$ radiation and a 3 kW rotating anode X-Ray generator. Patterns were collected from 5° to 90° (2θ), at a scan rate of 5° min^{-1}. In Chapter 3, XRD was used to characterise the in-situ prepared Pt single-site complex on glassy carbon (Pt/Ani/graphene) to check for the absence of Pt nanoparticles.

2.2.7 Nuclear magnetic resonance

Nuclear magnetic resonance (NMR) is a physical phenomenon in which nuclei will be perturbed in a solid, constant oscillating magnet and respond by producing an electromagnetic signal with a frequency characteristic of the magnetic field at the nucleus.[15] This process occurs when the oscillation frequency matches the intrinsic frequency of the nuclei, which can be regarded as the resonance between nuclei and the magnetic field. The characteristic frequency is determined by the strength of the static magnetic field, the chemical environment of nuclei, and the magnetic properties of the isotope involved.

NMR spectroscopy determines the chemical structure, chemical environment, and dynamics of molecules and materials in liquid or solid phases. NMR is the oscillatory response of nuclei with non-zero spins in a magnetic field to resonant excitation by radiofrequency irradiation. When atoms containing non-zero nuclear spins are placed in an external magnetic field, the degeneracy of the nuclear spin states is lifted, and an excitation of nuclei in the lower energy state to the higher energy state, leading to an energy difference ΔE given by equation (2.3):

$$\Delta E = \Upsilon \hbar \, (1 - \sigma) \, B_0 \qquad (2.3)$$

Where γ is the gyromagnetic ratio, a fundamental property associated with each isotope; B_0 is the strength of the static magnetic field, and σ is the chemical shielding around a nucleus. Transitions can then be induced by electromagnetic radiation between these nuclear spin states. The NMR transition frequencies are sensitive to the electron distribution around the nucleus, which shields the nucleus from the applied magnetic field. The shielding constant, σ, varies for different nuclei of a given isotope in a molecule, causing slightly different

frequencies.[16] Thus, NMR frequencies can reveal the sample'. NMR frequencies are commonly reported as a chemical shift, δ, which is the fractional difference between the frequency of a particular nucleus and a standard compound such as tetramethylsilane.

Solid-state NMR spectroscopy is the application of NMR spectroscopy to solid samples, including powders, single crystals, and amorphous samples and tissues in chemistry and materials sciences. In solids, the orientation dependence of NMR frequencies causes powder patterns for each nuclear spin. In most cases, this anisotropic contribution needs to be removed to obtain site-resolved spectra combined with magic-angle spinning (MAS), where samples are physically spun around an axis tilted by 54.7° from the static magnetic field. This angle results from the anisotropy of NMR interactions given by a second-rank tensor, whose time average vanishes at 54.7°.[17] MAS averages out the information-rich anisotropic chemical shift and dipolar interactions; many radiofrequency pulse sequences have been designed to reintroduce the desired spin interactions while retaining spectral resolution selectively.

In Chapter 5, solid-state NMR spectra are recorded to identify the structure of Pt single sites anchored on PANI (Pt-PANI) and the 1 wt% Pt-PANI sample after annealing at 800 °C under an N_2 atmosphere. Specifically, all solid-state NMR experiments were performed on a 9.45 T Bruker Avance III HD NMR spectrometer, operating at ^{1}H and ^{15}N Larmor frequencies of 399.89 and 40.52 MHz, respectively. A Bruker 4 mm double-resonance magic angle spinning (MAS) probe was used to facilitate a spinning frequency of 12 kHz. Those NMR experiments were performed and analysed by Dr. Hua Guo (University of Oxford) in the group.

2.3 Electrochemical characterisation techniques

2.3.1 Linear sweep voltammetry

Linear sweep voltammetry (LSV) is a voltammetric method to measure the current at a working electrode while the potential between the working electrode and a reference electrode is swept

linearly from the lower potential limit to the upper potential limit in time.[18] The experimental setup for linear sweep voltammetry utilises a potentiostat and a three-electrode system, including a working electrode, reference electrode, and counter electrode. The three electrodes are connected to a potentiostat and are placed in an electrochemical cell with the solution of interest. The potentiostat delivers a potential, E (a potential between the working electrode and reference electrode), through the working electrode to a solution. Then the current at the working electrode is monitored. Therefore, a plot of potential vs. current can be made, showing the oxidation and reduction of the material in the investigation. The slope of the potential vs. time graph is called the scan rate and can range from mV/s to 1,000,000 V/s.[19]

The working electrode is one of the electrodes at which the oxidation/reduction reactions occur—the processes at this electrode are monitored. The counter electrode is where an opposite process from the one taking place at the working electrode occurs. The processes at the counter electrode are not monitored. As the reactant molecules on the surface of the working electrode are oxidized/reduced, they move away from the surface, and new molecules come into contact with the surface of the working electrode. There will be electrons given out at the surface of the working electrode during the oxidation/reduction of molecules. The flow of electrons into or out of the electrode causes the current. The current is a direct measure of the rate at which electrons are exchanged through the electrode-electrolyte interface. When this rate becomes higher than the rate at which the oxidizing or reducing species can diffuse from the bulk of the electrolyte to the surface of the electrode, the current reaches a plateau or exhibits a peak.[20]

In Chapter 4 and Chapter 5, LSV experiments are employed to investigate the HER activity of target catalysts. A three-electrode cell system with coated catalysts on glassy carbon as the working electrode, Hg/Hg_2SO_4 as the reference electrode, and graphitic rod/Pt mesh as the counter electrode are used. The electrolyte is 0.5 M H_2SO_4 diluted from pure H_2SO_4 with DI water (18.2 Ω/cm). The obtained LSV curves can calculate the onset potential (overpotential

needed to reach a current density of 1 mA cm^{-2}), exchange current density, and Tafel slope value at an area without mass transform limit.

2.3.2 Cyclic voltammetry

Cyclic voltammetry (CV) is a type of potentiodynamic electrochemical measurement. In a cyclic voltammetry experiment, the working electrode potential is ramped linearly versus time. Unlike in linear sweep voltammetry, after the set potential is reached in a CV experiment, the working electrode's potential is ramped in the opposite direction to return to the initial potential. These cycles of ramps in potential are repeatable as needed. The rate of voltage change over time during each cyclic phase is known as the experiment's scan rate (mV/s). The applied potential is measured between the working electrode and the reference electrode, while the current is measured between the working electrode and the counter electrode. And the CV plot is defined as the recorded current at the working electrode versus the applied working electrode's potential.

The CV cycles work as follows: during the initial forward scan (from t_0 to t_1), an increasingly reducing potential is applied; thus, the cathodic current will, at least initially, increase over this period, assuming that there are sufficient reducible analytes in the system. After the reduction potential of the analyte is reached, the cathodic current will decrease as the concentration of the reducible analyte is depleted. If the redox couple is reversible, then during the reverse scan (from t_1 to t_2), the reduced analyte will start to be re-oxidised, giving rise to a reverse polarity current (anodic current) to before. The similarity between the oxidation and reduction peaks corresponds to the reversibility of the redox couple of analytes. Hence, CV data can provide information about redox potentials and electrochemical reaction rates.

This work uses a Bio-logic VMP3 or SP-150/240 to perform three-electrodes cell experiments. In Chapter 5, CV experiments are employed on a three-electrode cell system with Pt foil/coated catalysts on glassy carbon as the working electrode, Hg/Hg_2SO_4 as the reference electrode, and graphitic rod/Pt mesh as the counter electrode. 50-100 CV cycles with a scan

rate of 20 mV/s are used to clean the surface of active materials and reach stable and repeatable CV curves. It can be used to calculate the electrochemical surface areas of Pt foil catalysts. The electrolyte is 0.5 M H_2SO_4 diluted from pure H_2SO_4 with DI water (18.2 Ω/cm).

2.3.3 Chronoamperometry

Chronoamperometry (CA) is used to study the kinetics of chemical reactions, diffusion processes, and adsorption. In this technique, a constant potential step is applied to the working electrode, and the resulting current at the electrode is monitored as a function of time. The physical electrochemistry chronoamperometry experiment supports both single- and double-potential step experiments.

After the application of potential, the analyte in one oxidation state will be oxidised or reduced to another oxidation state. As the analyte is consumed, the current will decrease to the baseline (approaching zero). The total charge (in coulomb) that flows in the reaction during this process can also be calculated by integrating the area under the current plot and applying Faraday's law. The cell for CA electrolysis is usually a two- or three-compartment cell containing a counter electrode and is separated from the working electrode.

Specifically, in an unstirred cell, in response to a potential step perturbation, electrochemically active species in the electrolyte will diffuse to the surface of the working electrode as a function of the potential applied. At the onset of a potential step, a large current from ion flux to the electrode surface to balance the change in potential gives rise to a capacitive current, which decays rapidly. The concentration of electrochemically active species near the electrode surface decays with distance from the electrode, and the arrival of species to the surface is diffusion limited; therefore, as the mass transport limit is reached near the electrode surface, the Faradaic current will decay over time. These currents provide a typical exponential decay curve described by the Cottrell equation.[21]

CA electrolysis is generally utilised with cyclic voltammetry. Cyclic voltammetry can analyse the electrochemical behaviour of the analyte or the reaction. For instance, cyclic voltammetry

could tell us the cathodic potential of an analyte. Since the cathodic potential of this analyte is obtained, CA electrolysis could hold this constant potential for the reaction to happen.[22]

In Chapter 3 and Chapter 5, the CA tests are employed at a three-electrode cell during the operando XAS experiments to detect how current changes with the applied potentials at working electrodes. The working electrode was made by casting synthesised Pt SSC catalysts on glassy carbon, as described in Section 3.1.4. Then, based on obtained results, structure-activity relationships were built to clarify the undermining catalytic mechanism.

2.3.4 Potentiostatic electrochemical impedance spectroscopy

Potentiostatic Electrochemical Impedance Spectroscopy (PEIS) is a powerful technique that utilises a small amplitude, alternating current (AC) signal to probe the impedance characteristics of a cell. Like resistance (defined by Ohm's law), impedance is a measure of the ability of a circuit to resist the flow of electrical current.

Electrochemical impedance is usually measured by applying an AC potential to an electrochemical cell and then measuring the current through the cell. Assume that a sinusoidal potential excitation is applied. The response to this potential is an AC current signal. This current signal can be analysed as a sum of sinusoidal functions (a Fourier series). The impedance is the ratio between the AC potential and AC current signal. Therefore, it can be described by using the following equations.[23]

$$E_t = E_0 \sin(\omega t) \tag{2.4}$$

Where I_t is the potential at the time t, E_0 is the amplitude of the signal, and ω is the radial frequency. The relationship between radial frequency ω (expressed in radians/second) and frequency f (expressed in hertz) is:

$$\omega = 2\,\pi\,f \tag{2.5}$$

In a linear system, the response signal, I_t, is shifted in phase (Φ) and has a different amplitude than I_0.

$$I_t = I_0 \sin\ (\omega t + \phi) \tag{2.6}$$

An expression analogous to Ohm's Law allows us to calculate the impedance of the system as:

$$Z = \frac{E_t}{I_t} = \frac{E_0 \sin(\omega t)}{I_0 \sin(\omega t + \phi)} = Z_0 \frac{\sin\ (\omega t)}{\sin(\omega t + \phi)} \tag{2.7}$$

The impedance is therefore expressed in terms of a magnitude, Z_0, and a phase shift, Φ. If Euler's relationship is used to exchange, it is possible to express the impedance as a complex function. The potential is described as follows,

$$E_t = E_0 \exp(j\omega t) \tag{2.8}$$

and the current response as,

$$I_t = I_0 \exp(j\omega t - \phi) \tag{2.9}$$

The impedance is then represented as a complex number,

$$Z(\omega) = \frac{E}{I} = Z_0 \exp(j\phi) = Z_0\ (cos\phi + jsin\phi) \tag{2.10}$$

The impedance analysis shown in Chapter 5 was performed under a three-electrode cell by glassy carbon coated with commercial Pt/C or trapped Pt SSC as a working electrode, Pt mesh as a counter electrode, and a standard Hg/Hg_2SO_4 as a reference electrode. The range of frequencies used in the experiment was 200 kHz - 1Hz. The impedance was performed before the CV cycles, allowing at least half an hour of relaxation time to equilibrate the system.

2.4 References

1. Sheng, Y., Rong, Y., He, Z., Fan, Y. & Warner, J. H. Uniformity of large-area bilayer graphene grown by chemical vapor deposition. *Nanotechnology* **26**, 395601 (2015).

2. Munnik, P., de Jongh, P. E. & de Jong, K. P. Recent Developments in the Synthesis of Supported Catalysts. *Chem Rev* **115**, 6687–6718 (2015).

3. Haukka, S., Lakomaa, E. L. & Suntola, T. Adsorption controlled preparation of heterogeneous catalysts. *Stud Surf Sci Catal* **120**, 715–750 (1999).

4. Zhang, C., Oliaee, S. N., Hwang, S. Y., Kong, X. & Peng, Z. A Generic Wet Impregnation Method for Preparing Substrate-Supported Platinum Group Metal and Alloy Nanoparticles with Controlled Particle Morphology. *Nano Lett* **16**, 164–169 (2016).

5. Zhao, S. et al. One-Pot Pyrolysis Method to Fabricate Carbon Nanotube Supported Ni Single-Atom Catalysts with Ultrahigh Loading. *ACS Appl Energy Mater* **1**, 5286–5297 (2018).

6. Zhu, Y. *et al*. One-Pot Pyrolysis to N-Doped Graphene with High-Density Pt Single Atomic Sites as Heterogeneous Catalyst for Alkene Hydrosilylation. *ACS Catal* **8**, 10004–10011 (2018).

7. Fan, Y., He, K., Tan, H., Speller, S. & Warner, J. H. Crack-free growth and transfer of continuous monolayer graphene grown on melted copper. *Chemistry of Materials* **26**, 4984–4991 (2014).

8. Keller D R. Role of Nanoscale Inhomogeneities in Cu (In, Ga) Se_2 Thin Film Solar Cells. ETH Zurich, (2016).

9. Pennycook, S. J. & Jesson, D. E. High-resolution Z-contrast imaging of crystals. *Ultramicroscopy* **37**, 14–38 (1991).

10. Jones, L., Macarthur, K. E., Fauske, V. T., van Helvoort, A. T. J. & Nellist, P. D. Rapid estimation of catalyst nanoparticle morphology and atomic-coordination by high-resolution Z-contrast electron microscopy. *Nano Lett* **14**, 6336–6341 (2014).

11. Boyes, E. D., Ward, M. R., Lari, L. & Gai, P. L. ESTEM imaging of single atoms under controlled temperature and gas environment conditions in catalyst reaction studies. *Ann Phys* **525**, 423–429 (2013).

12. Evans, J. X-Ray Absorption Spectroscopy for the Chemical and Materials Sciences. *X-Ray Absorption Spectroscopy for the Chemical and Materials Sciences* (2018) doi:10.1002/9781118676165.

13. Newville, M. Fundamentals of XAFS. *Rev Mineral Geochem* **78**, 33–74 (2014).

14. Ravel, B. & Newville, M. ATHENA, ARTEMIS, HEPHAESTUS: data analysis for X-ray absorption spectroscopy using IFEFFIT. *urn:issn:0909-0495* **12**, 537–541 (2005).

15. Levitt, M. H. Spin dynamics : basics of nuclear magnetic resonance. 714 (2008).

16. Reif, B., Ashbrook, S. E., Emsley, L. & Hong, M. Solid-state NMR spectroscopy. *Nature Reviews Methods Primers 2021 1:1* **1**, 1–23 (2021).

17. Schaefer, J. & Stejskal, E. O. Carbon-13 Nuclear Magnetic Resonance of Polymers Spinning at the Magic Angle. *J Am Chem Soc* **98**, 1031–1032 (1976).

18. Nahir, T. M., Clark, R. A. & Bowden, E. F. Linear-Sweep Voltammetry of Irreversible Electron Transfer in Surface-Confined Species Using the Marcus Theory. *Anal Chem* **66**, 2595–2598 (1994).

19. Imbeaux J C, Savéant J M. Convolutive potential sweep voltammetry: I. Introduction. *Journal of Electroanalytical Chemistry and Interfacial Electrochemistry*, 44(2): 169-187 (1973).

20. Nahir, T. M., Clark, R. A. & Bowden, E. F. Linear-Sweep Voltammetry of Irreversible Electron Transfer in Surface-Confined Species Using the Marcus Theory. *Anal Chem* **66**, 2595–2598 (2002).

21. Cottrell, F. G. Der Reststrom bei galvanischer Polarisation, betrachtet als ein Diffusionsproblem. Zeitschrift für Physikalische Chemie 42U, 385–431 (1903).

22. Vieira, K. L. & Peters, D. G. Voltammetric behavior of tertiary butyl bromide at mercury electrodes in dimethylformamide. *J Electroanal Chem Interfacial Electrochem* **196**, 93–104 (1985).

23. Instruments, Gamry. Basics of EIS: Electrochemical Research-Impedance. (2016).

Chapter 3

Physically adsorbed Pt SSC

3.1 Introduction

Catalysts for the electrochemical hydrogen evolution reaction (HER) are desirable to produce hydrogen from clean sources like solar energy.[1, 2] Platinum is among the most active HER catalysts known in acidic media.[3] Platinum is a heterogeneous catalyst, with the HER occurring only on the metal surface.[4] This can be prohibitively inefficient because platinum is so rare and expensive.[5]

Single-site catalysts (SSCs) are an emerging type of heterogeneous catalysts in which isolated metal sites are supported on suitable substrates.[6, 7] Each metal site is well separated from other metal atoms by a distance greater than the length of the metallic chemical bond.[8, 9] Platinum SSCs can be prepared by synthesising a platinum complex and adsorbing the whole complex to a suitable substrate.[10-12] They have extremely high atom utilisation because every catalytic atom is exposed to the reactants and available for reaction.[13, 14] We choose to distinguish these structures from single-atom catalysts (SACs),[15-17] which have also been shown to promote a broad range of catalytic reactions, since the Pt SSCs we investigate are complexes of several atoms surrounding the catalytically active metal atom.[18, 19]

Despite the promise of platinum SSCs for the HER, the bonding environment of platinum in these devices before and during operation is poorly understood.[20-23] Establishing the structure-property relationship between the platinum bonding and the electrochemical performance of the catalyst is critically important to enabling the design of tailored, high per-

forming platinum SSCs.[24, 25] Furthermore, platinum SSCs for the HER have poor long-term stability, but the cause of their degradation is poorly understood.[26] Operando spectroscopy methods are a powerful tool to determine at the molecular level why these catalysts deactivate over time.[27-30]

In this work, we examine the model SSC system of a platinum complex with aniline and chloride ligands (trans-dianilinedichloroplatinum(II)) physically adsorbed onto graphene. Graphene is an excellent substrate because of its high electronic conductivity, chemical stability,[31] and the good contrast it provides with platinum in electron microscopy.[32] At the same time, aniline is stabilised via adsorption onto graphene through pi-pi stacking interactions with the molecule's aromatic ring.[10] Furthermore, aniline readily complexes with platinum and the molecule's large size provides a steric hindrance that can prevent platinum agglomeration.[33, 34]

We characterise the physical structure of the as-synthesised SSC with ex-situ scanning transmission electron microscopy (STEM) and X-ray diffractometry (XRD). We examine the SSC's oxidation state and bonding environment with X-ray photoelectron spectroscopy (XPS), X-ray absorption near edge structure spectroscopy (XANES), and extended X-ray absorption fine structure spectroscopy (EXAFS). Finally, we use chronoamperometry with operando EXAFS and XANES, fitted with structures calculated using density-functional theory (DFT), to study how platinum's bonding environment and coordination number change as a function of applied potential during the HER. This work is a good demonstration of using operando X-ray spectroscopy techniques to probe the atomic-level structural evolution of platinum SSCs for the HER during operation. This is an important contribution to the understanding of the synthesis and stability of platinum SSCs.

3.2 Results and discussion

3.2.1 Synthesis and physiochemical characterisation

The platinum SSC is prepared according to a modified impregnation method described in detail in Chapter 2 and outlined in Fig. 3.1a.

High-angle annular dark-field scanning transmission electron microscopy (HAADF-STEM) of (Pt/Ani/Ar) and (Pt/Ar) are shown in Fig. 3.1c-d and e-f, respectively. (Pt/Ani/Ar) contains atomically dispersed platinum with an average areal number density of about 0.5 nm^{-2}. Some aggregates of platinum are present;[34] these are generally of size 1 nm or smaller (Fig. 3.2a). (Pt/Ar) mainly contains larger nanoparticles that are up to about 4 nm across (Fig. 3.2b).

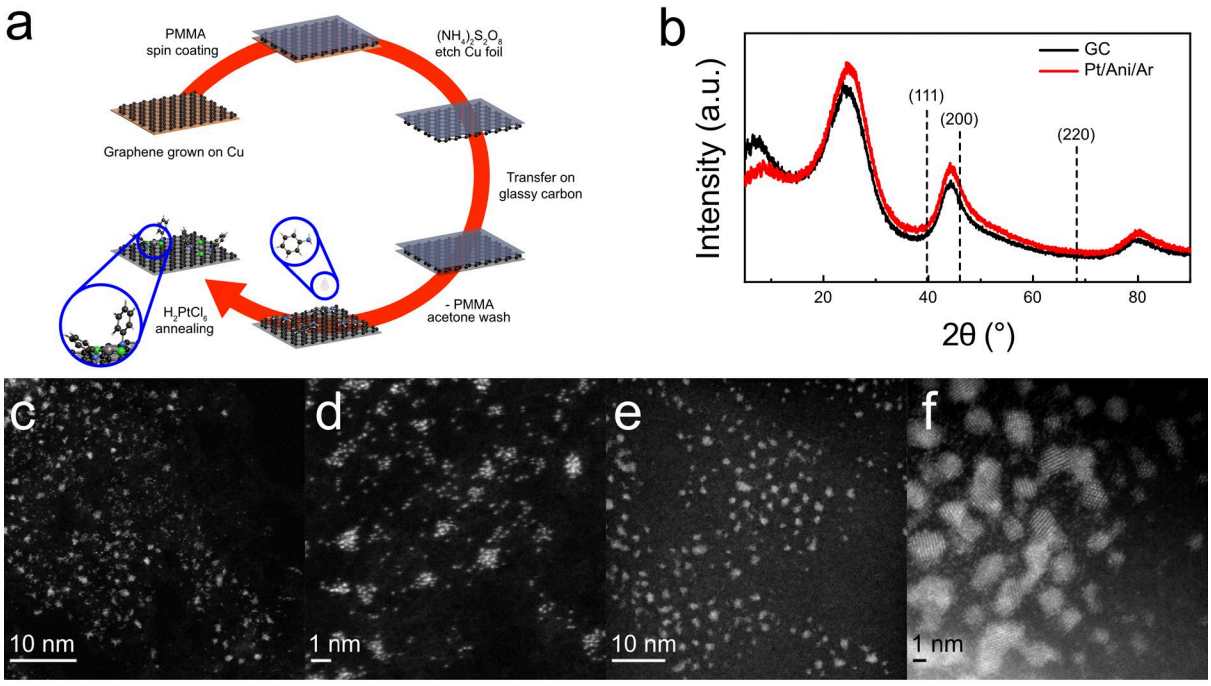


Figure 3.1: a, Schematic illustration of the synthesis process (5 steps) for Pt SSC (grey, Pt; green, Cl; blue, N; black, carbon; white, H). Step 1: graphene nanosheets are grown by chemical vapour deposition (CVD) on copper; Step 2: copper foil is etched after spin-coating with polymethyl methacrylate (PMMA) on top; Step 3: thin-layer graphene coated with PMMA is then transferred onto a polished glassy carbon (GC) electrode; Step 4: after washing the PMMA with acetone and heating to 250 °C to remove trace organic contaminants, aniline is drop-cast onto the graphene-coated GC electrode and dried; Step 5: chloroplatinic acid in ethanol is then drop-cast and annealed under argon atmosphere. This sample is referred to as the (Pt/Ani/Ar) sample. The control sample (Pt/Ar) is prepared by the same method but without aniline. **b**, X-ray diffraction patterns for pristine GC and a (Pt/Ani/Ar) sample on GC;

low magnification to high magnification atomic resolution HAADF-STEM images of (Pt/Ani/Ar) (**c**, **d**) and Pt/Ar (**e**, **f**).

The XRD patterns for the glassy carbon (GC) electrode and for (Pt/Ani/Ar) are shown in Fig. 3.1b.[35] The two patterns match well. In particular, the pattern for (Pt/Ani/Ar) lacks the intense peaks at about 39.8°, 46.2°, and 68.5° expected for the (111), (200), and (220) reflections in crystalline platinum (PDF#04-0802). This implies that the HAADF-STEM images, which show no platinum nanoparticles in (Pt/Ani/Ar), are representative of the bulk sample. The STEM images show that treatment with aniline promotes the formation of more atomically dispersed platinum.

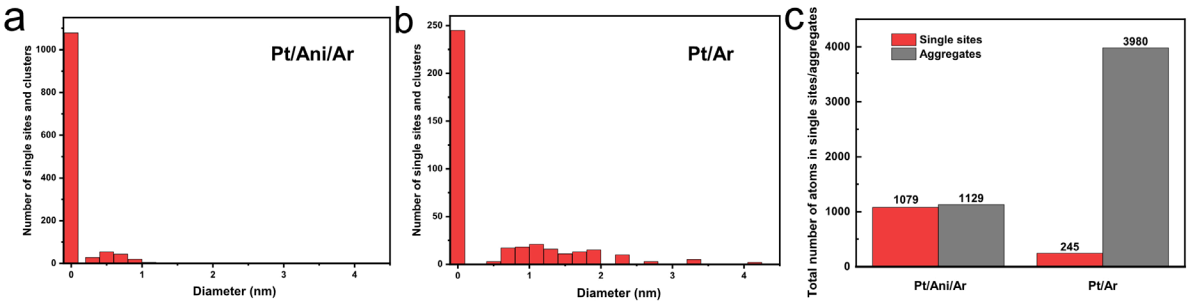


Figure 3.2: Representative histograms quantifying the number of Pt single site and aggregates diameters of (Pt/Ani/Ar) (**a**) and (Pt/Ar) (**b**) samples across an area of approximately 2000 nm^2 each from several STEM images. **c**, The total rough number of Pt atoms in single-site Pt and Pt aggregates in (Pt/Ani/Ar) and (Pt/Ar). A Pt single site is defined as when the distance between the site and its nearest neighbour atoms is larger than a metallic Pt-Pt bond; this diameter is defined as 0 in the histograms.

3.2.2 Ex-situ XPS and XAS

The platinum oxidation state is investigated by XPS, and the spectra for (Pt/Ani/Ar) and (Pt/Ar) are shown in Fig. 3.3a. Two standards are also shown: ammonium hexachloroplatinate(IV) ($(NH_4)_2PtCl_6$) and platinum(II) chloride ($PtCl_2$). The platinum $4f_{7/2}$ peak in $PtCl_2$ has a binding energy of 72.9 eV consistent with the +2 oxidation state. The $(NH_4)_2PtCl_6$ has a higher binding energy of 75.2 eV, which is also expected for its high oxidation state of +4. The spectrum for (Pt/Ani/Ar) is well fitted by a 74% contribution from a peak centred at 72.8 ± 0.1 eV and a 26% contribution from a peak centred at 74.6 ± 0.1 eV (Fig. 3.3a). These contributions likely arise from platinum(II) and platinum(IV),[36] respectively, indicating that the sample is a mixture of the two oxidation states.[24, 25, 37] The (Pt/Ar) is well fitted by a single peak centred at 73.0

± 0.1 eV arising from the +2 oxidation state.[38, 39] These oxidation-state assignments are consistent with the XANES spectra shown in Fig. 3.3b. Here, reference spectra for $PtCl_2$ (+2) and $(NH_4)_2PtCl_6$ (+4) have white line peak positions at 11565.8 eV and 11567.7 eV, respectively. The spectrum for (Pt/Ani/Ar) has a single peak centred at 11566.7 eV. This is expected of a mixture of platinum(II) and platinum(IV) and is consistent with the XPS data.[37, 38]]

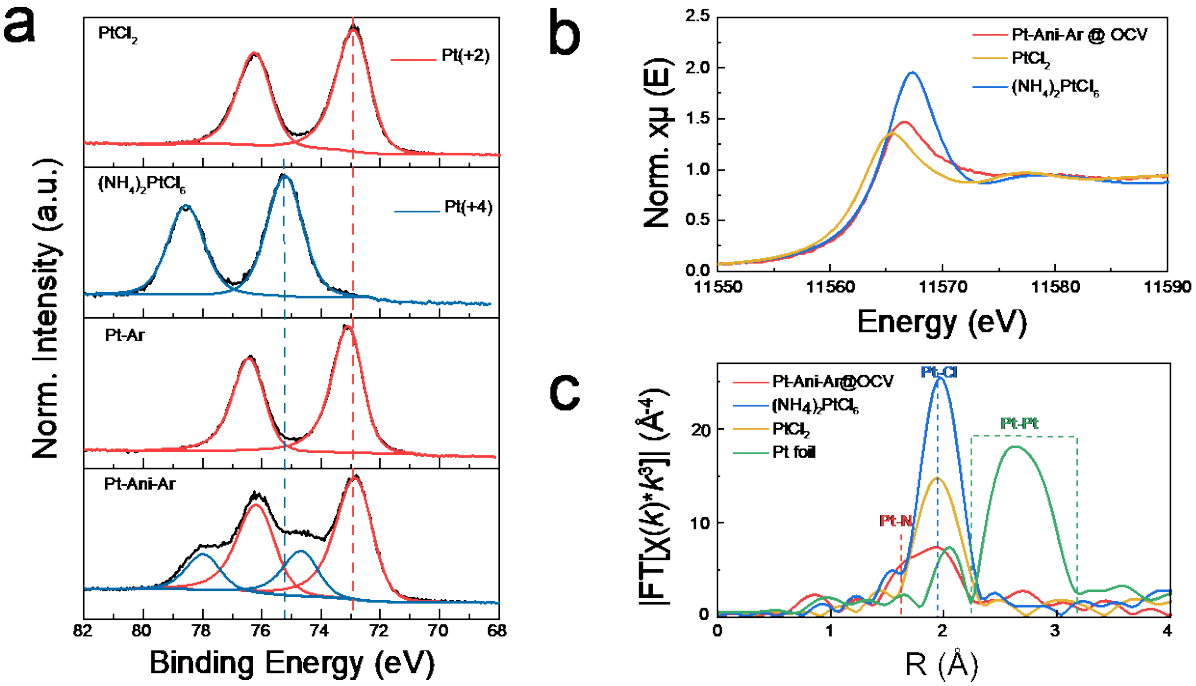


Figure 3.3: XPS spectra of Pt 4f (**a**) and XANES spectra (**b**) recorded at Pt L_3-edge for the synthesised Pt SSC and control sample (Pt/Ar) compared with reference standards in the oxidation states of platinum(II) and platinum(IV); all the sepctra are calibrated with C-C sp^3 at 248.8 eV. The vertical dashed red and blue lines in (a) indicate the peak positions of $Pt_{7/2}$ at the oxidation state of platinum(II) and platinum(IV). **c**, Corresponding k^3-weighted Fourier-transformed Pt L_3-edge EXAFS spectra of samples in (**b**) and standard Pt foil. The vertical dashed lines or area show the positions of Pt-N (red), Pt-Cl (blue), and Pt-Pt (green) peaks.

EXAFS spectra plotted in Fig. 3.3c (along with those of the standards) give information about the platinum bonding environment. The standard samples of $PtCl_2$ and $(NH_4)_2PtCl_6$ have one dominant peak in the range of 1.5 to 2.3 Å with the centre at 1.96 Å, suggesting that this peak can be associated with Pt-Cl bonding. The most intense peak in the spectrum for (Pt/Ani/Ar) is at 1.96 Å with a shoulder at 1.66 Å. The peak at 1.96 Å should arise from the presence of Pt-Cl bonds. This shoulder peak at 1.66 Å is indicative of platinum-nitrogen bonding.[40, 41] Finally, there is an absence of obvious Pt-Pt bonding at 2.73 Å (green curve in Fig. 3.3c),

which also suggests that the platinum atoms are mainly isolated from each other. Additionally, the Pt-Cl and Pt-N vibrations at 332 cm^{-1} and 445 cm^{-1} are recorded, as the Raman spectra are shown in Fig. 3.4. We, therefore, interpret these data to mean that the aniline and chloride coordinate with the platinum to form a complex molecule.

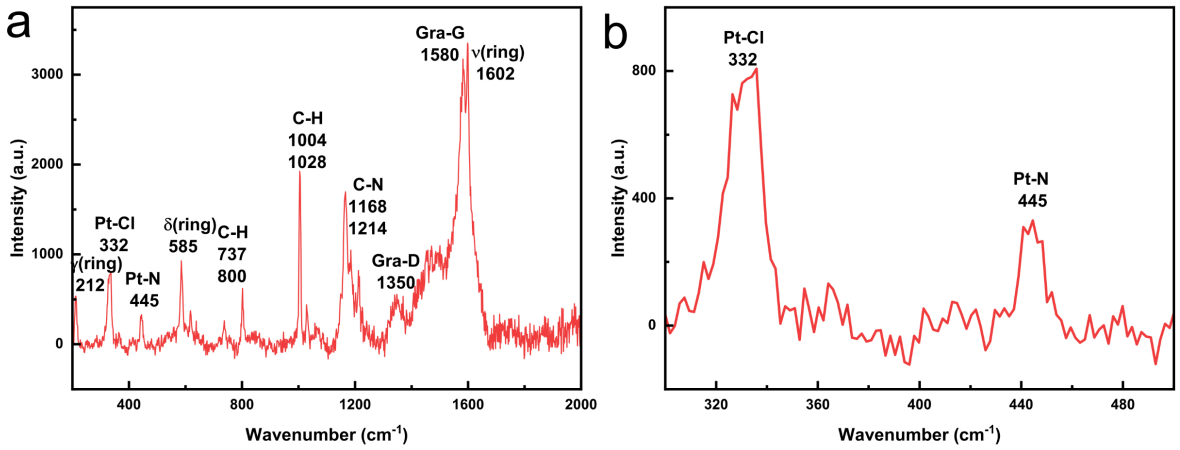


Figure 3.4: a, The Raman spectrum of the (Pt/Ani/Ar) sample. **b**, The enlarged area from 300 cm^{-1} to 500 cm^{-1} in (**a**) highlights two characteristic peaks at 332 cm^{-1} (Pt-Cl) and 445 cm^{-1} (Pt-N).

These XPS and XANES data indicate that (Pt/Ani/Ar) and (Pt/Ar) are reduced in situ from platinum(IV) (the oxidation state of platinum in the precursor H_2PtCl_6) to platinum(II). The cause of the reduction of Pt(IV) to Pt(II) is the ethanol used as a solvent to prepare the H_2PtCl_6 solution.[42] However, in (Pt/Ani/Ar) the platinum forms a complex with aniline (as confirmed by the bonding data from the EXAFS spectra). This is the reason that (Pt/Ani/Ar) is only partially reduced, with platinum(IV) still present. The STEM, XPS, XANES and EXAFS data, suggest that the aniline-treated sample contains atomically dispersed platinum in the form of molecular complexes (Pt single-site complexes) physisorbed onto the graphene substrate.

3.2.3 Operando XAS measurements

Operando hard XAS at the platinum L_3-edge was performed at different potentials to investigate the evolution of the platinum single-site complex's oxidation state and chemical bonding environment during HER.[23, 30, 43] A customised three-electrode cell setup, as shown in Fig. 2.5 in Chapter 2, was mounted to investigate the aniline-treated sample

(Pt/Ani/Ar). The chronoamperometric performance of (Pt/Ani/Ar) at various potentials is shown in Fig. 3.5a (with a particular shown in Fig. 3.5b). The areal current densities are shown for at least 1000 s of operation at each of 10 voltages: 0.4, 0.3, 0.2, 0.1, 0.06, 0.02, 0, -0.02, -0.04, and -0.06 V versus the reversible hydrogen electrode (RHE). The open-circuit voltage (OCV) is 0.6 V versus RHE. None of the tests at a positive potential has an areal current density greater than 0.1 mA cm^{-2}. This is to be expected since the HER is only thermodynamically favourable below 0 V versus RHE. Indeed, the data for the test at 0 V show a minimal areal current density until about 600 s (out of approximately 1,200 s in total) when the current jumps suddenly and then gradually increases to about -0.3 mA cm^{-2}. The areal current densities for the subsequent potentials of -0.02, -0.04, and -0.06 V versus RHE are -0.5, -0.9, and -1.5 mA cm^{-2}, respectively. The Tafel slope, calculated using the 4 negative potentials, is 60 mV dec^{-1}. This is comparable to the Tafel slope of platinum nanoparticles for the HER.[44, 45]]

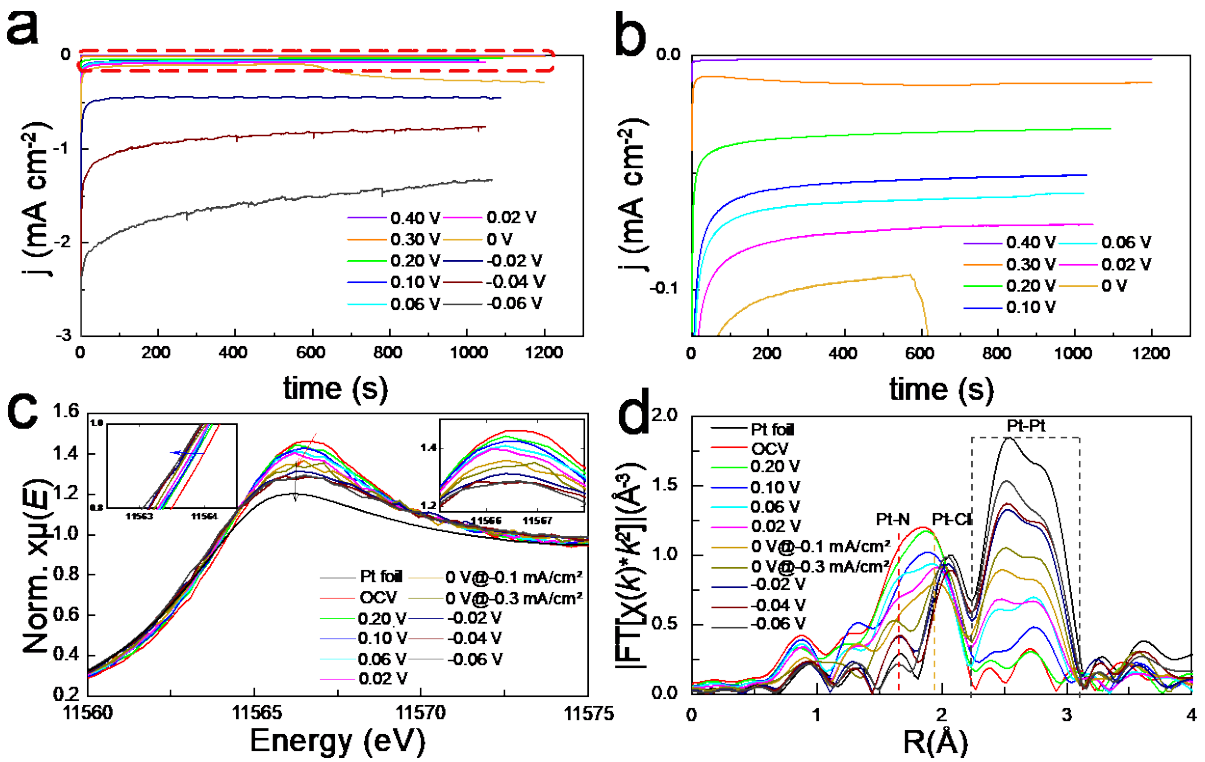


Figure 3.5: a, Stable chronoamperometric curves of Pt single-site complex at variable applied potentials; **b**, Enlarged red dashed area in (**a**) shows the chronoamperometric curves at current density smaller than 0.1 mA cm^{-2}; **c**, Operando XANES spectra recorded at Pt L_3-edge of synthesised Pt single-site complex sample at different working potentials for HER in 0.5 M H_2SO_4. The inset graphs show the energy shifts of Pt L_3 absorption edge (left) and white-line peak (right). **d**, The corresponding K^2-weighted Fourier-transformed EXAFS spectra

(magnitude component). The vertical dashed lines or area show the Pt-N (red), Pt-Cl (orange) and Pt-Pt (grey) peaks.

The average of eight XANES spectra, collected during operation at each potential, are shown in Fig. 3.5c. These data show that the oxidation state of platinum decreases from a mixture of +4 and +2 to 0. When the potential is decreased from 0.6 V (OCV) to 0 V versus RHE, the positions of both the white line (red arrow and right inset in Fig. 3.5c) and absorption edge (left inset in Fig. 3.5c) in the XANES spectra show a negative shift of 0.4 eV. Those shifts suggest a continuous decrease of platinum valence from a mixture of platinum(II) and platinum(IV) to metallic platinum.[23, 46]]

The bonding environment of the platinum also changes as the applied potential varies, as shown in the EXAFS spectra in Fig. 3.5d. As the potential is decreased from OCV to 0, the peaks at 1.66 and 1.96 Å, arising from Pt-N and Pt-Cl bonds, respectively, both decrease in intensity. But the peak arising from Pt-N (blue vertical line) decreases faster than that arising from Pt-Cl (orange vertical line). This indicates that as the potential is decreased from OCV and while the oxidation state of the platinum falls to 0, the aniline molecules are dissociating from the complex. The chloride ions are also dissociating from the platinum atoms, but to a lesser extent compared to the aniline molecules. At 0 V, the SSC has two distinct EXAFS spectra (yellow and olive curves in Fig. 3.5d): one at the low areal current density (-0.1 mA cm^{-2}) before the onset of the HER and one at the higher areal current density (-0.3 mA cm^{-2}) after the onset of the HER. Before the onset of the HER, the bonding environment still shows appreciable Pt-Cl bonding and some Pt-N bonding. After 600 s and the beginning of hydrogen evolution, almost all Pt-N bonding character is lost and the Pt-Cl bonding feature decreases significantly. The EXAFS spectrum is instead dominated by Pt-Pt bonding. The rapid breaking of Pt-N and Pt-Cl bonds at 0 V may be caused by hydrogen molecules aggregated on the SSC. It has been experimentally shown that the diffusion and agglomeration of platinum atoms can be induced by exposure to a hydrogen atmosphere.[47-50] Since more reduced platinum structures after 600 s can boost the evolution of hydrogen by lowering the Gibbs free energy

of hydrogen adsorption in acidic electrolytes,[23, 51] the sudden increase in current density here (the yellowish line discussed in Fig. 3.5a) can probably be justified accordingly.

3.2.4 Structure-electrochemistry correlation

The previous section elucidates the evolution of the Pt single-site complex into metallic nanoclusters at potentials below 0 V; the details of this transformation need to be quantitatively examined together with catalytic activity. The effect of applied potential on both areal current density and platinum oxidation state in the SSC is shown in Fig. 3.6a. The height of the XANES normalised white lines is summarised (black plot in Fig. 3.6a) to quantify the evolution of platinum's oxidation state and the electron occupancy of platinum's 5d orbitals.[52, 53] The white-line height decreases precipitously from OCV (0.60 V) to about 0 V versus RHE. This is consistent with the complete filling of the platinum 5d valence orbitals and the formation of metallic platinum.[23] At the same potential, the corresponding areal current density increases precipitously as the HER becomes thermodynamically favourable, although they are still relatively low (from -0.001 to -0.08 mA cm^{-2}). There is an obvious drop in white-line height at around 0 V, and the white-line height stabilises at around 1.30 after 0 V, indicating the oxidation state of platinum remains as 0 at potentials below 0 V. Corresponding to the decrease in oxidation state, a significant increase in current density is also recorded at 0 V (red plot in Fig. 3.6a). And after the increase, a linear relationship between the base-10 logarithm of the areal current density and the potentials is presented.

EXAFS curve-fitting analysis on the platinum's EXAFS spectrum at OCV allows for the determination of a plausible molecular structure for the platinum complex adsorbed onto graphene. Considering eight possible platinum complexes described by $(C_6H_5NH_2)_XCl_YPt$ for x = 1 or 2 and y = 1, 2, 3, or 4, the Pt-N and Pt-Cl bond lengths (about 2.05 Å and 2.30 Å, respectively) determined by density-functional theory modelling of the isolated molecular complexes are the starting point for the analysis. The operando EXAFS data are best described by the structural model for trans-dianilinedichloroplatinum(II), $(C_6H_5NH_2)_2Cl_2Pt$(II),

within the fitting range (K range: 3 to 12.5 Å, R range: 1.1 to 2.5 Å, misfit factor 0.8%). This structure is similar to the previously reported crystal $(C_6H_5NH_2)_2PtCl_2$ complex, prepared by mixing aniline with H_2PtCl_6. [54, 55]]

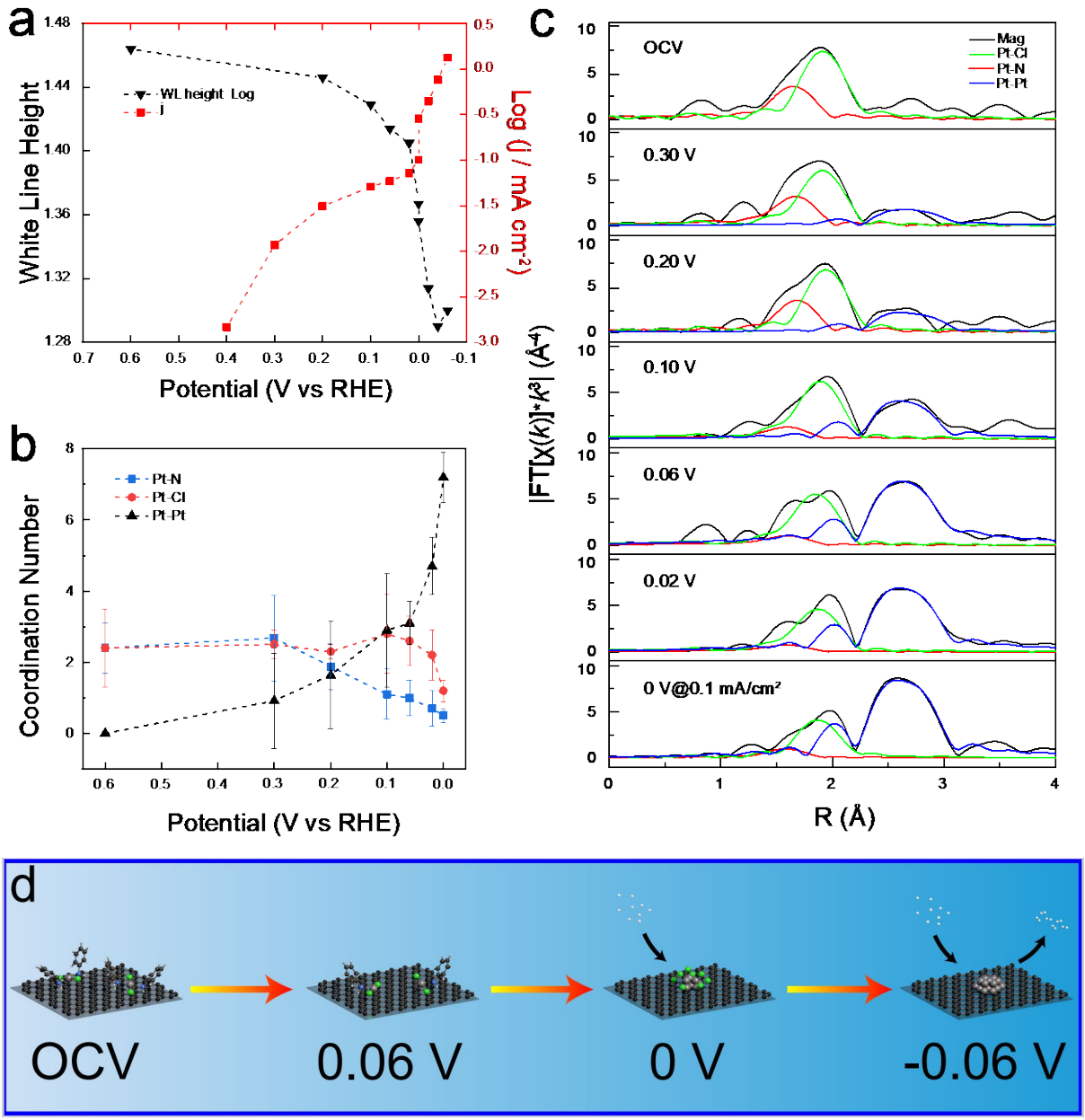


Figure 3.6: **a**, Amplitude of normalised white-line peak of Pt L_3-edge operando XANES spectra (black) and the corresponding catalytic activity (red) at different potentials. Log(j) is calculated using relatively stable current density at the end of each CA test. **b**, The Coordination number of Pt-N, Pt-Cl and Pt-Pt fitting paths for operando EXAFS data of Pt single-site complex at selected potentials by 0 V. Error bars in (**b**) represent the uncertainties of fitting results. **c**, Contribution of different paths (Pt-N, Pt-Cl and Pt-Pt) to fit the corresponding EXAFS spectra. **d**, Proposed schematic model for the evolution of (Pt/Ani/Ar) sample from single-site complex to subnanoclusters based on the operando EXAFS analysis (grey, Pt; green, Cl; blue, N; black, carbon; white, H).

Performing EXAFS curve-fitting analysis (platinum's first (1.5 to 2.1 Å) and second (2.3 to 3.1 Å) coordination shells) on the spectra collected at different potentials results in the curves in Fig. 3.6b, which shows the average number of platinum, chlorine, and nitrogen atoms coordinated to each platinum atom (i.e. the coordination number), as a function of applied potential. Specifically, Fig. 3.6c highlights the evolution of the EXAFS spectra while decreasing potential in the R-space fitted with the contributions of Pt-N, Pt-Cl and Pt-Pt paths. At OCV, the coordination number for both chlorine and nitrogen is about 2.5. As the potential is lowered, the coordination number for nitrogen decreases to about 1.0 by a potential of 0.1 V versus RHE. It continues to decrease to about 0.5 by 0 V (but before the onset of the HER). The chlorine coordination number stays higher than the nitrogen coordination number. This indicates that the aniline molecules dissociate from the complex before the chloride ions do, likely due to the more ionic character and higher bond energy of the Pt-Cl bonds compared to the Pt-N bonds.[56] The platinum coordination number increases as the potential is lowered, ultimately reaching a value of about 7.0 by 0 V versus RHE. This indicates the agglomeration of platinum as the potential is lowered, which is also in line with the reduction of the oxidation state of platinum described in Fig. 3.6a.[57]

Together these data elucidate how the platinum bonding environment in an SSC changes as a function of applied potential during operation, as described schematically in Fig. 3.6d. As the potential is lowered from OCV, the dianilinedichloroplatinum(II) decomposes as the aniline dissociates from the platinum, followed by the dissociation of the chloride ions. Simultaneously, the 5d valence orbitals of platinum are filled. By the onset of HER at 0 V versus RHE, the dianilinedichloroplatinum(II) complexes have completely dissociated, and the metallic platinum(0) single atoms agglomerate into nanoclusters which catalyse the HER.

3.3 Conclusion

In this work, we use operando, synchrotron X-ray absorption spectroscopy to characterise how the oxidation state and bonding environment of platinum changes in an SSC for the HER at the molecular level. First, we show successful synthesis of a platinum SSC, confirming the platinum is atomically dispersed by STEM and XRD. We observe a mixture of platinum(II) and platinum(IV) by XPS and XANES, and we confirm platinum coordination to aniline by ex-situ EXAFS. We then probe the oxidation state and molecular structure as a function of applied potential using operando EXAFS and XANES with synchrontron radiation. We find that as the potential is lowered from OCV the platinum oxidation state decreases, breaking bonds between platinum atoms and aniline ligands first. The Pt-Cl bonds also break, but to a lesser extent than the Pt-N bonds. Finally, once the onset of the HER at 0 V versus RHE is reached, the platinum is completely reduced and metallic platinum atoms agglomerate to form catalytic nanoclusters. Our work suggests that many single-site catalysts that achieve atomically dispersed platinum by ligand coordination do not remain atomically dispersed during device operation. This demonstrates that researchers should be extremely careful when assuming that the bonding environment of the as-synthesised SSC will remain the same during device operation. Furthermore, this operando study establishes two important structure-property relationships for aniline-complex platinum SSCs. First, platinum exists as metallic platinum (that is, in the oxidation state 0) while catalysing the HER. Second, the molecular structure of the platinum complexes is lost due to the reduction of the platinum. These findings highlight the necessity for operando techniques to follow the dynamic behaviour of SSCs during operation and provide critical new insight into why SSCs deactivate over time. Such experiments can also provide an important contribution to an atomic understanding of the structural evolution of SSC systems as well as SACs for other critical electrochemical reactions, such as oxygen reduction reaction and carbon dioxide reduction reaction. These

results and the operando X-ray spectroscopy method used in this study will accelerate the development of stable, high-performance platinum SSCs for clean hydrogen production.

3.4 References

1. Taibi, E. *et al*. Hydrogen from Renewable Power: Technology Outlook for the Energy Transition. (2018).

2. Lagadec, M. F. & Grimaud, A. Water electrolysers with closed and open electrochemical systems. *Nature Materials 2020 19:11* **19**, 1140–1150 (2020).

3. McCrory, C. C. L. *et al*. Benchmarking Hydrogen Evolving Reaction and Oxygen Evolving Reaction Electrocatalysts for Solar Water Splitting Devices. *J Am Chem Soc* **137**, 4347–4357 (2015).

4. Cui, X., Li, W., Ryabchuk, P., Junge, K. & Beller, M. Bridging homogeneous and heterogeneous catalysis by heterogeneous single-metal-site catalysts. *Nature Catalysis 2018 1:6* **1**, 385–397 (2018).

5. Kibsgaard, J. & Chorkendorff, I. Considerations for the scaling-up of water splitting catalysts. *Nature Energy 2019 4:6* **4**, 430–433 (2019).

6. Thomas, J. M., Raja, R. & Lewis, D. W. Single-Site Heterogeneous Catalysts. *Angewandte Chemie International Edition* **44**, 6456–6482 (2005).

7. Pelletier, J. D. A. & Basset, J. M. Catalysis by Design: Well-Defined Single-Site Heterogeneous Catalysts. *Acc Chem Res* **49**, 664–677 (2016).

8. Thomas, J. M. The concept, reality and utility of single-site heterogeneous catalysts (SSHCs). *Physical Chemistry Chemical Physics* **16**, 7647–7661 (2014).

9. Li, Z., Wang, D., Wu, Y. & Li, Y. Recent advances in the precise control of isolated single-site catalysts by chemical methods. *Natl Sci Rev* **5**, 673–689 (2018).

10. Ye, S. *et al*. Highly stable single Pt atomic sites anchored on aniline-stacked graphene for hydrogen evolution reaction. *Energy Environ Sci* **12**, 1000–1007 (2019).

11. Li, C. *et al*. Polyvinylpyrrolidone-Coordinated Single-Site Platinum Catalyst Exhibits High Activity for Hydrogen Evolution Reaction. *Angewandte Chemie International Edition* **59**, 15902–15907 (2020).

12. Chen, Y. *et al*. Single-Atom Catalysts: Synthetic Strategies and Electrochemical Applications. *Joule* **2**, 1242–1264 (2018).

13. Yang, X. F. *et al*. Single-atom catalysts: A new frontier in heterogeneous catalysis. *Acc Chem Res* **46**, 1740–1748 (2013).

14. Wang, A., Li, J. & Zhang, T. Heterogeneous single-atom catalysis. *Nature Reviews Chemistry 2018 2:6* **2**, 65–81 (2018).

15. Zhang, J. *et al*. Single platinum atoms immobilized on an MXene as an efficient catalyst for the hydrogen evolution reaction. *Nature Catalysis 2018 1:12* **1**, 985–992 (2018).

16. Tang, C. *et al*. Tailoring Acidic Oxygen Reduction Selectivity on Single-Atom Catalysts via Modification of First and Second Coordination Spheres. *J Am Chem Soc* **143**, 7819–7827 (2021).

17. Pang, J., Chang, B., Liu, H. & Zhou, W. Potential of MXene-Based Heterostructures for Energy Conversion and Storage. *ACS Energy Lett* **7**, 78–96 (2022).

18. Mitchell, S., Vorobyeva, E. & Pérez-Ramírez, J. The Multifaceted Reactivity of Single-Atom Heterogeneous Catalysts. *Angewandte Chemie International Edition* **57**, 15316–15329 (2018).

19. Copéret, C. Single-Sites and Nanoparticles at Tailored Interfaces Prepared via Surface Organometallic Chemistry from Thermolytic Molecular Precursors. *Acc Chem Res* **52**, 1697–1708 (2019).

20. Zhao, D. *et al*. Atomic site electrocatalysts for water splitting, oxygen reduction and selective oxidation. *Chem Soc Rev* **49**, 2215–2264 (2020).

21. Zhao, S., Yang, Y. & Tang, Z. Insight into Structural Evolution, Active Sites, and Stability of Heterogeneous Electrocatalysts. *Angewandte Chemie International Edition* **61**, e202110186 (2022).

22. Li, X., Yang, X., Zhang, J., Huang, Y. & Liu, B. In Situ/Operando Techniques for Characterization of Single-Atom Catalysts. *ACS Catal* **9**, 2521–2531 (2019).

23. Fang, S. *et al*. Uncovering near-free platinum single-atom dynamics during electrochemical hydrogen evolution reaction. *Nature Communications 2020 11:1* **11**, 1–8 (2020).

24. Kaiser, S. K. *et al*. Nanostructuring unlocks high performance of platinum single-atom catalysts for stable vinyl chloride production. *Nature Catalysis 2020 3:4* **3**, 376–385 (2020).

25. Ren, Y. *et al*. Unraveling the coordination structure-performance relationship in Pt_1/Fe_2O_3 single-atom catalyst. *Nature Communications 2019 10:1* **10**, 1–9 (2019).

26. Hübner, S., de Vries, J. G. & Farina, V. Why Does Industry Not Use Immobilized Transition Metal Complexes as Catalysts? *Adv Synth Catal* **358**, 3–25 (2016).

27. Timoshenko, J. & Roldan Cuenya, B. In Situ/ Operando Electrocatalyst Characterization by X-ray Absorption Spectroscopy. *Chem Rev* **121**, 882–961 (2021).

28. Malta, G. *et al*. Deactivation of a Single-Site Gold-on-Carbon Acetylene Hydrochlorination Catalyst: An X-ray Absorption and Inelastic Neutron Scattering Study. *ACS Catal* **8**, 8493–8505 (2018).

29. Liu, L. *et al*. Determination of the Evolution of Heterogeneous Single Metal Atoms and Nanoclusters under Reaction Conditions: Which Are the Working Catalytic Sites? *ACS Catal* **9**, 10626–10639 (2019).

30. Maurer, F. *et al*. Tracking the formation, fate and consequence for catalytic activity of Pt single sites on CeO_2. *Nature Catalysis 2020 3:10* **3**, 824–833 (2020).

31. Fei, H. *et al*. Single atom electrocatalysts supported on graphene or graphene-like carbons. *Chem Soc Rev* **48**, 5207–5241 (2019).

32. Lee, J. K. *et al*. Metal atom markers for imaging epitaxial molecular self-assembly on graphene by scanning transmission electron microscopy. *ACS Nano* **13**, 7252–7260 (2019).

33. Li, Y. *et al*. An oxygen reduction electrocatalyst based on carbon nanotube–graphene complexes. *Nature Nanotechnology 2012 7:6* **7**, 394–400 (2012).

34. Li, X. *et al*. Precursor Design for High Density Single Pt Atom Sites on MoS_2: Enhanced Stability at Elevated Temperatures and Reduced 3D Clustering. *Chemistry of Materials* **32**, 2541–2551 (2020).

35. Shiell, T. B. *et al*. In situ analysis of the structural transformation of glassy carbon under compression at room temperature. *Phys Rev B* **99**, 024114 (2019).

36. Yang, M. *et al*. A Common Single-Site Pt(II)-$O(OH)_x$- Species Stabilized by Sodium on 'active' and 'inert' Supports Catalyzes the Water-Gas Shift Reaction. *J Am Chem Soc* **137**, 3470–3473 (2015).

37. Liu, J. *et al*. High performance platinum single atom electrocatalyst for oxygen reduction reaction. *Nature Communications 2017 8:1* **8**, 1–10 (2017).

38. Cheng, X. *et al*. Highly active, stable oxidized platinum clusters as electrocatalysts for the hydrogen evolution reaction. *Energy Environ Sci* **10**, 2450–2458 (2017).

39. Imaoka, T. *et al*. Platinum clusters with precise numbers of atoms for preparative-scale catalysis. *Nature Communications 2017 8:1* **8**, 1–8 (2017).

40. Lim, T. *et al*. Atomically dispersed Pt–N_4 sites as efficient and selective electrocatalysts for the chlorine evolution reaction. *Nature Communications 2020 11:1* **11**, 1–11 (2020).

41. Li, X. *et al*. Single-Atom Pt as Co-Catalyst for Enhanced Photocatalytic H_2 Evolution. *Advanced Materials* **28**, 2427–2431 (2016).

42. Obreja, L.; Foca, N.; Popa, M.; Melnig, V. Alcoholic reduction platinum nanoparticles synthesis by sonochemical method. *Biomaterials in Biophysics, Medical Physics and Ecology*, **31** (2008).

43. Wang, J. *et al*. In Situ Identifying the Dynamic Structure behind Activity of Atomically Dispersed Platinum Catalyst toward Hydrogen Evolution Reaction. *Small* **17**, 2005713 (2021).

44. Ghanim, A. H. *et al*. Low-loading of Pt nanoparticles on 3D carbon foam support for highly active and stable hydrogen production. *Front Chem* **6**, 523 (2018).

45. Kang, J. *et al*. Platinum Atoms and Nanoparticles Embedded Porous Carbons for Hydrogen Evolution Reaction. *Materials 2020, Vol. 13, Page 1513* **13**, 1513 (2020).

46. Mansour, A. N., Cook, J. W. & Sayers, D. E. Quantitative technique for the determination of the number of unoccupied d-electron states in a platinum catalyst using the $L_{2,3}$ X-ray absorption edge spectra. *Journal of Physical Chemistry* **88**, 2330–2334 (1984).

47. Horch, S. *et al*. Enhancement of surface self-diffusion of platinum atoms by adsorbed hydrogen. *Nature 1999* 398:6723 **398**, 134–136 (1999).

48. Parkinson, G. S. *et al*. Carbon monoxide-induced adatom sintering in a Pd–Fe_3O_4 model catalyst. *Nature Materials 2013 12:8* **12**, 724–728 (2013).

49. Dessal, C. *et al*. Atmosphere-dependent stability and mobility of catalytic Pt single atoms and clusters on γ-Al_2O_3. *Nanoscale* **11**, 6897–6904 (2019).

50. Liu, L. *et al*. Regioselective Generation of Single-Site Iridium Atoms and Their Evolution into Stabilized Subnanometric Iridium Clusters in MWW Zeolite. *Angewandte Chemie International Edition* **59**, 15695–15702 (2020).

51. Shi, Y. *et al*. Electronic metal–support interaction modulates single-atom platinum catalysis for hydrogen evolution reaction. *Nature Communications 2021 12:1* **12**, 1–11 (2021).

52. Wang, J. *et al*. Redirecting dynamic surface restructuring of a layered transition metal oxide catalyst for superior water oxidation. *Nature Catalysis 2021 4:3* **4**, 212–222 (2021).

53. Malta, G. *et al*. Identification of single-site gold catalysis in acetylene hydrochlorination. *Science (1979)* **355**, (2017).

54. Mohanraju, K., Lee, H. & Kwon, O. J. High Loading Pt Core/Carbon Shell Derived from Platinum-Aniline Complex for Direct Methanol Fuel Cell Application. *Electroanalysis* **30**, 1604–1609 (2018).

55. Kong, P. C. & Rochon, F. D. Cis- and trans-platinum complexes of anilines. A study of isormerization reactions. *Inorganica Chim Acta* **61**, 269–271 (1982).

56. Astakhov, A. v., Soliev, S. B. & Chernyshev, V. M. Metal-ligand bond dissociation energies in the Ni, Pd, and Pt complexes with N-heterocyclic carbenes: effect of the oxidation state of the metal (0, +2). *Russian Chemical Bulletin 2020 69:11* **69**, 2073–2081 (2020).

57. Hao, X. *et al*. Direct measurement and modulation of single-molecule coordinative bonding forces in a transition metal complex. *Nature Communications 2013 4:1* **4**, 1–10 (2013).

Chapter 4

Chemically bonded Pt SSC

4.1 Introduction

This chapter investigates the synthesis, structure, and HER activity of Pt single sites chemisorbed on the polyaniline substrate.

As discussed in the previous chapter, the single-site Pt complex physically adsorbed on graphene substrate is not stable for the HER. The ligands of the physically adsorbed Pt SSC will dissociate from Pt sites, and the Pt sites will be reduced and aggregated into nanoparticles with applied HER working potentials. Therefore, stronger interactions between Pt single sites and supporting substrates are needed to maintain its atomic structure under the HER conditions, such as chemical interactions. However, due to the complex surface chemistries, it is challenging to synthesise a well-defined Pt SSC chemisorbed on the carbon-based substrate.[1] The atomic structure and the HER activity of those Pt SSC remain unclear.[2]

To obtain a well-defined Pt SSC, polyaniline is used as a supporting substrate to anchor platinum sites via the wet impregnation method.[3] The structure of this chemisorbed Pt SSC (Pt-PANI) is clarified by complementary characterisation techniques, including STEM, FT-IR, EXAFS, and XPS. Then, the HER activity of this chemisorbed Pt SSC is evaluated with our static three-electrode system based on a ring disk electrode. Finally, the structure of the chemisorbed Pt SSC after the CV activation and activity test is characterised to clarify the active structure of Pt for the HER. This chapter sets out the synthesis strategy, defines the structure, and clarifies the HER activity of chemically adsorbed platinum SSCs.

4.2 Results and discussion

4.2.1 Synthesis of Pt single sites on polyaniline

To obtain the chemisorbed Pt SSC, we anchor Pt single sites on polyaniline (Pt-PANI) via the wet impregnation method. Polyaniline (PANI) is a commonly used substrate to anchor transition metal precursors because it has sufficient N sites to coordinate with metal ions.[4, 5] In addition, the porous structure of PANI and the electrostatic interaction between PANI (the oxidised emeraldine type) and Pt ions can mitigate the aggregation of metal sites.[6-8]

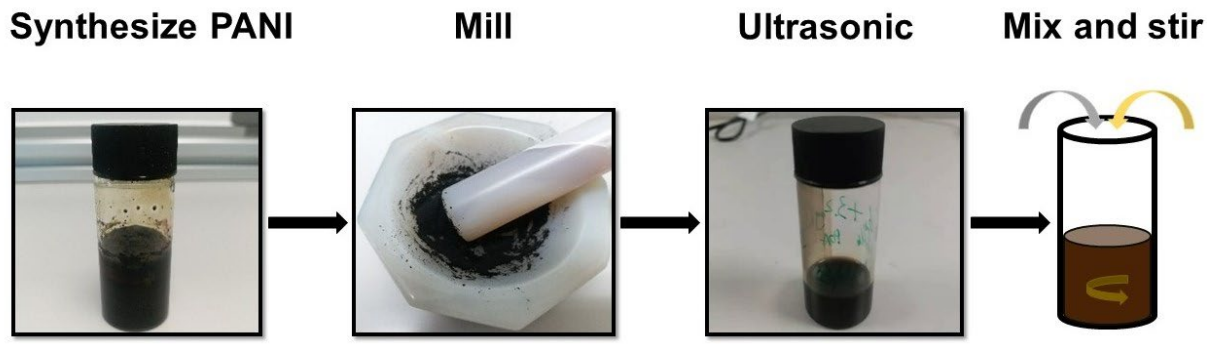


Figure 4.1: Schematic of the preparation process of the Pt-PANI samples.

The preparation of the Pt-PANI structure includes four steps, as shown in Fig. 4.1. Firstly, PANI was synthesised by the oxidative polymerisation of aniline in the hydrochloric acid solution. The PANI powder was then milled to a uniform particle size of around 1-5 μm. Afterward, the PANI powder was well-dispersed in ethanol solution with a concentration of 1 mg mL^{-1} by an ultrasonic process. Finally, the H_2PtCl_6 (10 mM in ethanol) was added dropwise to the PANI suspension under continuous magnetic stirring for 4 hrs. During the stirring process, the polyaniline was impregnated by the Pt sites from the H_2PtCl_6 ethanol solution to form a Pt-PANI mixture.

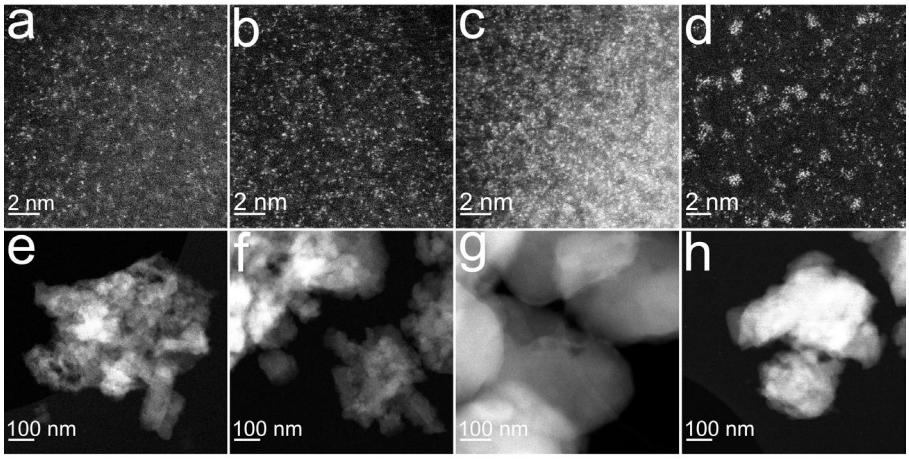


Figure 4.2: ADF-STEM images of 2 wt% **(a, e**), 5 wt% (**b, f**), 10 wt% (**c, g**), and 15 wt% (**d, h**) Pt-PANI samples show Pt sites can be atomically dispersed on PANI substrate with loading amount up to 10 wt%.

As the high-resolution HAADF-STEM images in Fig. 4.2a-c and e-g show, Pt sites are atomically dispersed on the polyaniline substrate. The images a-c and e-g show the Pt-PANI samples with a Pt loading of 2 wt% (a, e), 5 wt% (b, f), and 10 wt% (c, g). However, as shown in Fig. 4.2d and h, some Pt sites will aggregate into small clusters as the loading amount goes above 15 wt%. This is because Pt sites are too crowded to be isolated from surrounding Pt sites when the Pt loading is too high. Therefore, there is an upper limit for the Pt loading to be anchored as a single-site structure on the PANI substrate via the simple impregnation process.

4.2.2 Chemical structure of Pt-PANI

The interaction between Pt single sites and PANI was investigated by infrared spectroscopy (IR) and ex-situ XAS. By comparing the Fourier-transformed IR spectra of the 10 wt% Pt-PANI sample (red) and pristine PANI sample (blue) in Fig. 4.3a, alongside the characteristic peaks of PANI, new vibrations of Pt-Cl and Pt-N are present at 334/370 cm^{-1} and 920/1003 cm^{-1} respectively in the Fourier-transformed IR spectra of the Pt-PANI sample.[9] These new vibrations indicate that Pt sites are anchored on the PANI substrate by chemically interacting with N, and Pt sites are still bonding with the remaining Cl ligands from the H_2PtCl_6 precursor.

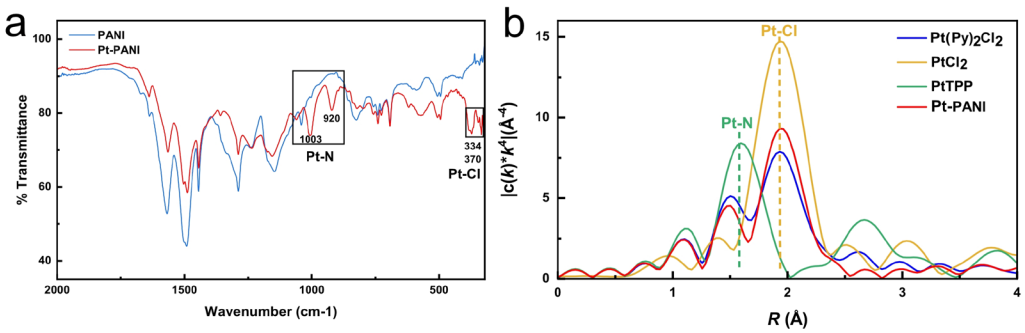


Figure 4.3: a, FT-IR spectra of 10 wt% Pt single sites on PANI (Pt-PANI). **b**, FT-EXAFS spectra of $PtCl_2$, PtTPP, $Pt(Py)_2Cl_2$, and Pt-PANI.

To clarify the chemical structure of Pt-PANI and provide information on the bonding environment of Pt, EXAFS of Pt-PANI was performed on the Pt L_3-edge and compared with reference Pt structures. As shown in Fig. 4.3b, the FT-EXAFS spectra of $PtCl_2$ (platinum chloride, yellow) and PtTPP (platinum(II) meso-tetraphenylporphine, green) demonstrate the reference peak positions of Pt-Cl and Pt-N at 1.93 Å and 1.56 Å, respectively. And the Pt-PANI (red) and $Pt(Py)_2Cl_2$ (Dichloro[bis(pyridine)]platinum(2+), blue) feature almost two identical peaks at 1.93 Å and 1.50 Å, corresponding to Pt-Cl and Pt-N peaks. The EXAFS data further supports that Pt single sites bond with N on the PANI substrate and Cl ligands from the precursor (Pt-Cl) at the Pt-PANI sample.

To further clarify the nature of Pt sites at the Pt-PANI sample, the XPS spectra of Pt core level, N 1s, and Cl 2p are recorded in Fig. 4.4. As Fig. 4.4a shows, the Pt $4f_{7/2}$ peak has a binding energy of ~72.9 eV, which corresponds to an oxidation state of +2.[3, 10] Therefore Pt is partially reduced from a +4 to a +2 oxidation state, going from the precursor of H_2PtCl_6 (in ethanol) to being anchored on the PANI substrate. After Pt single sites are anchored on PANI, the N 1s peak of PANI substrate positively shifts by 0.2 eV (Fig. 4.4b), meaning there may be a slight donation of electrons from N. More importantly, from the Cl 2p spectra of Pt-PANI in Fig. 4.4c, except for the organic Cl from own-synthesised PANI, there is a clear presence of metallic Cl peaks (red peak) at ~198.2 eV, which directly proves that Pt-Cl ligands from the precursor are being anchored on the PANI substrate.[10]

Overall, by combining the STEM, FT-IR, EXAFS, and XPS data, it is confirmed that a well-defined single-site structure (Pt-PANI) is obtained. At the Pt-PANI sample, Pt (+2) sites are atomically chemisorbed on the PANI by bonding with N at the substrate and Cl ligands from the precursor.

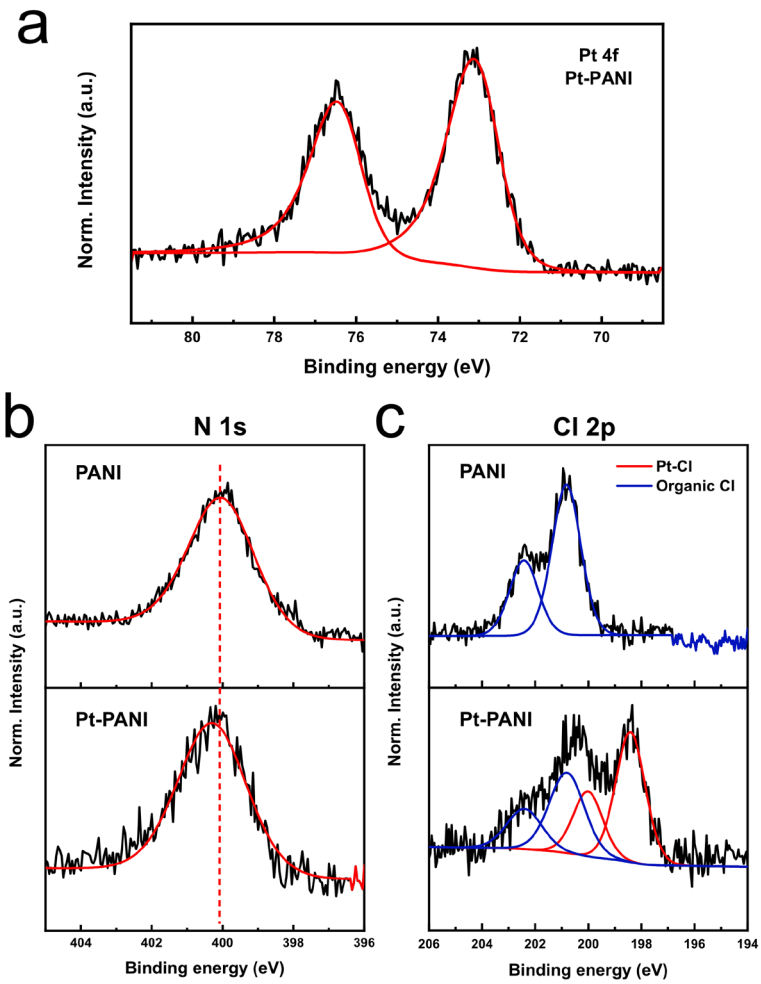


Figure 4.4: XPS spectra of Pt 4f (**a**), N 1s (**b**), and Cl 2p (**c**) of PANI before and after the impregnation of Pt sites (the PANI and the 10 wt% Pt-PANI sample).

4.2.3 HER activity of the chemisorbed Pt single sites on PANI substrate

After the chemisorbed Pt-PANI samples' structure was defined, their catalytic activities were evaluated under our static three-electrode system. The three-electrode system is based on

the rotating ring disk electrode developed by the PINE Research company.[11] The ring disk electrode made of glassy carbon is used as the working electrode; Hg/Hg_2SO_4 as the reference electrode and a graphite rod with a large surface area as the counter electrode. These three electrodes are put together into a 0.5 M H_2SO_4 solution saturated with pure Argon (A photograph of the cell is provided in Fig. 4.5a).

The Pt-PANI samples with 2 wt% and 10 wt% Pt loading were prepared via the impregnation process mentioned above to clarify the HER activity of the chemisorbed Pt SSC. The PANI substrate has a relatively low electrical conductivity which could limit the evaluation of the catalytic activity of the Pt structure.[12] To prevent this problem, carbon black was added and mixed with Pt-PANI to prepare a catalyst suspension. Then, ~15 µL of the suspension (~30 µg of the material) was drop cast on the ring disk electrode (with a geometric area of 0.196 cm^2) for activity tests. By rotating the ring disk, Pt catalysts were uniformly coated on the electrode, as shown in Fig. 4.5b.

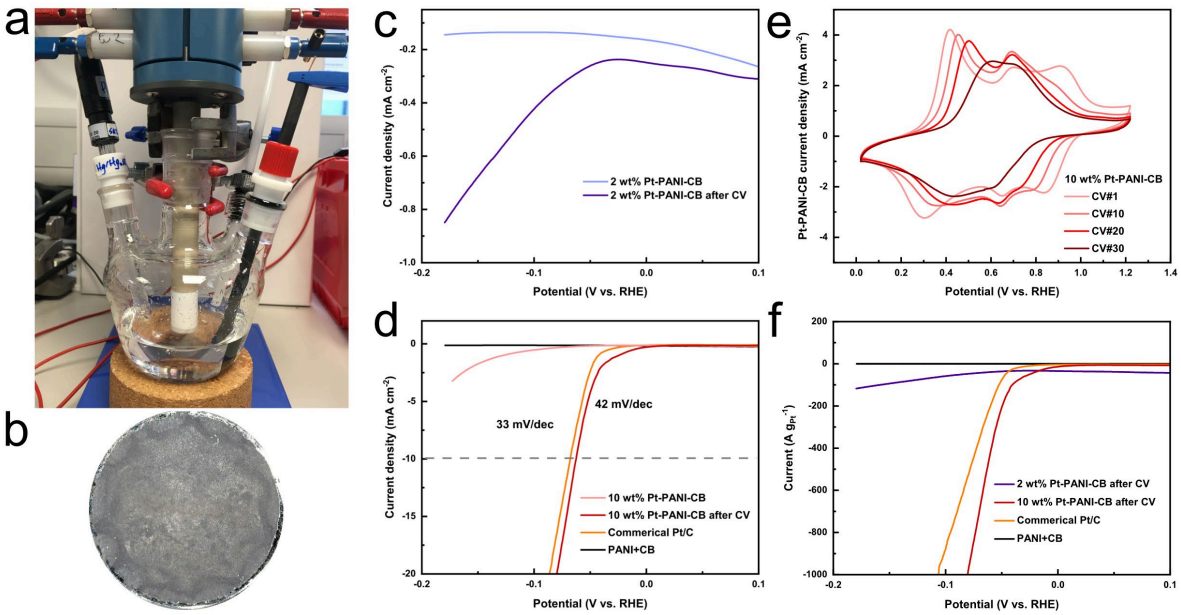


Figure 4.5: a, Photograph of static three-electrode system based on the ring disk electrode. **b**, A typical image of a uniform coating of Pt-PANI samples on the working electrode. **c**, **d**, Polarisation curves of 2 wt% Pt-PANI and 10 wt% Pt-PANI for the HER activity. **e**, 30 CV activation scans for 2/10 wt% Pt-PANI from 0 V to 1.2 V vs. RHE. **f**, Comparison of the mass activity of PANI+CB, 2 wt% Pt-PANI, 10 wt% Pt-PANI, and commercial 20 wt% Pt/C samples.

The HER catalytic activity was analysed using linear sweep voltammetry (LSV) at a scan rate of 5 mV/s. As the polarisation curves show in Fig. 4.5c, the 2 wt% Pt-PANI sample did not

present any detectable activity for the HER at the first LSV scan, which means the as-prepared Pt (+2) sites anchored on this sample are not active for the HER. Therefore, 30 cyclic voltammetry (CV) scans from ~0 V to +1.2 V vs. RHE at a scan rate of 50 mV/s were applied to activate the Pt sites. As the CV curves in Fig. 4.5e show, there are apparent changes in the peaks of CV scans. According to the literature, these changes are related to the oxidation/reduction of N in the Pt-PANI samples.[13, 14]]

Interestingly, after the CV activation, some increase in the catalytic activity for the 2 wt% Pt-PANI is recorded (Fig. 4.5c), even if the activity is still low compared to commercial 20 wt% Pt/C. In comparison, a dramatic increase in the HER catalytic activity after CV scans was recorded at the 10 wt% Pt-PANI sample (Fig 4.5d). At the first LSV scan, its catalytic activity is also inferior to Pt/C, but after 30 CV scans, only 70 mV overpotential is needed for the sample to reach a geometric current density of 10 mA cm^{-2}, which is comparable to the activity of the commercial Pt/C.

These results confirmed that the as-prepared Pt (+2) single sites chemisorbed on PANI substrate are not active catalysts for the HER. When the loading of Pt is high, Pt sites at Pt-PANI samples can be activated after the oxidation/reduction of N on the PANI substrate by CV scans. The active structure for HER of the 10 wt% Pt-PANI after CV scans need to be further clarified.

4.2.4 Structure of Pt-PANI after activity tests

To clarify the active structure of the chemisorbed 2 wt% and 10 wt% Pt-PANI for HER, the oxidation state and thestructure of Pt after the CV activation were checked by ex-situ XPS and high-resolution STEM.

The XPS spectra of Pt core level for 2 wt% Pt-PANI in Fig. 4.6a show that the binding energy of Pt 4f remains almost the same after the CV activation, but the metallic Cl peak from Pt-Cl disappears. And as shown in Fig. 4.6b,c, these chemisorbed Pt sites still are isolated, and no

obvious nanoparticles are formed after activation. These data further prove that Pt single sites at an oxidation state of +2 are not the desired structure for the HER. Comparatively, the Pt sites of the 10 wt% Pt-PANI show an apparent reduction after CV scans. As the Pt 4f XPS spectra in Fig. 4.6d show, after CV scans, in addition to the peaks of Pt (+2), metallic Pt peaks (blue) with a binding energy of 71.4 eV are observed. Also, many Pt nanoparticles with a size of around 2-5 nm are also present on PANI substrates after EC tests, which is directly shown from the high-resolution STEM images in Fig. 4.6e,f.

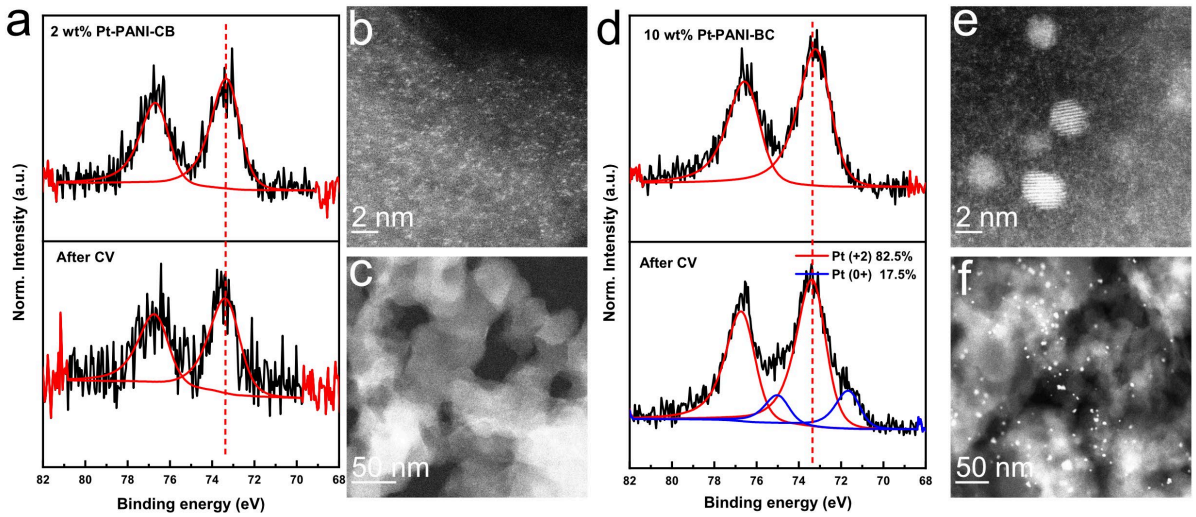


Figure 4.6: Pt 4f XPS spectra of 2 wt% (**a**) and 10 wt% (**d**) Pt-PANI samples before and after the CV activation. STEM images of the 2 wt% (**b, c**) and 10 wt% (**e, f**) Pt-PANI samples after the CV scans to clarify their active structure for the HER.

Comparing HER activities and structures of 2 wt%/10 wt% Pt-PANI samples before and after the CV activation, the as-prepared oxidised Pt (+2) sites on PANI are not active structures for the HER until they are reduced and aggregated into Pt metallic nanoparticles. The highly dispersed small Pt nanoparticles formed show a higher HER catalytic activity than commercial Pt/C. Our experiments clarified that the chemisorbed Pt (+2) SSC is not the active structure for HER. They also show these Pt sites are not stable and will be reduced to nanoparticles at repetitive CV scans.

4.3 Conclusion

This work successfully synthesised a model Pt SSC chemically anchored on the polyaniline substrate with a Pt loading from 2 wt% to 10 wt%. With the advantage of complementary characterisation techniques, it is found that Pt (+2) sites are atomically chemisorbed on the PANI by interacting with N at the substrate and remaining Cl ligands of Pt-Cl. After the structure of the chemisorbed Pt SSC is defined, its activity for the HER is also clarified. Unfortunately, the oxidised Pt single sites anchored on PANI are not active. After repeated CV scanning, the N at PANI substrate is changed, and these Pt (+2) sites are prone to be reduced and aggregated into nanoparticles, which are found to be active for the HER. Our findings prove that the chemisorbed single Pt sites bonding to N at an oxidation state of +2 is not desired for the HER, and the chemisorption interaction between Pt sites and the PANI substrate is still not robust enough to prevent Pt sites from aggregating at reduction potentials.

4.4 References

1. Korzyński, M. D. & Copéret, C. Single sites in heterogeneous catalysts: separating myth from reality. *Trends Chem* **3**, 850–862 (2021).

2. Pu, Z. *et al*. Single-Atom Catalysts for Electrochemical Hydrogen Evolution Reaction: Recent Advances and Future Perspectives. *Nano-Micro Letters* 2020 12:1 **12**, 1–29 (2020).

3. Kaiser, S. K. *et al*. Nanostructuring unlocks high performance of platinum single-atom catalysts for stable vinyl chloride production. *Nature Catalysis* 2020 3:4 **3**, 376–385 (2020).

4. Wu, G. *et al*. Synthesis–structure–performance correlation for polyaniline–Me–C non-precious metal cathode catalysts for oxygen reduction in fuel cells. *J Mater Chem* **21**, 11392–11405 (2011).

5. Chung, H. T. *et al*. Direct atomic-level insight into the active sites of a high-performance PGM-free ORR catalyst. *Science (1979)* **357**, 479–484 (2017).

6. Djara R, Holade Y, Merzouki A, *et al*. Insights from the physicochemical and electrochemical screening of the potentiality of the chemically synthesized polyaniline. *Journal of the Electrochemical Society*, 167(6): 066503 (2020).

7. Ding, S. *et al*. Electrostatic Stabilization of Single-Atom Catalysts by Ionic Liquids. *Chem* **5**, 3207–3219 (2019).

8. Huang, W. Y. *et al*. Polyaniline Based Pt-Electrocatalyst for a Proton Exchanged Membrane Fuel Cell. *Polymers* 2020, Vol. 12, Page 617 **12**, 617 (2020).

9. Vernooij, R. R. *et al*. Comprehensive Vibrational Spectroscopic Investigation of trans,trans,trans-$[Pt(N_3)_2(OH)_2(py)_2]$, a Pt(IV) Diazido Anticancer Prodrug Candidate. *Inorg Chem* **55**, 5983–5992 (2016).

10. Drelinkiewicz, A. *et al*. Polyaniline stabilized highly dispersed Pt nanoparticles: Preparation, characterization and catalytic properties. *React Funct Polym* **69**, 630–642 (2009).

11. Bruckenstein, S. & Miller, B. Unraveling Reactions with Rotating Electrodes. *Acc Chem Res* **10**, 54–61 (1977).

12. Chaudhari, H. K., & Kelkar, D. S. Investigation of structure and electrical conductivity in doped polyaniline. *Polymer international*, 42(4), 380-384 (1997).

13. Song, E. & Choi, J. W. Conducting Polyaniline Nanowire and Its Applications in Chemiresistive Sensing. *Nanomaterials 2013, Vol. 3, Pages 498-523* **3**, 498–523 (2013).

14. Fomo, G., Waryo, T. T., Baker, P. & Iwuoha, E. I. ELECTROCHEMICAL SCIENCE Electrochemical Deposition and Properties of Polyaniline Films on Carbon and Precious

Metal Surfaces in Perchloric Acid/ Acetonitrile. *Int. J. Electrochem. Sci* **11**, 10347–10361 (2016).

Chapter 5

Defect-trapped Pt SSC

5.1 Introduction

As shown in Chapter 3 and Chapter 4, the physically and chemically adsorbed Pt SSCs are both unstable at the HER working potential. Finally, trapping Pt sites into the defects of a substrate, the most robust interaction between Pt single sites and carbon substrate, is needed. This chapter will investigate the synthesis, formation mechanism, atomic structure, and HER activity of Pt single sites trapped at an N-doped graphene substrate.

For the hydrogen evolution reaction (HER) in PEM water electrolysis, metallic Pt nanoparticles are the state-of-the-art catalyst in terms of intrinsic activity.[1, 2] However, the current mass loading of Pt nanoparticles will limit the global large-scale (terawatt) deployment of PEM water electrolysers.[3] Highly dispersed Pt SSCs have the potential to decrease the mass loading of Pt by maximising atom utilisation. Many Pt SSCs trapped at carbon substrates have been proposed and synthesised with higher mass activities for the HER by fully-exposed metal sites. However, two critical issues are still highly debated: (1) the intrinsic activity of Pt SSCs for the HER compared to metallic nanoparticles; (2) the synthesis of Pt SSCs with a well-defined desirable structure.

Regarding the intrinsic activity of Pt SSCs, many articles claim that Pt single sites trapped at N-doped graphene with an oxidation state of +2 can demonstrate a high HER activity.[4, 5] However, recent evidence shows those Pt single sites must be reduced to near metallic states to produce hydrogen.[6, 7] To clarify the Pt SSCs' intrinsic activity for the HER, a well-defined Pt SSC should be prepared and assessed under rigorous practice for activity measurements.

And its active structure under electrochemical working conditions needs to be analysed using in-situ characterisation methods.[8-10]

For the synthesis of well-defined Pt SSCs for the HER, carbon-based materials are the most reported substrates to support SSCs due to their high electrical conductivity and electrochemical stability.[11, 12] To prevent the aggregation of single sites at reduction potentials, Pt single sites must be chemically trapped on the defects of carbon substrates.[13] One-pot pyrolysis is commonly used to synthesise the trapped SSCs: pyrolysing the mixture of metal precursors and carbon matrix at high temperatures (700-1000 °C).[14-17] However, because of the complexity of the mixture and dynamic structural evolution of single sites during pyrolysis,[18, 19] it is challenging to synthesise the Pt SSC with a well-defined atomic structure.[20-23] To solve this problem, a simple structure before pyrolysis and in-situ characterisation techniques are necessary to clarify the Pt SSCs' formation mechanism and define its structure at an atomic level.[24, 25]

In this work, we investigate two critical issues: (1) the atomic structure and synthesis mechanism of a trapped Pt SSC prepared by pyrolysis; (2) the intrinsic activity of the Pt SSC for the HER. Firstly, the successful synthesis of a typical Pt SSC trapped in an N-doped graphene substrate by pyrolysis is demonstrated.[26] Then, the formation mechanism of this trapped Pt SSC is clarified by complementary in-situ characterization techniques. Specifically, in-situ heating scanning transmission electron microscopy (STEM) and in-situ temperature-dependent X-ray photoelectron spectroscopy (XPS) are employed to probe the physical and chemical structures of Pt sites at various temperatures (25-800°C). Direct evidence shows that N can anchor Pt sites and, in-situ trap them into the defects during the substrate graphitisation. Thirdly, after the definition of the atomic structure with in-situ/ex-situ characterisation techniques, our trapped Pt SSC's intrinsic activity for the HER is evaluated under a customised three-electrode setup, which minimises the mass transfer limitations at low overpotentials. It is found that the partially oxidised Pt SSC is less active for the HER compared to metallic Pt nanoparticles. Finally, the structure of the Pt SSC under working

conditions is investigated using operando X-ray absorption spectroscopy (XAS). The XAS data shows the Pt SSC is stable and remains a single-site structure at the HER working potentials.

This study clarifies the formation mechanism and atomic structure of the trapped SSC synthesised by pyrolysis via in-situ experiments. Furthermore, with our model catalyst, the intrinsic activity of trapped Pt SSC for the HER is uncovered. Our findings strongly suggest that an all-the-way in-situ characterisation is critical in the investigation of SSCs' presence, evolution, structure, and catalytic behaviour. This study could aid the design and synthesis of improved SSC for the HER and more electrochemical reactions.

5.2 Results and discussion

5.2.1 Synthesis of trapped Pt SSC on N-doped graphene by pyrolysis

By directly pyrolysising the Pt-PANI samples synthesised and defined in Chapter 4, the trapped Pt SSC was formed. The structure of the trapped Pt SSC was extensively characterised by microscopy and spectroscopy. Specifically, to completely graphitise PANI into N-doped graphene and trap Pt sites into the substrate simultaneously, Pt-PANI samples with various Pt loadings (10 wt%, 5 wt%, 2 wt%, and 1 wt%) were pyrolysed at 800 °C under pure nitrogen gas for 1.5 hrs. The physical structures of Pt after pyrolysis are obtained using ex-situ STEM (Fig. 5.1a-h). Pt nanoparticles are identified in the pyrolysed Pt-PANI samples with Pt loadings of 10 wt% (a, e), 5 wt% (b, f), and 2 wt% (c, g), especially at the edge of the substrates. It should be noted that a considerable amount of Pt maintains single sites, and the amount of Pt nanoparticles drops with the decrease of Pt loading. Eventually, when the loading of Pt reduces to 1 wt%, almost all the Pt remains as a single-site structure after pyrolysis (Fig. 5.1d, h). Therefore, we propose the 1 wt% Pt-PANI sample after pyrolysis as a model trapped Pt SSC for further investigation (referred to the trapped Pt SSC below).

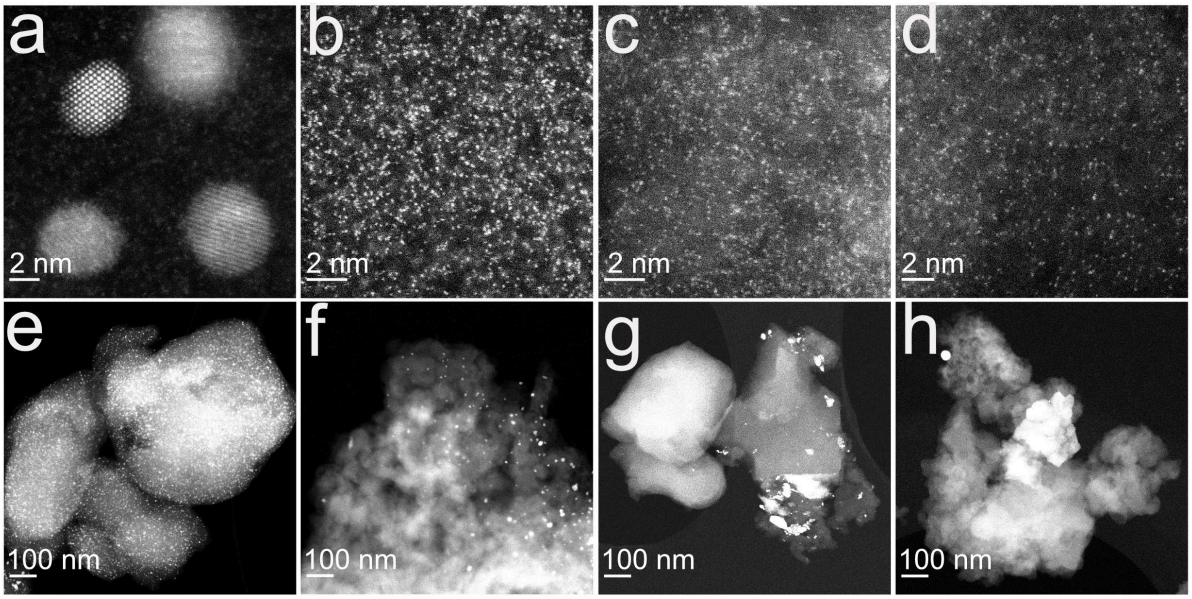


Figure 5.1: High-(**a-d**) and low-(**e-h**) resolution STEM images of Pt-PANI with various loadings after pyrolysis in N_2 at 800 °C for 1.5 hrs; 10 wt% (**a, e**), 5 wt% (**b, f**), 2 wt% (**c, g**), and 1 wt% (**d, h**).

The chemical structure of the trapped Pt SSC was clarified by spectroscopies. Raman spectroscopy and Cross-polarization Magic-angle spinning nuclear magnetic resonance (CPMAS NMR) were used to confirm the structure of PANI after pyrolysis. The ex-situ Raman spectra of PANI before/after pyrolysis (Fig. 5.2a) show that all the characteristic peaks of PANI vanish, and two peaks of graphite's D and G bands at 1360 cm^{-1} and 1580 cm^{-1} appear after pyrolysis, which indicates the formation of a defective graphene substrate.[27, 28] Furthermore, in the ^{15}N CPMAS NMR spectra of 1 wt% Pt-PANI (Fig. 5.2b), new peaks ranging from -50 to -200 ppm formed after pyrolysis prove the formation of pyridinic N and graphitic N.[29] Both Raman and NMR data suggest the PANI substrate has transformed into N-doped graphene after pyrolysis.

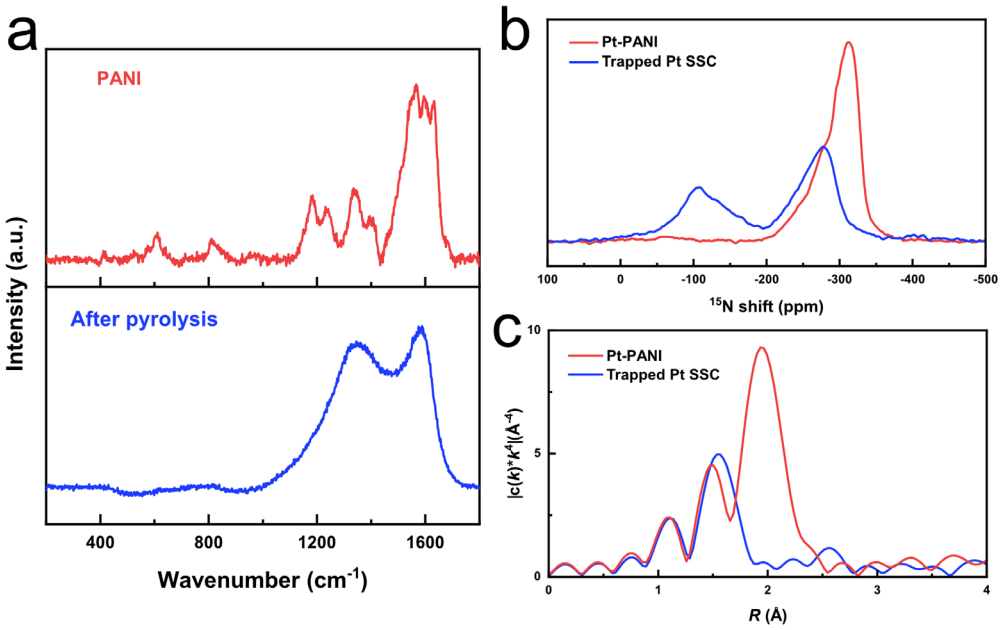


Figure 5.2: **a**, Raman spectra of PANI substrate before and after pyrolysis. **b**, **c**, CPMAS NMR spectra of ^{15}N (**b**), and FT-EXAFS (**c**) of 1 wt% Pt-PANI before and after heating in N_2 at 800 °C for 1.5hs.

Then, the Pt L_3-edge EXAFS spectra of the trapped Pt SSC (Fig. 5.2c, blue) are analysed to obtain the overall electronic structure of Pt. After pyrolysis, the Pt-Cl peak at 1.93 Å disappears, and the peak at 1.58 Å (Pt-N peak) remains dominant. The lack of the Pt-Pt peak at 2.73 Å, means Pt sites are still isolated and bonded to N.

5.2.2 Formation mechanism of trapped Pt SSC

Although a model trapped Pt SSC was prepared by pyrolysis, there still lacks information on how Pt sites are trapped on the substrate, and the atomic structure of Pt needs to be further clarified. Therefore, we first employ in-situ heating STEM to track the geometric structure change of Pt on the 10 wt% Pt-PANI sample at increasing temperatures. As the atomic STEM images in Fig. 5.3a-h show, the majority of the Pt sites in bulk areas (Fig. 5.3a-d) can remain isolated even if the temperature goes up to 800 °C; in comparison, some of the sites at the edge positions (Fig. 5.3e-h) start to aggregate at 500 °C, and further transform into nanoparticles at 800 °C, which corresponds to the ex-situ STEM images in Fig. 5.2a, e. The

formation of Pt nanoparticles illustrates that Pt sites are prone to aggregate at high temperatures, especially when the loading of Pt is relatively high.

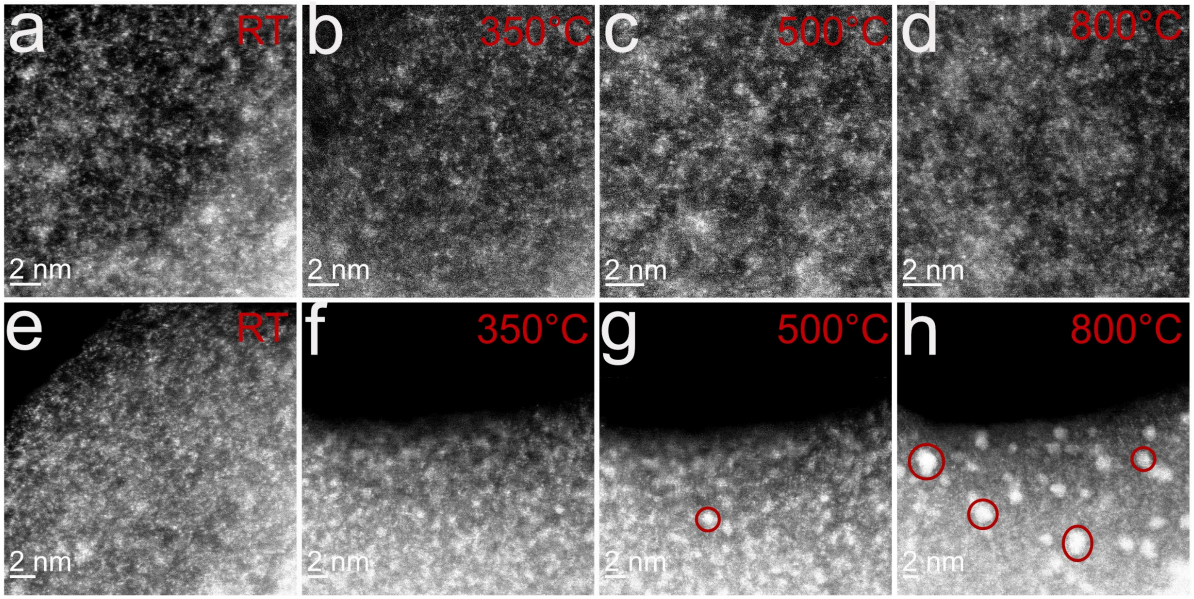


Figure 5.3: a-h, In-situ heating STEM images showing the structural evolution of Pt sites at the edge (a-d) and bulk (e-h) areas in 10 wt% Pt-PANI sample with increasing temperatures (RT, 350 °C, 500 °C, and 800 °C).

Then, in-situ temperature-dependent XPS is applied to track the changes in the bonding environment of Pt sites in sample 1 wt% Pt-PANI during pyrolysis. XPS spectra of the core level for Pt 4f, N 1s, Cl 2p, C 1s, and O 1s were recorded (Fig. 5.4). As Fig. 5.4a shows, with the rising temperature, the binding energy of Pt 4f negatively shifts by 0.8 eV, from 72.8 eV (Pt(+2)) at room temperature (RT) to 72.0 eV at 700 °C, meaning that the unoccupied orbitals of Pt 4f are partially filled with surrounding bonding sites at high temperature. More importantly, when the temperature increases to 700 °C, the N 1s peak is gradually split into two peaks: graphitic N peak at 400.9 eV and pyridinic N peak at 398.3 eV (Fig. 5.4b). This significant change indicates the graphitisation of PANI substrate at high temperatures, which is also supported by the shifts in the C-N peak in the C 1s region (Appendix Fig. 6.1).[26]

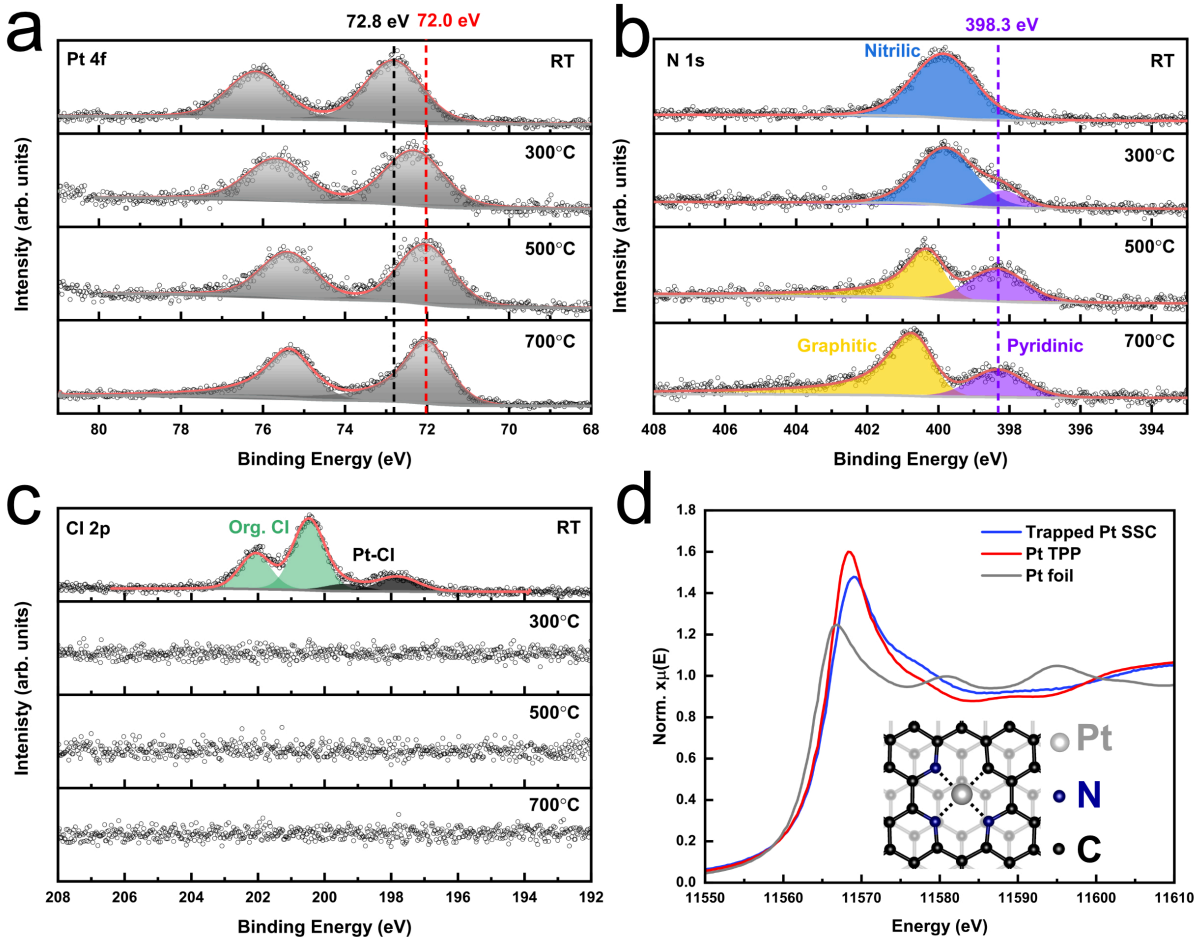


Figure 5.4: a-c, In-situ temperature-dependent XPS data of 1 wt% Pt-PANI to show how the bonding environment of Pt evolves during pyrolysis. Pt 4f spectra (**a**), N 1s spectra (**b**), and Cl 2p spectra (**c**). **d**, XANES of the trapped Pt-SSC synthesised by pyrolysis, compared with Pt TPP complex and Pt foil. The inset is a schematic of the trapped Pt-SSC structure; black for carbon, blue for N, and metallic for Pt.

Comparatively, the metal Cl peaks at 198.3 eV bonded to Pt sites, and organic Cl peaks at 200 eV from PANI disappear when heated to 300 °C (Fig. 5.4c). Similarly, oxygen peaks also disappear at 300 °C (Appendix Fig. 6.1). From the XPS survey scans (Appendix Fig. 6.2), though the intensity of N peaks has dropped, the vanishing of Cl and O indicates that only the remaining N can continuously trap Pt sites to form N-doped graphene at high temperatures. Based on the electronic structure, it is more likely that the pyridinic N can donate electrons to bond with (partially reduce) Pt sites than graphitic N.[30] By comparing the XANES data of the trapped Pt-SSC with PtTPP and Pt foil (Fig. 5.4d), we can confirm the Pt sites in trapped Pt-SSC have a similar oxidation state and bonding environment as Pt(II) in the PtTPP complex, which is consistent with our XPS results (Fig. 5.4a). By fitting the EXAFS data with calculated

DFT models, the atomic structure of the trapped Pt SSC has been defined: one Pt site bonding with 3 N and 1 C on the N-doped graphene (Pt-3N-C structure in the inset figure of Fig. 5.4d).

Overall, the formation mechanism and atomic structure of trapped Pt SSC are clarified by in-situ experiments. In the Pt-PANI samples, Pt sites are atomically bonded with N and Cl at an oxidation state of +2; during the pyrolysis process, Pt sites continuously bond with N to maintain as single sites; and then they are gradually reduced and trapped in the defects of the N-doped graphene by pyridinic N during the graphitisation. However, for Pt-PANI samples with high Pt loading, the crowded Pt sites are prone to aggregate into metallic nanoparticles when the surrounding N sites are evaporated at high temperatures.

5.2.3 HER activity of trapped Pt SSC

After clarifying the structure of the trapped Pt SSC (1 wt% Pt-PANI after pyrolysis), its intrinsic activity for the HER was evaluated using a three-electrode system and compared with other trapped Pt samples (5 wt%, 10 wt% Pt-PANI after pyrolysis) and commercial 20 wt% Pt/C (1 ug_{Pt} cm^{-2}). The customised three-electrode system (Appendix Fig. 6.3) is specially designed to minimise the mass transfer limitations in the HER, which is critical to accurately evaluate the intrinsic activity of catalysts for the HER.

To validate our electrochemical setup, we calculated the HER turnover frequency (TOF) of the commercial 20 %wt Pt/C and compared the value with the state-of-the-art mass-transfer H_2 pump techniques. The H_2 pump experiment is based on the feeding of pure hydrogen and ultralow loading of Pt. Specifically, the H_2 pump cell with 50 cm^2 active area MEAs was conducted at 80 °C using overhumidified H_2 at a total pressure of 150 KPa. H_2 was supplied at a constant rate of 2000 sccm, and the anode outlet was connected to the cathode inlet so that the exhaust hydrogen was fed into the cathode. Low-loaded Pt electrodes (3 ug_{Pt} cm^{-2}) served as working electrodes, while high-loaded Pt electrodes (400 ug_{Pt} cm^{-2}) served as counter/reference electrodes.[31]

The TOF is defined as the rate of H_2 produced per active site and is calculated as:

$$TOF = n_{H2} / (n_{site} \cdot time) = I / (q_{HER/HOR} \cdot Q_{HUPD}) = i / (2 \cdot Q_{HUPD})$$

where i is the measured HER/HOR current. Q_{HUPD} denotes the integrated charge in the HUPD experiment. The $q_{HER/HOR}$ is the number of charges transferred to evolve one H_2 molecule. Using our electrochemical setup, the 20 %wt Pt/C reached a TOF value of ~100 at -0.1 V (Fig. 5.5a), which is approaching the same order of magnitude as the numbers from the H_2 pump (TOF is ~1000). Specific current density curves were plotted in Fig. 5.5b by normalising the current by the ECSA of the 20 wt% commercial Pt/C sample, showing that an overpotential of 50 mV is required to reach a current density of 10 mA cm^{-2}. These data suggest our electrochemical cell and testing protocol can allow for a fair activity comparison of our Pt SSC with commercial Pt/C sample with ignorable mass transport limitation. Unfortunately, the activity of our oxidised Pt SSC samples could not be calculated to TOF, because the number of the active sites of our Pt SSC can not be determined by traditional CO stripping methods. The CO molecules can only strongly interact with metallic Pt structures, such as Pt nanoparticles.[32] However, as we proved before, the Pt in our Pt SSC samples is at an oxidation state of +2, which hardly interact with CO compared to metallic Pt nanoparticles.

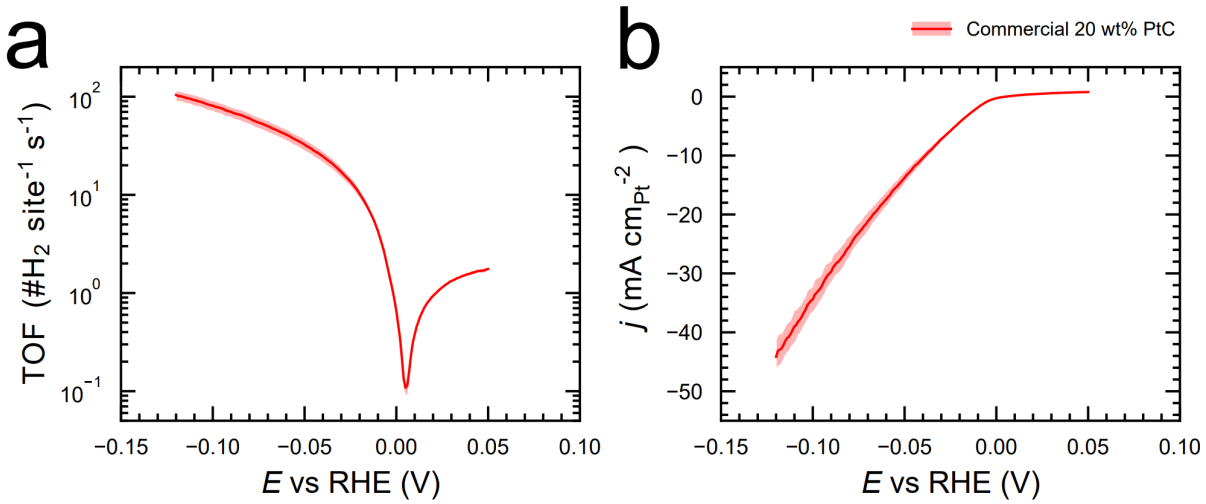


Figure 5.5: TOF polarisation curve (**a**) and specific current density curve (**b**) of the 20 wt% commercial Pt/C tested with our customised three-electrode cell. The solid line is the average value from three independent measurements and the shaded area denotes the standard error.

The intrinsic activities of trapped Pt samples and Pt/C were analysed by cyclic voltammetry (CV) at a scan rate of 10 mV/s in 0.5 M H_2SO_4 saturated with pure H_2. The representative structures of those trapped Pt samples (1 wt%, 5 wt%, and 10 wt% Pt-PANI after pyrolysis, abbreviated to trapped 1 wt%, 5 wt%, and 10 wt% Pt respectively) and commercial 20 wt% Pt/C are visualised by atomic STEM images in Fig. 5.1 and Appendix Fig. 6.4. As shown, the trapped 10 wt% Pt sample is composed of well-dispersed nanoparticles and single sites, and the trapped 1 wt% Pt sample is a pure single-site structure. And 20 wt% Pt/C is full of nanoparticles with an average size of 2-3 nm (Appendix Fig. 6.4).

From the CV curves shown in Fig. 5.6a, the trapped 1 wt% Pt sample (trapped Pt SSC, blue line) has a much higher onset overpotential (the potential to reach a current density of 1mA cm^{-2}) of ~330 mV for HER compared with only 11 mV for Pt/C (yellow). And the HER activities of trapped Pt samples are significantly increasing with the loading of Pt (from blue to green to red). The trapped 10 wt% Pt sample with dominant nanoparticles shows superior activity. As shown by the red line in Fig. 5.6a, it needs only 80 mV VS. RHE to reach a current density of 10 mA cm^{-2}, which is 410 mV and 350 mV lower than the trapped 1 wt% and 5 wt% samples, respectively.

Furthermore, from the curves in Fig. 5.6b calculated by the base-10 logarithm of the geometric current density in Fig. 5.6a, the HER kinetics of Pt single sites dominated samples (trapped 1 wt% and 5 wt% Pt) are much lower than Pt nanoparticles dominated ones (trapped 10 wt% Pt and 20 wt% Pt/C). It indicates that the trapped Pt SSC may have a different reaction mechanism for HER to metallic Pt nanoparticles.[33] A correlation between the oxidation state of Pt and HER activity is built in Fig. 5.6c. The more reduced Pt structure has a lower onset overpotential for HER, which proves metallic Pt is more active than the oxidised Pt SSC trapped on the N-doped graphene.

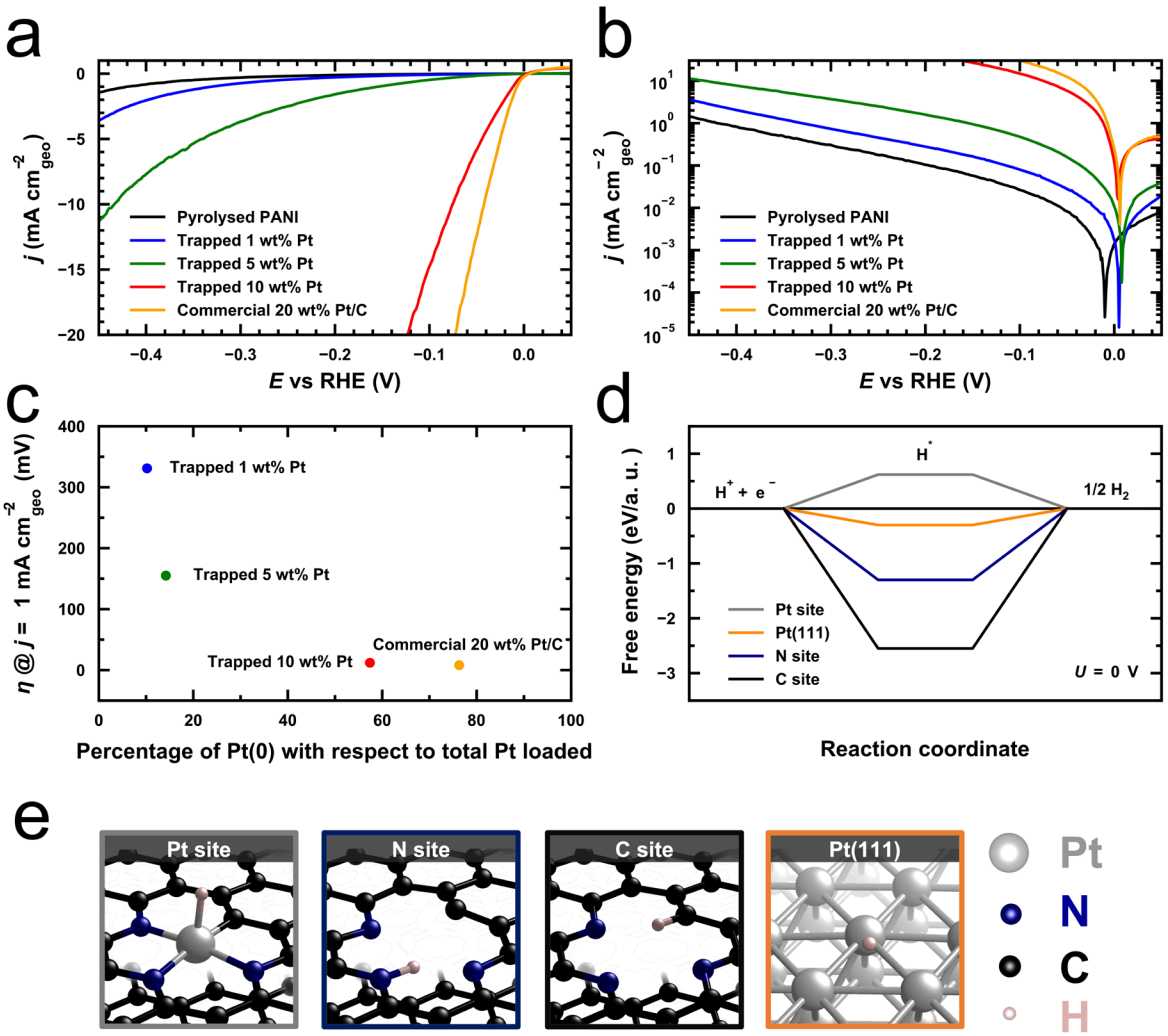


Figure 5.6: a, Average CV curves for trapped Pt SSC samples synthesised by one-pot pyrolysis and commercial 20 wt% Pt/C in 0.5 M H_2SO_4 electrolyte, showing the overpotential needed to reach a specific geometric current density. **b**, The areal current density on the logarithm-10 scale derived from the average CV curves for Pt samples in (**a**). **c**, The correlation between the onset overpotentials (n at the current density of 1 mA cm^{-2}) and the peak positions of the binding energy of Pt $4f_{7/2}$ for Pt samples. **d**, Free energy diagram for hydrogen evolution at reaction potential U = 0 V. The data are calculated at 1 bar of H_2 and pH = 0 at 300 K. **e**, Relaxed structures of hydrogen adsorbed on Pt site, N site, C site and the FCC site on Pt(111) surface). Pink for hydrogen, black for carbon, blue for N, and metallic for Pt.

The origin of the low HER activity of the trapped Pt SSC is probed from the first principles. We calculate the hydrogen chemisorption free energy at applied external potential U = 0 V and pH = 0 on the Pt site, C site, and the N site of the Pt-3N-C model, as shown in Fig. 5.6e. The hydrogen chemisorption free energy calculated based on density-functional theory is an indicator of HER activity for Pt group metals, with a value closest to 0 eV showing the highest HER activity.[34] An 0.69 eV hydrogen chemisorption energy for the Pt site is observed (grey in Fig. 5.6d). This value is further away from the thermo-neutral value than that of the Pt(111)

surface (-0.36 eV) (yellow in Fig. 5.6d), implying that the HER may be less favoured to occur on the single Pt site than on the metallic Pt(111) surface. Strong hydrogen adsorption on the N (-1.35 eV) and C site (-2.52 eV) in the nitrogen defects can also be observed, suggesting that these two sites are unlikely to catalyse the HER. These observations are in agreement with our experimentally measured activity.

5.2.4 The structure of trapped Pt SSC at working potential

Finally, operando X-ray absorption spectroscopy was employed to investigate the structure of the trapped Pt SSC under working potentials for HER. The current and XAS spectra of the Pt L_3-edge were recorded simultaneously when the sample was applied with various potentials (from OCV (0.50 V) to -0.30 V vs. RHE). The whole setup of the operando experiment is shown in Chapter 2. The chronoamperometry (CA) curves recorded at 7 potentials are shown in Fig. 5.7a, revealing that hydrogen starts to evolve after -0.1 V vs. RHE. From the FT-EXAFS spectra of the Pt L_3-edge at all potentials (Fig. 5.7b), the Pt-N bond at 1.50-1.60 Å is always the dominant peak, and Pt-Pt peak is not found; but some distortions of the Pt-N peak with the decreasing of potential are recorded.

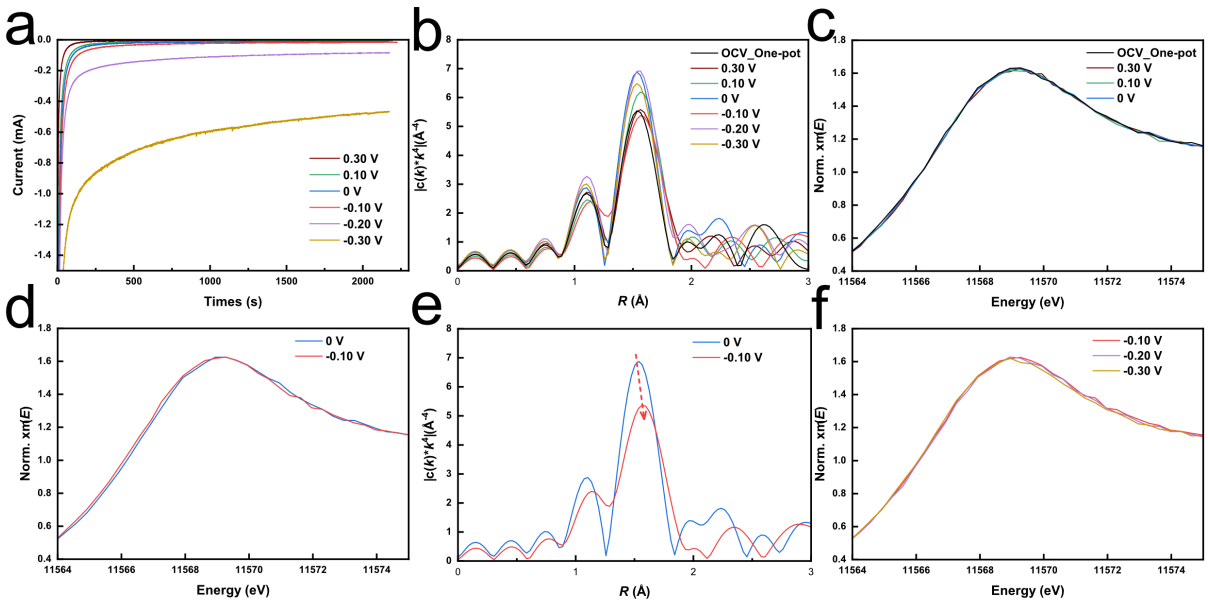


Figure 5.7: **a**, The chronoamperometry curves of trapped Pt SSC at different applied potentials. **b**, The FT-EXAFS data of Pt L_3-edge for trapped Pt SSC at applied potentials. **c**, **d**, **f**, The XANES spectra of Pt L_3-edge line of trapped Pt SSC at applied potentials from OCV

to -0.30 V: OCV to 0 V at (**c**), 0 V to -0.1 V at (**d**), and -0.1 V to -0.3 V at (**f**). **e**, The FT-EXAFS spectra of Pt L_3-edge for trapped Pt SSC are highlighted at 0 V and -0.10 V.

From OCV to 0 V vs. RHE, there is no shift in the absorption edge and the white-line intensity of the XANES spectra (Fig. 5.7c), which means the oxidation state of Pt is unchanged before 0 V. Still, a slight reduction of Pt has been found from 0 V to -0.1 V (Fig. 5.7d). The edge line negatively shifts by 0.1 eV at -0.1 V when the HER happens. An apparent distortion in the Pt-N peak in the FT-EXAFS spectra has also been observed at -0.1 V in Fig. 5.7e. After fitting the operando EXAFS data with the proposed Pt-3N-C structure, we find the Pt-N bond may be shortened by ~0.01 Å. The slight reduction of Pt's oxidation state and the Pt-N bond length reduction indicates that the trapped Pt SSC has been slightly reduced to trigger the reaction.

However, at working potentials for HER (-0.1 V, -0.2 V, and -0.3 V vs. RHE), the oxidation state of Pt remains stable, as shown by the XANES spectra in Fig. 5.7f. And there is no Pt-Pt peak at ~2.70 Å detected (Fig. 5.6b). Those data show Pt stably bonds with N and remains as a single-site structure under HER working conditions. Even when the potential returns to OCV after CA tests, the Pt-N bonding still holds (Fig. 5.8a). Finally, the stability of the trapped Pt SSC was further proven by the ADF-STEM images of the spent catalyst. As shown in Fig. 5. 8b and 8c, no evident Pt aggregates are recorded after 2 hours of the CA test at -0.2 V vs. RHE. All those data have illustrated that the trapped Pt SSC is a stable structure for HER working potentials.

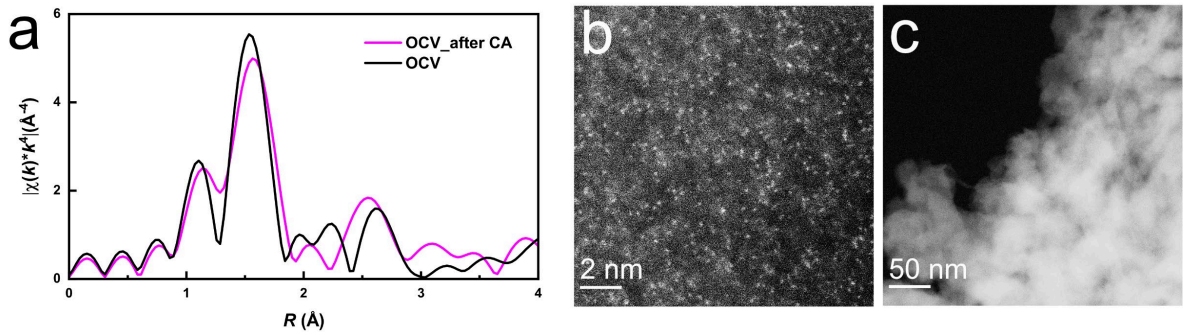


Figure 5.8: a, FT-EXAFS spectra of Pt-L_3 for trapped Pt SSC at OCV before and after CA tests. **b**, **c**, Atomic STEM images of trapped Pt SSC after 2 hours of CA test at -0.2 V. vs. RHE.

5.3 Conclusion

In this work, a model Pt SSC trapped on N-doped graphene was prepared by pyrolysing atomically-dispersed Pt on PANI substrate. With the advantages of well-defined structures before pyrolysis and all-the-way in-situ characterisation experiments, the formation mechanism of the trapped Pt SSC is uncovered. From the in-situ heating STEM and in-situ temperature-dependent XPS data, we identified that N sites on the substrate could persistently bond with Pt sites during pyrolysis and in-situ trap Pt into the defects after the substrate graphitisation. However, there is a maximum mass loading limit to maintain Pt as a single-site structure at high temperatures. Pt sites could be reduced and aggregated into nanoparticles after the loss of N. Furthermore, thanks to the ex-situ and in-situ characterisation results, the atomic structure of the trapped Pt SSC is defined: Pt single sites bond with three pyridinic nitrogen and one carbon on the N-doped graphene substrate. Then, the intrinsic activity of this well-defined trapped Pt SSC for HER is clarified. It is found that the oxidised Pt SSC is not thermodynamically favourable for HER, which requires an extra ~300 mV overpotential to trigger the reaction compared to metallic Pt nanoparticles. By correlating the activity and oxidation state of our Pt catalysts and commercial Pt nanoparticles, we confirmed that a metallic Pt structure is more active for the HER because metallic Pt has a lower hydrogen chemisorption energy. The operando XAS experiment shows our trapped Pt SSC is stable at the HER reduction overpotentials. Therefore, we can infer that fully-exposed metallic Pt structures (single atoms or small clusters) trapped on substrates are the ultimate structure for the HER. However, metallic Pt single-site structures that are stable under the HER conditions have not been well-demonstrated to date. These findings will facilitate the design and synthesis of SSCs for the HER and other electrochemical reactions.

5.4 References

1. Hansen, J. N. *et al.* Is There Anything Better than Pt for HER? *ACS Energy Lett* **6**, 1175–1180 (2021).

2. Zalitis, C. M., Kramer, D., Sharman, J., Wright, E. & Kucernak, A. R. Pt Nano-Particle Performance for PEFC Reactions at Low Catalyst Loading and High Reactant Mass Transport. *ECS Trans* **58**, 39–47 (2013).

3. Hubert, M. A., King, L. A. & Jaramillo, T. F. Evaluating the Case for Reduced Precious Metal Catalysts in Proton Exchange Membrane Electrolyzers. *ACS Energy Lett* **7**, 17–23 (2022).

4. Li, J. *et al.* Unveiling the Nature of Pt Single-Atom Catalyst during Electrocatalytic Hydrogen Evolution and Oxygen Reduction Reactions. *Small* **17**, 2007245 (2021).

5. Liu, D. *et al.* Atomically dispersed platinum supported on curved carbon supports for efficient electrocatalytic hydrogen evolution. *Nature Energy 2019 4:6* **4**, 512–518 (2019).

6. Wang, J. *et al.* In Situ Identifying the Dynamic Structure behind Activity of Atomically Dispersed Platinum Catalyst toward Hydrogen Evolution Reaction. *Small* **17**, 2005713 (2021).

7. Fang, S. *et al.* Uncovering near-free platinum single-atom dynamics during electrochemical hydrogen evolution reaction. *Nature Communications 2020 11:1* **11**, 1–8 (2020).

8. Li, X., Yang, X., Zhang, J., Huang, Y. & Liu, B. In Situ/Operando Techniques for Characterization of Single-Atom Catalysts. *ACS Catal* **9**, 2521–2531 (2019).

9. Speck, F. D. *et al.* Atomistic Insights into the Stability of Pt Single-Atom Electrocatalysts. *J Am Chem Soc* **142**, 15496–15504 (2020).

10. Cao, L. *et al.* Identification of single-atom active sites in carbon-based cobalt catalysts during electrocatalytic hydrogen evolution. *Nature Catalysis 2018 2:2* **2**, 134–141 (2018).

11. Yang, Y. *et al.* Recent Progress of Carbon-Supported Single-Atom Catalysts for Energy Conversion and Storage. *Matter* **3**, 1442–1476 (2020).

12. Gu, J., Hsu, C. S., Bai, L., Chen, H. M. & Hu, X. Atomically dispersed Fe^{3+} sites catalyze efficient CO_2 electroreduction to CO. *Science (1979)* **364**, 1091–1094 (2019).

13. Tang, P. *et al.* Elucidating the Formation and Structural Evolution of Platinum Single-Site Catalysts for the Hydrogen Evolution Reaction. *ACS Catal* **12**, 3173–3180 (2022).

14. Fei, H. *et al.* General synthesis and definitive structural identification of MN_4C_4 single-atom catalysts with tunable electrocatalytic activities. *Nature Catalysis 2018 1:1* **1**, 63–72 (2018).

15. Xia, C. *et al.* General synthesis of single-atom catalysts with high metal loading using graphene quantum dots. *Nature Chemistry 2021 13:9* **13**, 887–894 (2021).

16. Ju, W. *et al.* Understanding activity and selectivity of metal-nitrogen-doped carbon catalysts for electrochemical reduction of CO_2. *Nature Communications 2017 8:1* **8**, 1–9 (2017).

17. Peng, Y., Lu, B. & Chen, S. Carbon-Supported Single Atom Catalysts for Electrochemical Energy Conversion and Storage. *Advanced Materials* **30**, 1801995 (2018).

18. Zhao, S. *et al.* One-Pot Pyrolysis Method to Fabricate Carbon Nanotube Supported Ni Single-Atom Catalysts with Ultrahigh Loading. *ACS Appl Energy Mater* **1**, 5286–5297 (2018).

19. Copéret, C. Single-Sites and Nanoparticles at Tailored Interfaces Prepared via Surface Organometallic Chemistry from Thermolytic Molecular Precursors. *Acc Chem Res* **52**, 1697–1708 (2019).

20. Hai, X. *et al.* Scalable two-step annealing method for preparing ultra-high-density single-atom catalyst libraries. *Nature Nanotechnology 2021 17:2* **17**, 174–181 (2021).

21. Kaiser, S. K. *et al.* Performance descriptors of nanostructured metal catalysts for acetylene hydrochlorination. *Nature Nanotechnology 2022 17:6* **17**, 606–612 (2022).

22. Zhao, L. *et al.* Cascade anchoring strategy for general mass production of high-loading single-atomic metal-nitrogen catalysts. *Nature Communications 2019 10:1* **10**, 1–11 (2019).

23. Han, L. *et al.* A single-atom library for guided monometallic and concentration-complex multimetallic designs. *Nature Materials 2022 21:6* **21**, 681–688 (2022).

24. Kottwitz, M., Li, Y., Wang, H., Frenkel, A. I. & Nuzzo, R. G. Single Atom Catalysts: A Review of Characterization Methods. *Chemistry - Methods* **1**, 278–294 (2021).

25. Maurer, F. *et al.* Tracking the formation, fate and consequence for catalytic activity of Pt single sites on CeO_2. *Nature Catalysis 2020 3:10* **3**, 824–833 (2020).

26. Kaiser, S. K. *et al.* Nanostructuring unlocks high performance of platinum single-atom catalysts for stable vinyl chloride production. *Nature Catalysis 2020 3:4* **3**, 376–385 (2020).

27. Kaniyoor, A. & Ramaprabhu, S. A Raman spectroscopic investigation of graphite oxide derived graphene. *AIP Adv* **2**, 032183 (2012).

28. Chung, H. T. *et al.* Direct atomic-level insight into the active sites of a high-performance PGM-free ORR catalyst. *Science (1979)* **357**, 479–484 (2017).

29. Kim, G., Lee, J., Liu, T. & Grey, C. P. Characterizing Nitrogen Sites in Nitrogen-Doped Reduced Graphene Oxide: A Combined Solid-State ^{15}N NMR, XPS, and DFT Approach. *Journal of Physical Chemistry C* **125**, 10558–10564 (2021).

30. Lin, Y. C. *et al.* Structural and Chemical Dynamics of Pyridinic-Nitrogen Defects in Graphene. *Nano Lett* **15**, 7408–7413 (2015).

31. Neyerlin, K. C., Gu, W., Jorne, J. & Gasteiger, H. A. Study of the Exchange Current Density for the Hydrogen Oxidation and Evolution Reactions. *J Electrochem Soc* **154**, B631 (2007).

32. Ciapina, E. G., Santos, S. F. & Gonzalez, E. R. Electrochemical CO stripping on nanosized Pt surfaces in acid media: A review on the issue of peak multiplicity. *Journal of Electroanalytical Chemistry* **815**, 47–60 (2018).

33. Prats, H. & Chan, K. The determination of the HOR/HER reaction mechanism from experimental kinetic data. *Physical Chemistry Chemical Physics* **23**, 27150–27158 (2021).

34. Nørskov, J. K. *et al.* Trends in the Exchange Current for Hydrogen Evolution. *J Electrochem Soc* **152**, J23 (2005).

Conclusions and future work

Key findings

This DPhil work has been devoted to the systematic study of the synthesis, characterisation, and catalytic activity of Pt single-site catalysts for the HER.

In Chapter 3, a physically adsorbed Pt single-site complex catalyst was synthesised by complexing with aniline and chloride ligands onto graphene. This allowed us to use operando X-ray absorption spectroscopy to characterise how the oxidation state and bonding environment of platinum changes in this Pt SSC for the HER at the molecular level. First, we confirmed that the Pt is atomically dispersed in the as-prepared Pt SSC by STEM and XRD; we observed a mixture of Pt(II) and Pt(IV) by XPS and XANES and clarified platinum coordination to aniline by ex-situ EXAFS. Then we probed the oxidation state and molecular structure as a function of applied potential using operando EXAFS and XANES. As the potential is lowered from OCV, the Pt oxidation state decreases, and the aniline and Cl ligands dissociate with Pt sites. Finally, once the onset of the HER at 0 V versus RHE is reached, the platinum is completely reduced, and metallic platinum atoms agglomerate to form catalytic nanoclusters. This work suggests that Pt single-site catalysts physically dispersed on substrates do not remain atomically dispersed during the HER process. The molecular structure of the platinum complexes is lost due to the reduction of the platinum. Stronger interaction between Pt sites and substrates is needed to stabilise the single-site structure.

For this reason, in Chapter 4, a model Pt SSC chemically anchored on the polyaniline substrate was synthesised. With the advantage of complementary characterisation techniques, it was found that Pt (+2) sites are atomically chemisorbed on the PANI by interacting with N at the substrate and remaining Cl ligands from the Pt precursor. After the structure of the chemisorbed Pt SSC was defined, its activity for the HER was also clarified. Unfortunately,

the oxidised Pt single sites anchored on PANI are not active. After repeated CV scanning, the N at PANI substrate is changed, and these Pt (+2) sites are prone to be reduced and aggregate into nanoparticles, which are found to be active for the HER. Our findings prove that the chemisorbed single Pt sites bonding to N at an oxidation state of +2 is not desirable for the HER, and the chemisorption interaction between Pt sites and the PANI substrate is still not robust enough to prevent Pt sites from aggregating at reducing potentials.

Therefore, in Chapter 5, by directly pyrolysising the well-defined Pt-PANI samples in Chapter 4, we obtained the Pt single sites trapped in the defects of the N-doped graphene substrate, which is the most robust interaction between the Pt sites and carbon substrates to stabilise the single-site structure. With the well-defined structures of the Pt-PANI sample and in-situ characterisation techniques, the formation mechanism of the trapped Pt SSC was uncovered. From the in-situ heating STEM and temperature-dependent XPS results, we identified that N sites on the substrate could persistently bond with Pt sites during pyrolysis and in-situ trap Pt into the defects by Pt-N bonding after the substrate graphitisation. However, there is a maximum mass loading limit to maintain Pt as a single-site structure at high temperatures. Pt sites could be reduced and aggregated into nanoparticles after the loss of N during heating. Thanks to our ex-situ and in-situ characterisation results, the atomic structure of the trapped Pt SSC was determined: Pt single sites bond with three pyridinic nitrogen and one carbon on the N-doped graphene substrate. Then, the intrinsic activity of this well-defined trapped Pt SSC for the HER was clarified. It is found that the oxidised Pt SSC is not thermodynamically favourable for HER, which displays a higher overpotential for the HER compared to metallic Pt nanoparticles. The operando XAS experiment shows that the trapped Pt SSC is stable at the HER working potentials. By correlating the activity and oxidation state of Pt catalysts, we confirmed that a metallic Pt structure is more active for the HER because metallic Pt has a lower hydrogen chemisorption energy.

Through my DPhil projects, it can be confirmed that a strong interaction between Pt single sites and carbon substrates is needed to stabilise Pt SSCs, such as trapping Pt sites into the

N defects. And the near metallic Pt structures are the active structure for the HER. Therefore, it can be inferred that fully-exposed metallic Pt structures (single atoms with oxidation sate of 0 or small clusters) trapped on substrates are the ultimate catalysts for the HER. This work will facilitate the design and synthesis of desired Pt SSCs for the HER, which can significantly reduce the mass loading of precious metals in PEM water electrolysers.

Future work

Firstly, one of the following key questions that remain to answer is how to synthesise near-metallic Pt SSCs trapped on a carbon substrate that is supposed to be stable and active for the HER. Because metallic Pt sites have a high surface free energy, leading to severe aggregation of their single dispersion. Appropriate approaches, such as molecular engineering, are necessary to construct and control the bonding environment of Pt sites. And the development of novel synthesis strategies that can be incorporated into the current chemical industry is also critical to achieving the single-atom concept. Secondly, the synthesis method of Pt SSCs we developed in Chapter 4 and Chapter 5 is adaptable to other transition metals, like iridium and cobalt. Iridium and cobalt single sites can be trapped in the defects of N-doped graphene by the pyrolysis of Ir-PANI and Co-PANI samples (Appendix Fig. 6.7).. It would be scientifically interesting to investigate their activity and stability in other electrochemical reactions, including oxygen reduction reaction, oxygen evolution reaction, and carbon reduction reaction. Applying these defect-trapped SSCs in the wide heterogeneous catalysis field is a highly relevant and popular research area at the moment. Finally, the methodology of in-situ and operando experiments in my work are a good demonstration in the investigation of SSCs' presence, evolution, structure, and catalytic behaviour. I hope that the results of my DPhil projects will aid the development of the research field of Pt single-site catalysts and facilitate the synthesis of improved catalysts for the HER.

Appendices

A. In-situ temperature-dependent XPS data

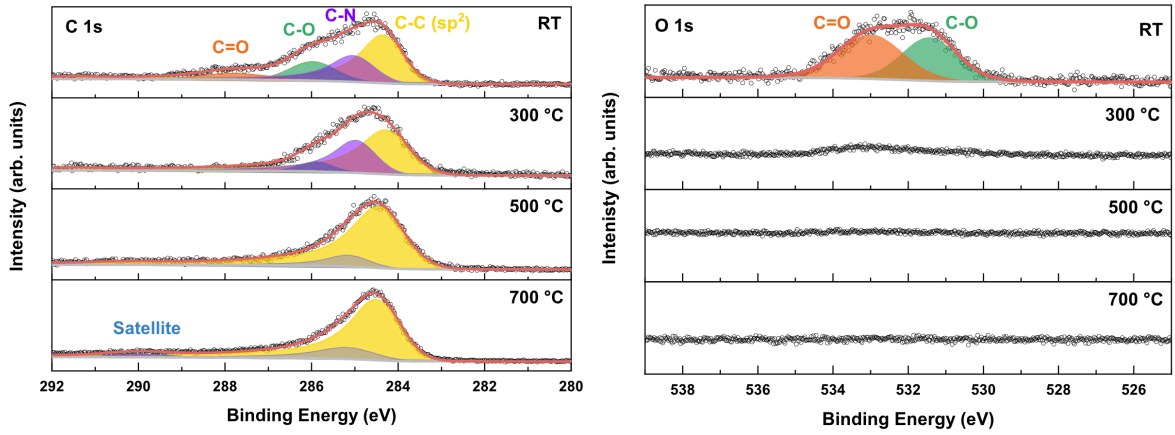


Figure 6.1: In-situ temperature-dependent XPS data of the C 1s and O 1s peaks for the 1 wt% Pt-PANI sample. Only C-N and C-C sp^2 peaks are maintained after being heated at 700 °C.

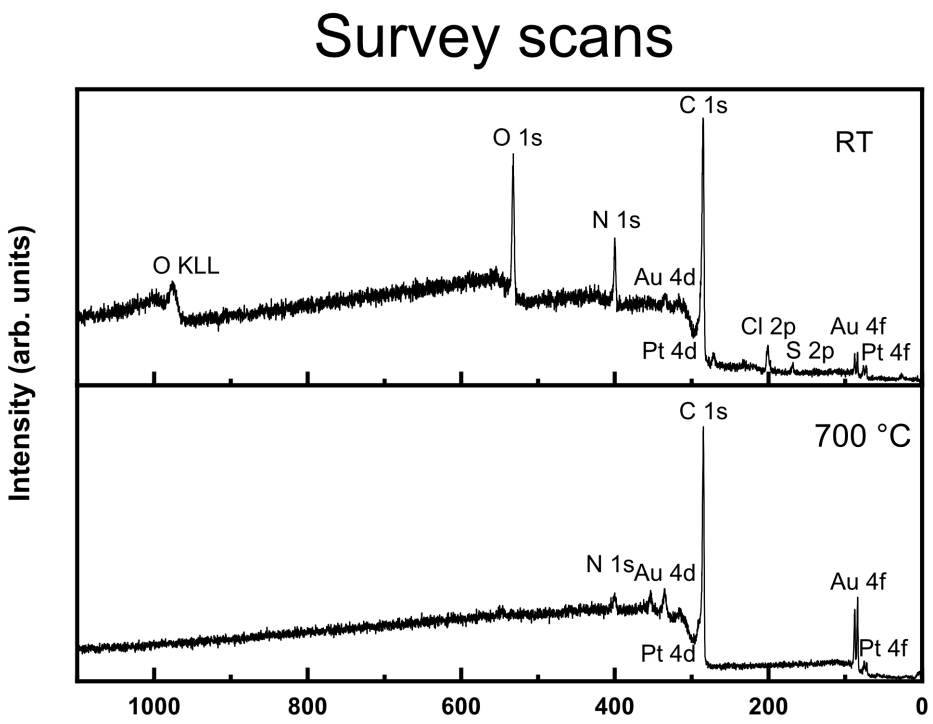


Figure 6.2: In-situ temperature-dependent XPS data of the survey scans for the 1 wt% Pt-PANI sample at RT and 700 °C.

B. The customised three-electrode system



Figure 6.3: our customised three-electrode system uses a well-polished glassy carbon as the working electrode, a $Hg/HgSO_4$ as the reference electrode, and Pt mesh as the counter electrode.

C. STEM images of commercial 20 wt% Pt/C

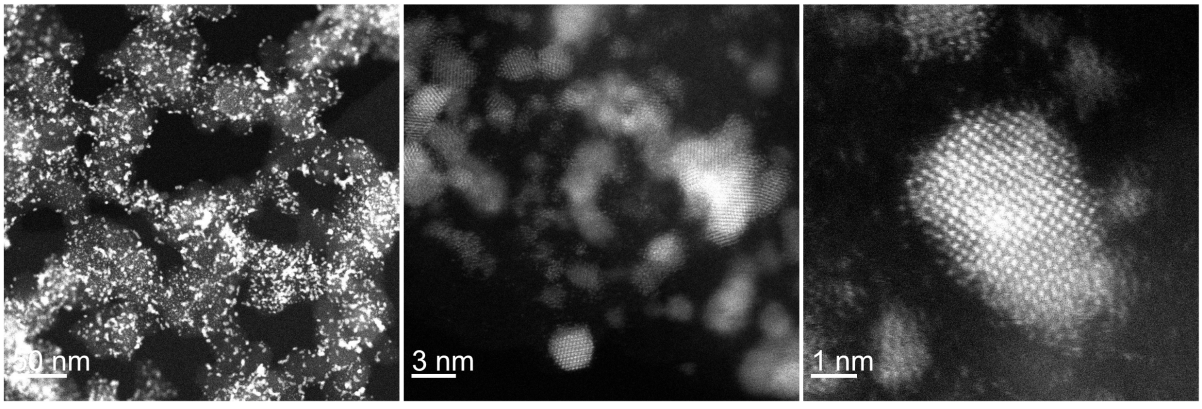


Figure 6.4: High-resolution images of 20 wt% Pt/C shows well-dispersed Pt nanoparticles with an average size of around 3 nm on the carbon support.

D. In-situ heating STEM images of Pt-PANI showing another edge area during heat treatment

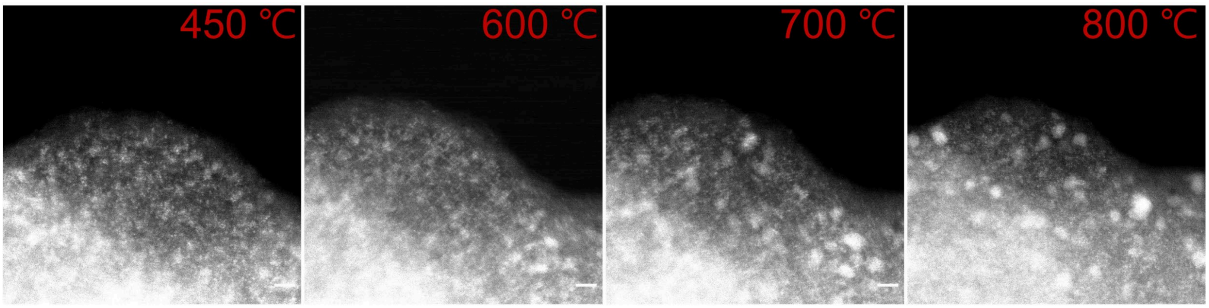


Figure 6.5: High-resolution in-situ heating STEM images of Pt sites at another edge area in the 10 wt% Pt-PANI sample at varied heating temperatures (450 °C, 600 °C, 700 °C, and 800 °C). The scale bar is 2 nm in a-d.

E. Ex-situ XPS data of Pt-PANI with different Pt loading after pyrolysis

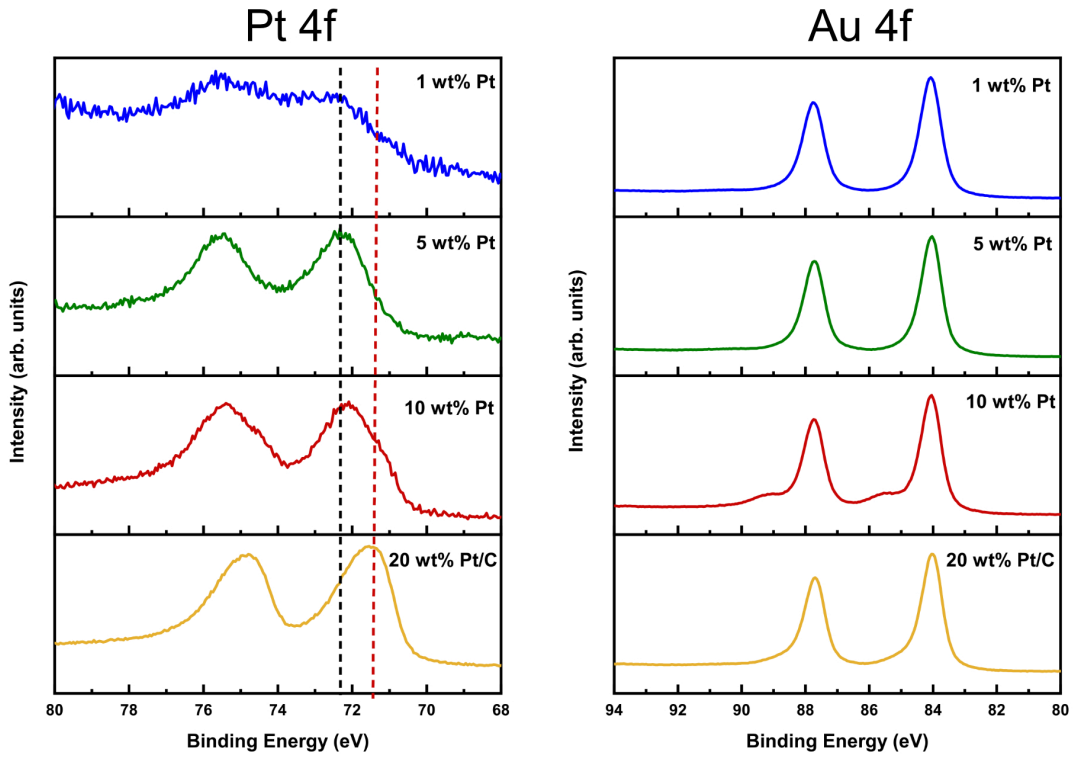


Figure 6.6: Ex-situ XPS data: Pt 4f and Au 4f (reference) spectra from the 2 wt% (blue), 5 wt% (green), 10 wt% (red) Pt-PANI samples, and 20 wt% Pt/C (yellow)

F. STEM images of trapped Co and Ir SSC on N-doped graphitic carbon

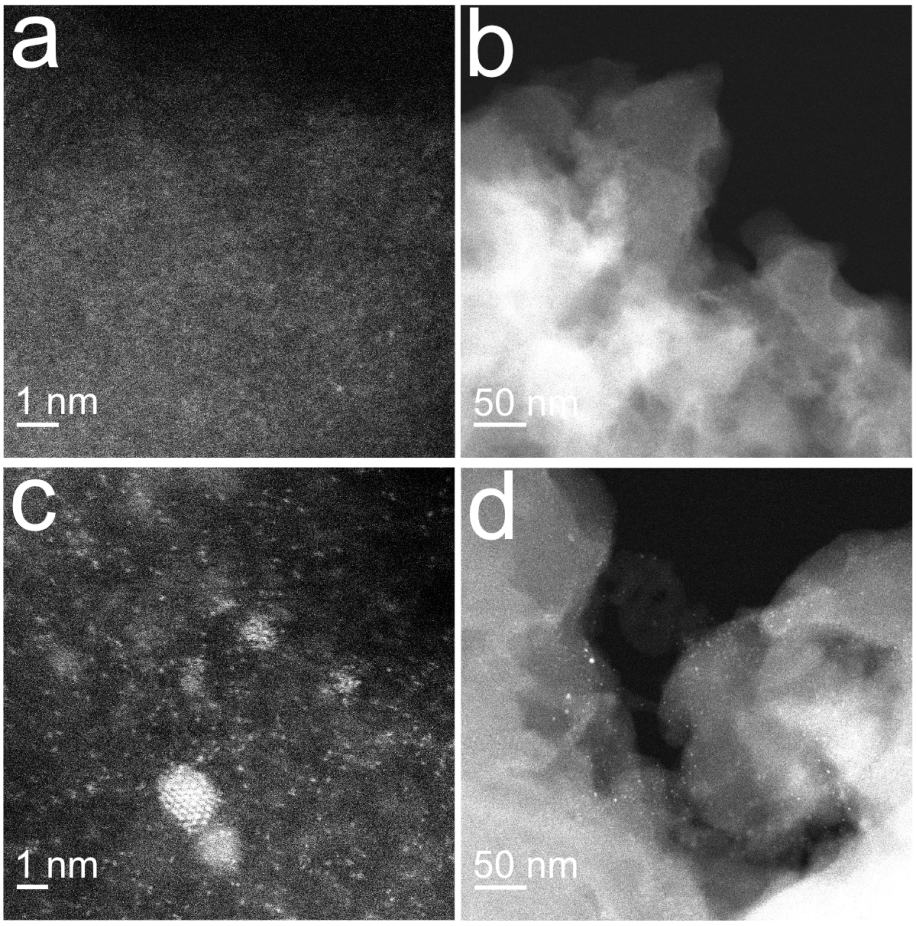


Figure 6.7: High-resolution STEM images of Co single sites (5 wt%, **a** and **b**) and Ir single sites (1 wt%, **c** and **d**) trapped at pyrolysed PANI.